UNIVERSITÉ DE LILLE

Doctoral school **ED SMRE**

University Department **Laboratoire de Physique des Lasers, Atomes et Molécules (PhLAM)**

Thesis defended by **Carlos MAS ARABÍ**

Defended on 24th October 2018

In order to become a Doctor from Université de Lille

Academic Field **Physics**
Speciality **Optics and Lasers, Physical Chemistry, Atmosphere**

Nonlinear propagation in optical fibers: from soliton radiations to multimode instabilities

Thesis supervised by	Alexandre Kudlinski	Supervisor
	Matteo Conforti	Supervisor
Comittee members		
Referees	Costantino de Angelis	Università degli Studi di Brescia
	Albert Ferrando	Universitat de València
Examiners	Katarzyna Krupa	Università degli Studi di Brescia
	Arnaud Mussot	Université de Lille
	Dmitry Skryabin	University of Bath
	Alessandro Tonello	Université de Limoges
Supervisors	Matteo Conforti	Université de Lille
	Alexandre Kudlinski	Université de Lille

UNIVERSITÉ DE LILLE

Doctoral school **ED SMRE**

University Department **Laboratoire de Physique des Lasers, Atomes et Molécules (PhLAM)**

Thesis defended by **Carlos MAS ARABÍ**

Defended on 24th October 2018

In order to become a Doctor from Université de Lille

Academic Field **Physics**
Speciality **Optics and Lasers, Physical Chemistry, Atmosphere**

Nonlinear propagation in optical fibers: from soliton radiations to multimode instabilities

Thesis supervised by	Alexandre Kudlinski	Supervisor
	Matteo Conforti	Supervisor
Comittee members		
Referees	Costantino de Angelis	Università degli Studi di Brescia
	Albert Ferrando	Universitat de València
Examiners	Katarzyna Krupa	Università degli Studi di Brescia
	Arnaud Mussot	Université de Lille
	Dmitry Skryabin	University of Bath
	Alessandro Tonello	Université de Limoges
Supervisors	Matteo Conforti	Université de Lille
	Alexandre Kudlinski	Université de Lille

UNIVERSITÉ DE LILLE

École doctorale **ED SMRE**

Unité de recherche **Laboratoire de Physique des Lasers, Atomes et Molécules (PhLAM)**

Thèse presentée par **Carlos MAS ARABÍ**

Soutenue le 24 Octobre 2018

En vue de l'obtention du grade de docteur de l'Université de Lille

Discipline **Physique**
Specialité **Optique et Lasers, Physico-Chimie, Atmosphère**

Propagation non-linéaire dans les fibres optiques: solitons, ondes dispersives et instabilités multimodes

Thèse dirigée par	Alexandre Kudlinski	Directeur
	Matteo Conforti	Directeur
Composition du jury		
Rapporteurs	Costantino de Angelis	Università degli Studi di Brescia
	Albert Ferrando	Universitat de València
Examinateurs	Katarzyna Krupa	Università degli Studi di Brescia
	Arnaud Mussot	Université de Lille
	Dmitry Skryabin	University of Bath
	Alessandro Tonello	Université de Limoges
Directeurs de thèse	Matteo Conforti	Université de Lille
	Alexandre Kudlinski	Université de Lille

REMERCIEMENTS

Je tiens tout d'abord à remercier Marc Douay, directeur du laboratoire PhLAM de l'Université de Lille, pour m'avoir permis de réaliser cette thèse et veiller sur son bon déroulement.

J'adresse aussi mes remerciements aux membres du jury qui ont accepté de lire et réviser mes travaux de thèse. En particulier, je voudrais remercier Costantino de Angelis, professeur à l'Université de Brescia et Albert Ferrando, professeur à l'Université de Valencia, qui ont accepté d'être rapporteurs de cette thèse, mais aussi Dmitry Skryabin, professeur à l'Université de Bath, Alessandro Tonello, maître de conférences à l'Université de Limoges et Katarzyna Krupa, chercheuse à l'Université de Brescia.

Un très grand merci est dirigé à mes encadrants : à Matteo Conforti pour sa patience et ses indications toujours pertinentes, ainsi que pour ses conseils très instructifs pour améliorer mon Français et me présenter le bon côté d'habiter au Nord de la France. Un énorme merci également pour son aide pendant les premières semaines à Lille, car sans sa bienveillance je n'aurais jamais réussi à m'y installer. À Alexandre Kudlinski, qui m'a montré l'importance de bien communiquer et a même osé me laisser faire quelques expériences. Je voudrais aussi remarquer que sans lui, les expressions plus courantes de la langue française seraient restées inconnues pour moi. À Arnaud Mussot, pour l'énergie qu'il arrive à transmettre au groupe et qui nous encourage à toujours aller plus loin. Merci à vous trois pour m'avoir accepté dans votre groupe, c'était un énorme plaisir de travailler avec vous et vous allez rester pour moi un modèle à suivre.

Maintenant c'est le moment de remercier les gens qui ont intégré le groupe Zobicon pendant ma thèse : à Gang Xu pour nos visites périodiques au restaurant chinois, à Tomy Marest et ses discussions quasi-philosophiques sur les quasi-solitons, à François Copie pour me montrer comment me rendre à la montagne la plus haute du coin, à Flavie Braud pour son aide dans la découverte de Lille au début de ma thèse, à Abdelkrim Bendhamane pour ses visites au bureau à l'heure du goûter. Merci aussi aux marins qui ont croisé le triangle des Bermudes : à Florent Bessin pour me montrer que c'est possible d'aimer la pluie et le vent, et à Corentin Naveau, le prochain guru des carbonades flamandes.

Merci aussi aux autres membres du groupe photonique, à Maryna pour les shots de vodka auxquels on ne peut pas échapper, à Damien pour toujours rester jusqu'à au bout, à Patrick pour nous présenter le camarade Staline qui fait du Kendo, et à Monika, Rémi,

Benjamin, Jean, Aurélie, Laurent, Olivier, Arsène, Stéphane, Géraud… avec qui j'ai pu passer des bons moments.

Dans ces remerciements je ne peux pas oublier Gilbert Martinelli, qui m'a fait confiance pour donner des cours. Merci pour ton insistance pour toujours regarder le côté physique des problèmes. Je ne peux pas non plus oublier Rémy, mon collègue de tranchée avec qui j'ai pu partager des moments très drôles.

Je voudrais aussi remercier Marie, Tobias, Alexey, Ramón, Roman et Elena, avec qui j'ai partagé pas mal de moments et discussions.

En aquests agraïments, no puc evitar fer una menció especial a Albert i Carles. Gràcies perquè sense vosaltres mai hauria arribat a conèixer l'òptica no lineal. Gràcies pels vostres sempre encertats consells.

Moltes gràcies també a la meua família i qui quasi ho són (Paco i Estefania), qui no han dubtat en creuar mitja Europa per donar-me suport.

Gràcies Vanessa per sempre entendre'm i donar-me ànims per a continuar. Aquesta tesi també és teua.

Nonlinear propagation in optical fibers: from soliton radiations to multimode instabilities

Abstract: The main goal of this thesis is the investigation of nonlinear light propagation in optical fibers. We have focused on two kinds of problems: solitons in single-mode fibers and multimode light propagation in graded index (GRIN) fibers. Solitons are short and intense light pulses which remain localized during propagation. They appear as maxima of intensity (called bright soliton) in the anomalous dispersion regime or intensity dips on a continuous wave (CW) background in normal dispersion (dark solitons). When their carrier frequency is close to the zero dispersion wavelength (ZDW) or when fiber's birefringence is taken into account, solitons can interact with weak waves and generate new frequencies. We have studied theoretically the efficiency of these processes in the case of dark solitons propagating close to ZDW and bright solitons in a highly birefringent fiber. The outcomes of these analysis have been validated experimentally.

In the second part of this thesis, we increase the degrees of freedom by using multimode fibers. Light propagation in multimode fibers entails a spatiotemporal dynamics which is still far to be fully understood. An effect arising in GRIN fibers is self-imaging, a process in which the spatial beam injected at the input replicates itself periodically along the fiber, creating a grating by virtue of the silica's Kerr effect. Due to this periodic behavior, when a CW propagates in a multimode fiber, some frequencies become unstable and they are amplified (a process called geometric parametric instability). We have characterized the pattern of unstable frequencies when a periodic variation of the fiber diameter is made. We also present a reduced one dimensional model which is able to mimic the spatiotemporal dynamics of light in a multimode GRIN fiber.

Keywords: Temporal optical solitons; Nonlinear optics; Optical fiber; Modulation instability; Multimode fiber; Dispersive waves.

ABSTRACT

Propagation non-linéaire dans les fibres optiques: solitons, ondes dispersives et instabilités multimodes

Resumé: Ces travaux de thèse portent sur l'étude de la propagation non-linéaire de la lumière dans les fibres optiques. Nous nous sommes concentrés sur deux types de problèmes: les solitons dans les fibres monomodes et la propagation de la lumière multimode dans les fibres à gradient d'indice. Les solitons sont des impulsions lumineuses courtes et intenses qui restent localisées lors de la propagation. Ils apparaissent sous la forme d'un maximum d'intensité (appelé soliton brillant) dans le régime de dispersion anormale, ou d'un trou d'intensité sur un fond continu en dispersion normale (soliton sombre). Lorsque leur fréquence de porteuse est proche de la longueur d'onde de dispersion nulle ou que la biréfringence de la fibre est prise en compte, les solitons peuvent interagir avec des ondes de faible amplitude et générer de nouvelles fréquences. Nous avons étudié théoriquement l'efficacité de ces processus dans le cas de solitons sombres qui se propagent près de la longueur d'onde de dispersion nulle et de solitons brillants dans une fibre fortement biréfringente. Les résultats de ces analyses ont été validés par des expériences.

Dans la deuxième partie de cette thèse, nous augmentons le nombre de degrés de liberté en utilisant des fibres multimode. La propagation de la lumière dans les fibres multimodes s'acompage d'une dynamique spatio-temporelle encore loin d'être complètement comprise. Un effet qui se produit dans les fibres GRIN est le l'auto-imagerie, un processus dans lequel le faisceau spatial injecté à l'entrée se réplique périodiquement le long de la fibre, créant un réseau d'indice grâce à l'effet Kerr de la silice. En raison de ce comportement périodique, quand une onde continue se propage dans une fibre multimode, certaines fréquences deviennent instables et sont amplifiées (processus appelé instabilité paramétrique géométrique). Nous avons caractérisé le motif des fréquences instables lorsqu'une variation périodique du diamètre de la fibre est réalisée. Nous présentons également un modèle unidimensionnel capable d'imiter la dynamique spatio-temporelle de la lumière dans une fibre multimode.

Mots clés: Optique non-linéaire; Fibres optiques; Solitons; Ondes dispersives; Fibres multimode; Instabilité modulationelle; Instabilité paramétrique.

Contents

INTRODUCTION

The effects explained by nonlinear optics are not commonly encountered in our daily life. In our usual experience, light does not change the properties of a medium when it goes through it. However, when the intensity of light is increased, the optical characteristics of a material may be modified due to light propagation. This property of light-matter interaction was almost hidden before the construction of the first working laser by Maiman in 1960 [1]. The laser paved the way to the observation of second harmonic generation using a quartz crystal by Franken [2], and to a posterior full explanation by Armstrong [3]. Both works gave birth to the field of nonlinear optics. Right after, numerous experimental realizations of nonlinear phenomena were carried out: the dependence on the intensity of light of the refractive index [4], Brillouin scattering [5] or degenerated four wave mixing [6] to cite some of them.

Some years later, optical fibers with low losses were available [7]. Indeed, not a longer time after, the potential of optical fibers to become a workhorse of nonlinear optics was being exploited. In just a few years, Raman scattering [8], [9], stimulated Brillouin scattering [10] and Self-Phase modulation [11] were observed using as a nonlinear material a silica made fiber (see references [12], [13] for a more detailed historical approach). Among the plethora of nonlinear effects taking place in fibers, two of them attracted our attention: solitons and modulation instability.

Solitons

Solitons are solutions of nonlinear equations representating a wave which keeps its form and remains localized. Notably they are not altered by collisions, unless a phase shift [14]. The name soliton was first coined by Zabusky and Kruskal [15] due to its close similarity to a particle. This kind of waves is ubiquitous in many physical fields such as Bose-Einstein

Condensates [16]–[18], hydrodynamics [19] and biological systems [20].

Solitons also appear in many optical systems, both in the spatial and in the temporal domain. Some remarkable exemples in the spatial domain are found in photorefractive crystals [21], nonlocal media [22], in the transverse plane of a photonic crystal fiber (PCF) [23] or discrete waveguides [24]. Whereas, the most notable case in time domain are single-mode optical fibers.

Initially proposed by Hasegawa [25], optical temporal solitons are localized structures in time domain. They are characterized by the perfect balance between nonlinearity and linear distortion produced by dispersion. Temporal solitons in optical fibers were initially observed by Mollenauer [26] and attracted much attention because of their potential application in long-haul optical telecomunications [27]. Although timing jitters produced by small carrier frequency fluctuations due to amplification (Gordon-Hauss effect [28]) or produced by Raman effect [29] significantly reduced the capacity and reachable distance of communication systems based on solitons [30], [31], they are attracting a renewed interest to conform future telecommunication systems [32], [33].

Besides their potential use in telecommunications, solitons play a crucial role in broadband sources. After the discovery of supercontinuum in PCF by Ranka [34], it was found that the interaction of solitons with other waves was at the origin of the broad spectrum [35] and they played a crucial role to explain this phenomena. These kind of interactions have attracted much attention since almost a decade ago and it is still an active field of research.

Modulation Instability

A continuous wave (CW) is the simplest non-trivial solution of wave equation describing light propagation in an optical fiber. However, it may be unstable due to modulation instability (MI) [36]. MI appears as a temporal modulation of the constant background whose amplitude increases following an exponential fashion. MI is present in many branches of physics, such as plasma physics [37], hydrodynamics [38] and Bose-Einstein Condensates [39] to cite some of them. In fiber optics, among all conditions where MI is triggered, the most common is anomalous dispersion regime [40]. It is also observed in normal dispersion in presence of higher order dispersion [41], fiber birefringence [42], multiple spatial modes [43] or if an external variation of parameters is applied [44]. The latter case is also called parametric instability or parametric resonance.

Parametric resonance (PR) is a well-known phenomenon taking place in systems where

parameters are varied in a periodic manner. A classical case is a pendulum whose string's length is changed periodically. Depending on the oscillator parameters, the system may be unstable and oscillations become unbounded.

Historically, one of the pioneering studies of PR was carried out by M. Faraday, who studied the formation of standing waves on the surface of a liquid in a closed vibrating receptacle, a phenomenon known as Faraday instability [45]. Faraday instabilities also manifest in a huge variety of physical settings [46], such as Bose-Einstein condensates [47]–[51], granular systems [52], [53], colloidal suspensions [54], mechanical systems [55] and chemical process [56] to cite some of them.

In optics, a CW may be also unstable due to PR when an external parameter is varied periodically. This external forcing can result from periodic amplification [57], dispersion [44], [58]–[62] or nonlinearity [63], [64]. The periodic evolution of nonlinearity can be self-induced in highly multimode graded-index (GRIN) fibers. Indeed, such fibers exhibit a periodic self-imaging of the injected field pattern due to the interference between the different propagating modes [65]. This is due to the fact that the propagation constants of the modes are equally spaced [66]. This creates a periodic evolution of the spatial size of the light pattern and therefore induces a periodic evolution of the effective nonlinearity in the propagation direction [67], [68]. Recent experiments showed that PRs produced by GPI can reach detunings from the pump in the order of hundreds of Terahertzs [69].

Objectives and organization of this manuscript

The present manuscript is divided in three parts, and each part in different chapter.

The first part is conceived to introduce the basic physical concepts. In the first chapter, physical mechanisms involved in light propagation in optical fibers are depicted. We shall explain the structure of the electric field, the origin of dispersion and nonlinearity. In the second chapter, single-mode solitons and their perturbations are explained from a physical point of view. Finally, in the third chapter, modulation instability produced in homogeneous and periodically varying fibers is explained.

The second part is devoted to optical solitons in single-mode fibers in presence of perturbations. The cases we shall analyze are the interactions of bright solitons in a birefringent PCF with a CW, and a dark soliton propagating near to zero dispersion wavelength (ZDW). In this later case, Cherenkov emission and the interaction with a linear wave are explained. In this part, all presented theoretical results are supported by numerical and experimental results.

In the last part, nonlinear multimode wave propagation in optical fibers is faced. We shall overview the recently published literature and present a detailed analysis of the model that we shall use. We will explain geometric parametric instability both in a constant core and a periodically modulated fiber. Finally, we will describe a (1+1)D model capable to mimic the dynamics of light propagating in a GRIN fiber.

Part I

Fundamentals of light propagation in optical fibers

CHAPTER

ONE

PHYSICAL MECHANISMS INVOLVED IN LIGHT PROPAGATION

Contents

The aim of chapter 1 is to give an overview of the general background needed to fully understand this manuscript. In section 1.1, the structure of a fiber and the light's confining mechanism are depicted. In section 1.2, the general form of the electric field is discussed and the most relevant approximations are explained. In section 1.3, the effects related to linear propagation are shown. In section 1.4, the most remarkable nonlinear effects and their origin are presented. In the last section 1.5, some important kinds of fiber and their most crucial characteristics are defined.

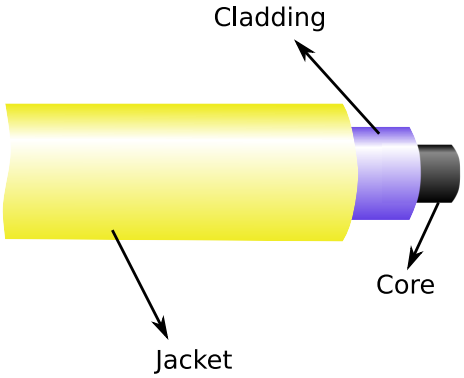

Figure 1.1: Schema of the fiber's general structure.

1.1 General structure of fibers

Optical fibers are dielectric waveguides which deliver electromagnetic radiation within a spectral range lying from visible to near infrared. They are mainly made of silica, although they also can be produced using lead silicates, chalcogenides, and bismuth oxide glasses, to name a few [40]. The physical mechanism underlying light confinement inside the guide is total internal reflection [70]. The most paradigmatic example of fiber is step-index, whose structure is composed of three well-differentiated concentric cylindrical regions (see Fig. 1.1) with different optical properties. The first region is the core, which is situated at the center of the fiber. The most part of the traveling energy is confined inside this region. The second part is called the cladding, which surrounds the core. This second stratum must have a refractive index strictly lower than the core in order to fulfill the conditions of total internal reflection and allow light guiding. In order to achieve this property, the core is doped with germanium, whose effect is to slightly increase its refractive index. Finally, there is the jacket wrapping the core and cladding. This last layer is conceived to protect the fiber from mechanical stress and it is optically isolated. Its presence is omitted along the whole manuscript since its purpose is only to protect the fiber and it does not affect the physical phenomena under investigation.

1.2 General structure of the Electric Field

Light propagation in an optical fiber is described by Maxwell's equations, which govern the electric (**E**) and magnetic (**B**) fields. In absence of free currents and charges, the full description can be reduced to only one of the two fields, that we choose without loss of

generality to be **E**.

The electric field is considered as a confined wave propagating forward along the z-axis. Note that under this assumption backward propagating fields produced by linear scattering, nonlinear coupling or non-guided radiation are neglected.

In addition, the considered guides will be assumed to have a small difference of refractive index between core and cladding. This hypotesis is known as weakly-guiding approximation [70]. Within this assumption, the different components of **E** will not be linearly coupled, although they could interact via nonlinear terms as we shall see in the second part of this manuscript.

The polarization components of the electric field can be split in two different parts, one perpendicular and the other paralel to the direction of propagation (z) [70] :

$$\mathbf{E}(x,y,z,t) = \mathbf{E}_{\perp} + \mathbf{E}_{z}. \tag{1.1}$$

It can be shown that $|\mathbf{E}_{\perp}| \gg |\mathbf{E_z}|$, hence **E** is considered to lie in the transverse plane of propagation. The spatial distributions of the electric field in this plane are called spatial modes $F(x,y)$. These distributions are solution of Maxwell equations and have to verify the boundary conditions imposed by the waveguide geometry. For example, in the step-index fiber, light have to be confined in the core and the electric field must go to zero in the cladding. The modes form a base and they can be used to expand and to fully describe the guided electric field **E** [71]. Using the translational invariance of fibers, a monochromatic electric field **E** can be written as:

$$\mathbf{E}(x,y,z,t) = \sum_{n} A_n(z) F_n(x,y) e^{i(\beta_n z - \omega_0 t)} \mathbf{u}_{\perp} + c.c, \tag{1.2}$$

where ω_0 is called the carrier frequency of the field, $c.c$ denotes complex conjugate, $A_n(z)$ is the amplitude of the n-th mode and β_n is the propagation constant, which is the conserved quantity associated to continuous translation symmetry of the fiber [70]. This last quantity plays a main role in the description of light propagation since it relates frequency with wave-number. The knowledge of this relation tells us crucial information such as phase velocity, group velocity, group velocity dispersion, ... as we will see in section 1.3. The propagation constant depends on the material, the guide and nonlinearity. If the field is monochromatic, and there is not coupling between modes (neither linear nor nonlinear), evolution in z is found by multiplying $A_n(z)$, which is constant due to the z-invariance of the modes, by the phase factor $\exp(i\beta_n z)$. Nevertheless, in real fibers, the modes are coupled and they may exchange energy. Modes interact via two different mechanisms:

by linear coupling, whose origin is small bending or imperfections of the waveguide or nonlinear interactions, due to the nonlinear nature of refractive index. In this manuscript, we will consider fibers which do not couple modes linearly and only nonlinear interactions between modes will be taken into account.

In waveguide theory is common to write β_m as a function of an effective refractive index ($n_{eff,m}(\omega)$):

$$\beta_m(\omega) = \frac{\omega n_{eff,m}(\omega)}{c}. \tag{1.3}$$

A certain mode is guided by total internal reflection if it verifies the condition $n_{clad} < n_{eff,m} < n_{core}$. Depending on the number of guided modes, fibers are classified in two main groups: single-mode, when there is only one guided mode and multimode, when there are more than one guided modes.

Equation (1.2) describes a strictly monochromatic electric field. If the electric field **E** has a finite spectral band, this expression should be modified in the following way:

$$\mathbf{E}(x,y,z,t) = \sum_n A_n(z,t)F_n(x,y)e^{i(\beta_n z-\omega_0 t)}\mathbf{u}_\perp + c.c. \tag{1.4}$$

The construction is quite similar, but note that now $A(z,t)$ depends also on t. This function is called envelope and it is a complex function whose bandwidth is much smaller than the carrier frequency ($|\Delta\omega| \ll \omega_0$). Then, the time dependence of Eq. (1.4) is described by the product of two functions, one varying at the carrier frequency ($e^{-i\omega_0 t}$) and another one which varies in a slower fashion and is called envelope. The approximation of considering two well-differentiated time scales is named slowly varying envelope approximation (SVEA) [72] , which can be mathematically written as $|\partial_t A| \ll \omega_0|A|$.

1.3 Linear effects: Dispersion

Interaction between light and matter is described by the macroscopic polarizability (**P**). If we assume a local response, this quantity can be expressed as a power series of the electric field [73]:

$$\mathbf{P}(\mathbf{r},\omega) = \epsilon_0(\chi^{(1)}(\omega)\cdot\mathbf{E} + \chi^{(2)}(\omega)\cdot\mathbf{EE} + \chi^{(3)}(\omega)\cdot\mathbf{EEE} + ...), \tag{1.5}$$

where $\chi^{(n)}(\omega)$ is a $(n+1)$-dimensional tensor describing the material properties named susceptibility. When **E** is weak enough, it is safe to keep only up to first order in the expansion. This first order approximation is the supporting basis of all the physics that can

be found in linear optics. The susceptibility $\chi^{(1)}$ is a function of frequency and it is related to the refractive index by the expression:

$$n^2(\omega) = 1 + Re(\chi(\omega)). \tag{1.6}$$

One important feature of linear light propagation is that the spectral content of the field will not be altered. The dependence on frequency of the refractive index far from resonances can be obtained by the Sellmeier formula [40]:

$$n^2(\omega) = 1 + \sum_j \frac{B_j \omega_j^2}{\omega_j^2 - \omega^2}, \tag{1.7}$$

where B_j and ω_j are coefficients depending on the material. In the case of germanium doped silica, which is the material consitituting most optical fibers, these coefficients are reported in Ref. [74]. The dependence on frequency of the refractive index makes the propagation constant frequency-dependent. The analytic form of this dependence is seldom known, since it is a function of guide geometry and its material composition. Nevertheless it can be developed as a Taylor series around the carrier frequency ω_0:

$$\beta(\omega) = \beta_0 + \beta_1(\omega - \omega_0) + \frac{\beta_2}{2}(\omega - \omega_0)^2 + \frac{\beta_3}{3!}(\omega - \omega_0)^3 + ... \quad , \quad \beta_m = \frac{d^m \beta(\omega)}{d\omega^m}\Big|_{\omega=\omega_0}. \tag{1.8}$$

The coefficients of the polynomial expansion are related to physical quantities. β_0 is related to the phase-velocity of the carrier frequency and β_1 and β_2 are related with the group-velocity and group velocity dispersion (GVD) respectively:

$$\frac{d\beta(\omega)}{d\omega} = \frac{1}{v_g} \quad , \quad \beta_2(\omega) = \frac{d^2\beta(\omega)}{d\omega^2}. \tag{1.9}$$

As it will be shown in coming chapters, GVD plays a fundamental role in light dynamics in optical fibers. Dispersion orders higher than 2 are called higher order dispersion (HOD). When HOD coefficients are present, the coefficient β_2 is a function of ω. Three different regimes are defined as a function of the sign of β_2:

- $\beta_2 = 0$: group velocity is an extrema, these points are called zero dispersion wavelength (ZDW). In conventional step-index fibers it is situated near 1300 nm but it may be found near 800 nm in special cases like photonic crystal fibers or around 1550 nm in dispersion shifted fibers (DSF).

- $\beta_2 < 0$: The group velocity increases with ω, this regime is called anomalous dispersion. In this regime bright solitons are found. They are going to be carefully studied in Chap. 4.

- $\beta_2 > 0$: The group velocity decreases with ω, this dispersion regime is known as normal dispersion. In this dispersion regime we will find dark solitons, which will play a main role in Chap. 5.

The physical effect of a group velocity dependence on ω is that the spectral components of a pulse travel with different velocities, producing a temporal distortion of the pulse.

1.4 Nonlinear effects: third order susceptibility

When the electric field is intense enough, the first order approximation of material response made in the last section is no longer valid, hence higher order terms must be included to properly describe light-matter interaction. When higher order terms of the polarizability are taken into account, processes involving several photons are allowed and as a consequence, the spectral content of the field may change.

The first contribution to nonlinear macroscopic polarizability in Eq. (1.5) is the second order susceptibility $\chi^{(2)}$. This contribution is responsible for a wide variety of relevant physical effects, such as second harmonic [2] and sum frequency generation. However, fused silica is a centro-symmetric material, thus the second-order nonlinearity strictly vanishes [75]. Silica centrosymmetry can be broken in optical fibers by special techniques such as thermal [76] or optical [77] poling, but these kind of effects are not considered in this manuscript.

The next contribution to nonlinear polarizability is $\chi^{(3)}$. The most prominent effects originated by this term are third harmonic generation (THG), four-wave mixing (FWM), self-phase modulation (SPM) and Raman effect [73]. Depending on the time scale of the reponse, nonlinear processes are classified in two groups: instantaneous and delayed response effects.

1.4.1 Instantaneous Response

This contribution is associated to the electronic response of the material. Its effect is seen if the electric field is expressed as $E = \frac{1}{2}(Ae^{-i\omega_0 t} + A^* e^{i\omega_0 t})$, where A is a complex number.

Consequently nonlinear polarizability writes as:

$$P^{(3)} = \epsilon_0 \chi^{(3)} (A^3 e^{-i3\omega_0 t} + 3|A|^2 A e^{-i\omega_0 t} + c.c) \tag{1.10}$$

The first term is related to THG, but in fiber optics is not observed unless special conditions are considered [78], [79] hence its contribution will be neglected. If Eqs. (1.10) and (1.6) are merged, the resultant physical effect is a refractive index depending on the intensity:

$$n(\omega) = n_l(\omega) + \bar{n}_2 \|A\|^2, \tag{1.11}$$

where $n_l(\omega)$ is the linear contribution to the refractive index and $\bar{n}_2 = 3/8 Re(\chi^{(3)}) n_l^{-1}$. Materials are classified as focusing ($n_2 > 0$) or defocusing ($n_2 < 0$) relying upon the sign of n_2. In the wavelength range we consider, silica is a focusing material [80].

When variations of refractive index due to intensity seen by a field are produced by the field itself, the process is called SPM, while when there is a different field at the origin of the induced changes, the effect is named cross-phase modulation (XPM). Both XPM and SPM are particular cases of a more general process called four-wave mixing (FWM), which consists on the annihilation of two photons with frequencies ω_1 and ω_2 to generate two new photons with frequencies ω_3 and ω_4. The interaction is elastic, thus energy and momentum are conserved. This means there are a frequency ($\omega_1 + \omega_2 = \omega_3 + \omega_4$) and wavenumber ($\beta^{(1)} + \beta^{(2)} = \beta^{(3)} + \beta^{(4)}$) conservation laws. In nonlinear optics the conservation of wavenumber is known as phase-matching.

1.4.2 Raman effect

Photons can also interact with a $\chi^{(3)}$ material via nonlinear inelastic scattering, which means that involved photons lose some energy which is transfered to the medium. In optical fibers, the most imporant effects are Raman and Brillouin scattering. In our case, we will only consider Raman effect. This phenomena, first discovered by C.V. Raman [81] in 1928, was observed for the first time in optical fibers by Stolen *et al.* [8] in 1972. It consists on the interaction of photons with molecular vibrations of silica. From a quantum mechanical point of view, an incident photon with frequency ω_i excites a virtual level of energy, after decays to a lower energy photon ω_e, and thus excites a mode of vibration of the crystalline structure with frequency Ω_R, a phonon. In Fig. 1.2 an schema of the spontaneous Raman scattering is displayed. In nonlinear media such as gasses, this effect produces discrete lines, but due to the amorphous nature of silica, the generation of new

frequencies is a continuum extending over more than 40 THz. The Raman reponse can be approximated to the analytic expression in frequency domain as:

$$h_R(\Delta\omega) = \frac{\tau_1^2 + \tau_2^2}{\tau_1^2 \tau_2^2} \frac{1}{(\tau_2^{-1} - i\Delta\omega)^2 - \tau_1^{-2}}, \tag{1.12}$$

or in temporal domain:

$$h_R(t) = (\tau_1^{-2} + \tau_2^{-2})\tau_1 e^{-t/\tau_2} \sin(t/\tau_1)\Theta(t) \tag{1.13}$$

where $\tau_1 = 1/\Omega_R = 12.2$ fs, being Ω_R the vibrational frequency of molecules and $\tau_2 = 32$ fs the damping time of vibrations. $\Theta(t)$ is the Heaviside function, which ensures the causality of the response function. In Fig. 1.2(b) the imaginary part of Eq. (1.12) is represented. From this representation we can see that the imaginary part of the Raman reponse extendeds continuously and has a maximum (minimum) near 13 (-13) THz. In Fig. 1.2(c), Raman reponse in time domain written in a explicit manner in Eq. (1.13) is plotted. The Raman effect becomes important in two principal cases. On the one hand, when a certain power threshold is reached, this process becomes very efficient and can transfer energy to another frequency, which may become as energetic as the initial pump, giving birth to a cascade process. On the other hand, when characteristic time scale of involved phenomena is comparable to nonlinear Raman reponse (pulses of less than 1 ps), the energy transfer takes place inside the bandwidth of the pulse. A good example is the soliton self frequency shift [82], where a soliton reduces continuously its frequency.

1.5 Other kinds of fiber

In addition to step-index, there is a huge variety of fibers. Among all the types, in this manuscript we will make use of micro-structured fibers and graded-index (GRIN) fibers.

1.5.1 Micro-structured fiber

Step-index fibers discussed in section 1.1 do not give much freedom to taylor light propagation parameters, because the ZDW is close to the one of silica. This problem can be overcome by using microstructured fibers or photonic crystal fibers (PCF). These fibers are characterized by having a periodic structure on the transverse plane which enables light confinement. They were theoretically proposed in the 70s [83], however PCF were not experimentally available until 1996 [84].

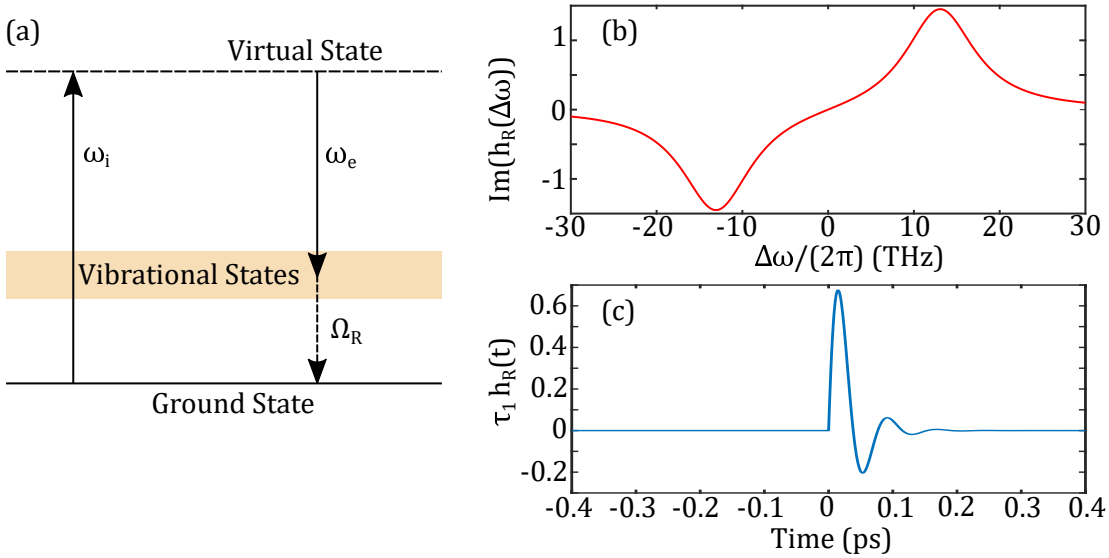

Figure 1.2: Raman Effect: (a) Sketch of the quantum mechanical picture of the Spontaneous Raman scattering. (b,c) Response function of Raman scattering in temporal and spectral domains.

There are two physical mechanisms lying beneath light propagation in PCF [85]:

1. **Total internal reflection:** The most emblematic example is the holey-fiber. The structure of fibers using this guiding mechanism consists on a periodic array of air holes on the transverse plane with a defect at the center, where light is confined. The physical mechanism behind light propagation is total internal reflection because the holey structure has an equivalent refractive index lower than the center silica defect. This structure increases the number of degrees of freedom and allows to precisely control birefringence [86], dispersion [87], [88] and mode area [89].

   Holey fibers have played a leading role in the design of broad spectrum sources [34], which are based on supercontinuum generation [90]. In the Ranka's experiment, a PCF with hexagonal lattice of circular holes was employed, a structure formerly studied by Ferrando *et al.* [91].

2. **Photonic band-gap guiding**: This was the initial mechanism proposed to confine light in the fiber, but waveguides relying on this physical process were fabricated some years after the holey fibers [92]. It is based on the fact that a periodic transverse structure produces forbidden bands [93]. This kind of fiber can be very interesting because they allow light guiding in air, reducing considerably nonlinear effects and

losses.

1.5.2 GRIN fibers

A very important kind of waveguide studied in this manuscript is GRaded-INdex (GRIN) fibers. Their most important difference with respect to step-index fibers is that instead of having a constant core index, their refractive index is maximum at the center and it decreases when approaching to the cladding. A sketch of the refractive index profile is shown in Fig. 1.3 (a). The refractive index $n(r,\omega)$ has a parabolic shape for $r < R$ and constant inside the cladding $(r > R)$. The relative index difference (Δ) is defined as:

$$\Delta = \frac{n_{core}^2 - n_{clad}^2}{2n_{core}^2}, \tag{1.14}$$

where n_{core} (n_{clad}) is the refractive index at the core center (cladding).

A widely used approximation allowing to simplify the theoretical understanding is to consider the core to have an infinite radius. In Fig. 1.3 (a) the index profile corresponding to the infinite readius approximation is shown with a black dashed line. We will see after that this approximation is equivalent to consider a 2-D harmonic quantum potential. Within this limit, the fiber modes can be written in polar coordinates as [66]:

$$F_{m,p}(\rho,\phi) = \sqrt{\frac{p!}{\pi(|m|+p)!}}\frac{\rho^{|m|}}{\rho_0^{|m|+1}} exp\left(-\frac{\rho^2}{2\rho_0^2}\right) L_p^{|m|}\left(\frac{\rho^2}{\rho_0^2}\right) e^{im\phi}, \tag{1.15}$$

where $\rho_0 = R\lambda_0/(2\pi\sqrt{2\Delta}n_{core})$, m and p are two integers and $L_p^{|m|}$ are generalized Laguerre polynomials. The dispersion relation of the different modes can be obtained analytically, and it is approximated by the following expression:

$$\beta_g(\omega) \approx \frac{2\pi n_{core}(\omega)}{\lambda} - \frac{\sqrt{2\Delta}}{R}g \quad , \quad g = 2p + |m| + 1. \tag{1.16}$$

This dispersion relation is composed by two terms, the first one is associated to the contribution of material dispersion and the second one is exclusively due to the guide contribution.

One important idiosyncrasy of GRIN fibers is self-imaging. This effect consists in the replication of the input image with a period ξ. We can clearly see the self-imaging effect if

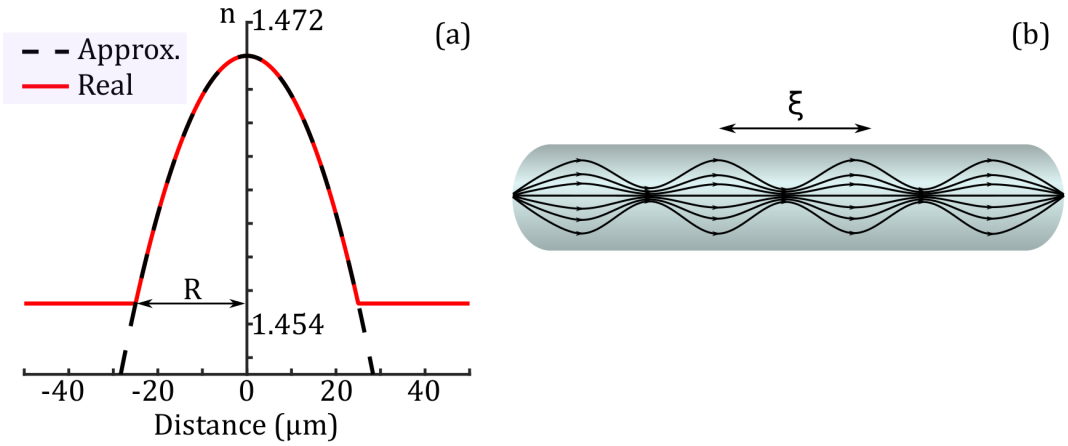

Figure 1.3: (a) Refractive index profile of a graded index fiber. Dashed line represents infinite core approximation and solid red line shows the real case. Parameters are $R = 25\ \mu$m and $\Delta = 10^{-2}$. (b) Self-imaging in a graded-index fiber, ξ is the self-imaging period.

the intensity of the field is calculated. Then, by using Eq. (1.2) and Eq. (1.16):

$$I(x,y,z) = \sum_{n,k>n} |F_n|^2 + 2F_nF_m \cos\left(\frac{2\sqrt{2\Delta}}{R}(k-n)z\right), \tag{1.17}$$

where only modes with the same m have been considered. The equation clearly shows that the intensity of the propagating field is an interference pattern between different modes with period $\xi = \pi R/\sqrt{2\Delta}$ [65]. Self-imaging is an exclusive characteristic of GRIN fibers and it is due to the fact that the difference $\beta_{g+1} - \beta_g$ does not depend on the mode number g. Figure 1.3(b) shows a ray path representation of a beam propagating in a GRIN fiber. It is shown how the beam experiences a periodic behavior with period ξ because the interference of modes.

Summary

- Step index are the most paradigmatic example of optical fibers. They are composed by three different regions: Core, cladding and jacket. All them have different optical properties.
- We have discussed the general structure of the electric field, and the most commonly employed approximations to describe it. The difference between multimode and single-mode fibers has been outlined.

- The dependence on the frequency of material refractive index is called dispersion. This effect is at the origin of many physical phenomena relevant for this manuscript, such as group velocity and group velocity dispersion amid others.
- We have exposed the nonlinear involved phenomena : Kerr and Raman effect.
- Other fibers than step-index have been described, being the most relevant photonic crystal and graded index fibers.

CHAPTER

TWO

SOLITONS IN NONLINEAR FIBER OPTICS

Contents

The aim of this chapter is to present temporal optical solitons in single-mode fibers [27] from a physical point of view. The chapter is organized as follows: in the first section, the generalized nonlinear Schrödinger equation is described, which is a general model describing light propagation in single-mode fibers. We will tell under which conditions solitons are found. In the second section, we describe the different kinds of solitons and under which conditions appear. Finally, in the third section, the physical effects arising from the perturbation of solitons are described.

2.1 Nonlinear Schrödinger equation

An electric field linearly polarized propagating in a single-mode waveguide can be expressed using the general form presented in Eq. (1.2):

$$E = F(x,y)A(z,t)e^{i(\beta(\omega_0)z-\omega_0 t)} + c.c. \tag{2.1}$$

where $F(x, y)$ is the field distribution of the fundamental mode in the transverse plane. The envelope $A(z, T)$ is described by the equation so called generalised nonlinear Schrödinger equation (GNLSE) [40]:

$$i\partial_z A + D(i\partial_T)A + \gamma A \int_0^\infty R(t')|A(t-t')|^2 dt' = 0, \tag{2.2}$$

where the first term $D(i\partial_T) = \sum_{n=2}^{\infty} \beta_n (i\partial_T)^n / n!$ is the dispersion operator, which is the inverse Fourier transform of $D(\omega) = \beta(\omega) - \beta_1(\omega_0)(\omega - \omega_0) - \beta_0(\omega_0)$, where $\beta(\omega)$ was defined in the previous chapter and it takes into account of the whole dispersion relation. Time (T) is defined in a reference frame traveling at the group velocity of the carrier frequency and it relates to time in the laboratory reference frame (t) through the transformation $T = t - \beta_1(\omega_0)z = t - z/v_g$. The coefficient γ, named nonlinear coefficient, is given by the following expression [40]:

$$\gamma = \frac{\omega_0 n_2}{c} \frac{\int_S |F(x,y)|^4 \mathrm{dS}}{\left(\int_S |F|^2 \mathrm{dS}\right)^2}, \tag{2.3}$$

being n_2 the nonlinear refractive index of the material which is equal to $3.2{\cdot}10^{-20}$ m^2/W in the case of silica. The parameter γ is proportional to the field confinement inside the fiber: the bigger is γ, the less power is needed to observe nonlinear effects. Its value ranges from 1-10 W$^{-1}{\cdot}$km^{-1} in standard fibers to 100 W$^{-1}{\cdot}$km^{-1} in PCF. The nonlinear response $R(t)$ can be expressed as the sum of the instantaneous (Kerr) and delayed (Raman) contributions:

$$R(t) = (1 - f_r)\delta(t) + f_r h_R(t). \tag{2.4}$$

The constant f_r is the fraction of Raman contribution which in fibers is equal to 0.18, $h_R(t)$ is the Raman response function given in the previous chapter and $\delta(t)$ is the Dirac delta distribution. This equation has successfully been used for modeling pulse propagation in fibers and it reproduces accurately the whole dynamics observed in phenomena such as supercontinuum generation [94].

When ω_0 is far from ZDW and the pulse is spectrally narrow, it can be considered that the GVD does not depend on the frequency ω (otherwise said, dispersion relation is truncated to second order in ω). Moreover, Raman effect can be neglected if the pulse is not too short nor too intense. Accounting for these approximations in Eq. (2.2), bring us to:

$$i\partial_z A - \frac{\beta_2}{2}\partial_T^2 A + \gamma |A|^2 A = 0. \tag{2.5}$$

Equation (2.5) is the well-known nonlinear Schrödinger equation (NLSE) and it is integrable by means of the inverse scattering transform (IST) [95]. One of the most striking properties of integrable systems solvable with IST is the existence of solitons, which in the simplest case are localized waveforms which propagate without deformation. Depending on the sign of the dispersion, the solitons are bright (anomalous dispersion) or dark (normal dispersion). The differences between the two kinds of solitons will be studied in sections 2.2 and 2.3, respectively. The properties of a soliton are related to the parameter N, which we call order of the soliton:

$$N^2 = t_0^2 \frac{\gamma P_0}{|\beta_2|}, \tag{2.6}$$

where t_0 is the characteristic duration of the pulse and P_0 is the peak power. This parameter takes into account the ratio between the nonlinear coefficient γ, the peak power of the pulse P_0 and dispersion (β_2 and t_0).

2.2 Bright solitons

Bright solitons are found in the anomalous dispersion regime ($\beta_2 < 0$). They appear as an intense and short pulse whose intensity vanishes when $T \to \pm\infty$. They are classified depending on their value of N. Solitons verifying N=1 evolve without changing their temporal and spectral shape and are called fundamental. The analytical expression describing their evolution in z is:

$$A(z,T) = \sqrt{P_0}\text{sech}\left(T\sqrt{\frac{|\beta_2|}{\gamma P_0}}\right)e^{i\frac{\gamma P_0 z}{2}}. \tag{2.7}$$

If N> 1, then the soliton is a periodic solution with period $L_{sol} = \frac{\pi N^2}{\gamma P_0}$ and are called higher order solitons. They can be seen as the superposition of several solitons with different powers and different durations. In Fig. 2.1, the evolution of a bright soliton of order N=2 is shown: we see how its behavior repeats periodically with z.

2.3 Dark solitons

Dark solitons exist in the normal dispersion regime ($\beta_2 > 0$). The intensity profile of a dark soliton is a dip over a continuous wave (CW) background. Its depth is a function of the grayness (ϕ), a parameter defined from $-\pi/2$ to $\pi/2$. In Fig. 2.2, the intensity of a dark soliton is shown for two different grayness values. Solid red curve represents $\phi = 0$

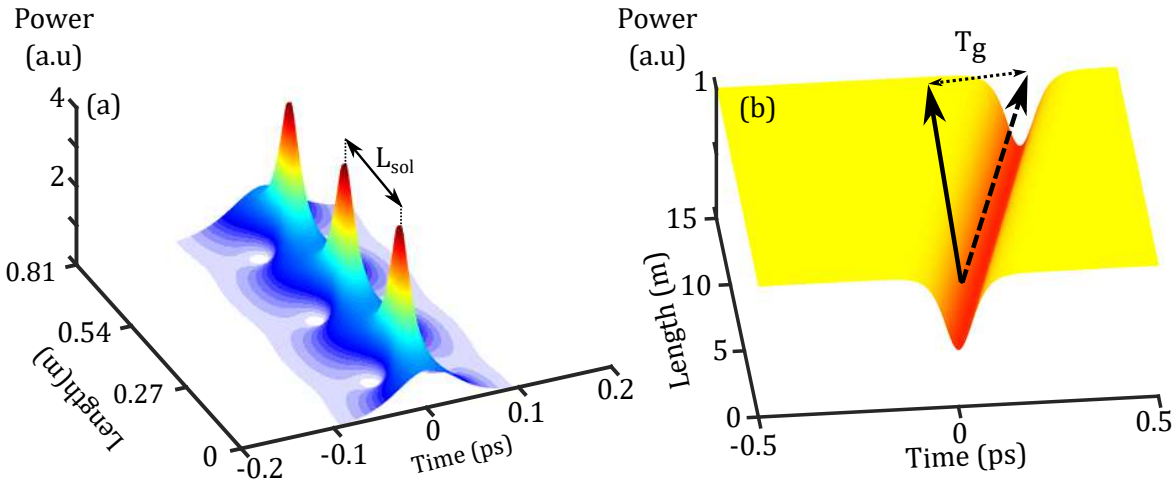

Figure 2.1: (a) Evolution of a higher order bright soliton in time domain. (b) Evolution of a dark soliton with grayness $\phi = \pi/8$ in time domain.

and the blue dashed curve the case where $\phi = -\pi/5$. In the particular case where the minimum intensity reaches zero ($\phi = 0$), the soliton is called black soliton. The analytic solution of a dark soliton is:

$$A(z,T) = \sqrt{P_0}\left[\cos(\phi)\tanh\left((T-\beta_{1sol}z)\sqrt{\frac{|\beta_2|}{\gamma P_0}}\cos(\phi)\right) - i\sin(\phi)\right]e^{i\gamma P_0 z}. \tag{2.8}$$

Dark solitons have a phase jump in the neighborhood of T=0. In figure 2.2 (b), this effect is shown for the values $\phi = 0$ and $\phi = -\pi/5$. In the case of a black soliton, the jump is abrupt while when $\phi \neq 0$ becomes smooth. Due to this temporal dependence of the phase, dark solitons are chirped.

The group velocity of a dark soliton depends on its grayness. As a consequence of the velocity mismatch between the soliton and reference frame, the soliton acquires a time delay respect to the background. This additional group velocity is given by the soliton parameters $\beta_{1sol} = \sqrt{\beta_2\gamma P_0}\sin(\phi)$. In Fig. 2.1 (b) the evolution of a gray soliton with $\phi = \pi/8$ is shown. The solid black arrow represents the velocity of the background and the dashed one the velocity of the soliton. We see that the soliton is delayed from its initial position by an amount of time T_g.

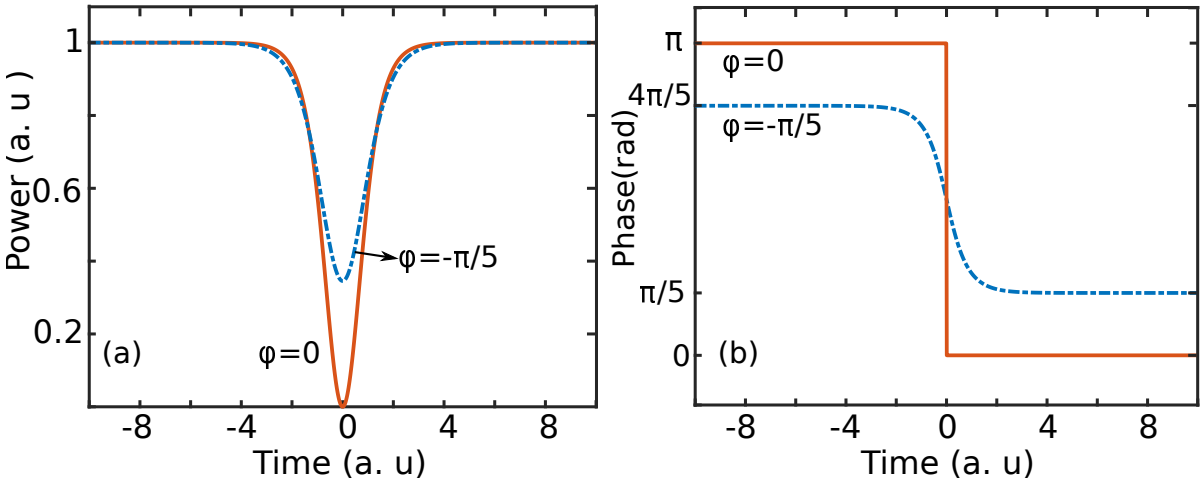

Figure 2.2: (a) Intensity of a black soliton (solid red line) and a gray soliton with $\phi = -\pi/5$ (dashed blue line). (b) Phase of a black soliton (solid red line) and a gray soliton with $\phi = -\pi/5$ (dashed blue line).

When the value N exceeds 1, then the initial pulse breaks into several solitons of different grayness [40]. Thus, the dark soliton breaks apart and do not form a periodic solution, as was the case for a bright soliton.

2.4 Perturbation of solitons

Equation (2.5) is valid when light propagates far from the ZDW. In this limit, solitons collide elastically with other solitons or linear waves. If we get closer to the ZDW, the truncation of dispersion up to second order is not longer valid and HOD must be included. When HOD is taken into account, solitons are not anymore solutions of the propagation equation, which physically translates in the possible interplay between a soliton and dispersive waves. Two different kinds of interaction appear when HOD is included: the emission of radiation by solitons and their interaction via FWM with linear waves.

2.4.1 Emission of radiation

Under the effect of perturbations, solitons can transfer energy to linear waves [96]. This process, known as emission of Cherenkov radiation [97], has been studied in the case of bright fundamental solitons [98]–[101] , dark solitons [102]–[106], higher order solitons [107] and bright solitons in multimode fibers [108].

The soliton can efficiently transfer its energy to a linear wave if they both share the same propagation constant, verifying momentum conservation (equivalently phase-matching). A good example to illustrate the process is to consider a bright soliton ($\beta_2 < 0$) propagating near the ZDW. The wavenumber of the soliton, given by Eq. (2.7) is $\gamma P_0/2$ and dispersion relation of linear waves is $D(\Omega) = \frac{\beta_2}{2}\Omega^2 + \frac{\beta_3}{3!}\Omega^3$, where $\Omega = \omega - \omega_0$, being ω_0 the carrier frequency of the soliton. For the sake of simplicity, dispersion is kept over to third-order, because the only condition to emit Cherenkov radiation is the existence of a ZDW. The phase matching condition is thus:

$$\frac{\beta_2}{2}\Omega^2 + \frac{\beta_3}{3!}\Omega^3 = \frac{\gamma P_0}{2}. \tag{2.9}$$

The frequency Ω_{rad}, which is a solution of Eq. (2.9) is the frequency of the radiated wave. From Eq. (2.9) we see that the role of β_3 is crucial, since without it, this equation has not real solutions.

A numerical solution of Eq. (2.2) without including Raman effect is shown in Fig. 2.3. The soliton has a duration of t_0= 45 fs and fiber parameters are $\beta_2 = -11.83 \cdot 10^{-3}$ ps^2/m, β_3 = 8.10·10^{-5} ps^3/m, λ_{ZDW} = 784 nm and γ=0.11 ·10^{-3} W^{-1}m^{-1}. In Fig. 2.3 (a) the spectral output (input) is shown with solid (dashed) curve. Dashed vertical line represents phase-matching condition, which perfectly predicts the emitted wavelength. In Fig 2.3 (b) the evolution in time domain is represented. The vertical dashed arrow represents the trajectory followed by the soliton, the arrow with slope $\beta_1(\Omega_{rad})$ represents the delay of a linear wave with frequency Ω_{rad} with respect to the carrier frequency frame.

2.4.2 Interaction between solitons and linear waves

In the presence of HOD [109] or birefringence [110], solitons can interact via FWM with linear waves and produce new frequencies. This interplay commonly takes place in supercontinuum generation [35], hence its understandig is crucial to conceive new broadband sources. This mechanism has been suggested as a way to achive all optical-switching [111], as a close physical analogy of event horizon in black holes [112], [113] and to perform a "cage" to trap dispersive waves [114]–[116]. In the simplest case, this process involves bright fundamental solitons, even thought it has been recently explored the possibility of using other kinds of solitons such as dark solitons [117] and higher order bright solitons [118]. The main difference between classical FWM and interaction of solitons and linear waves is that one of the involved fiels is a non-dispersing pulse instead of a CW. Unlike the CW, solitons have a dispersion relation which does not depend on ω. If we consider

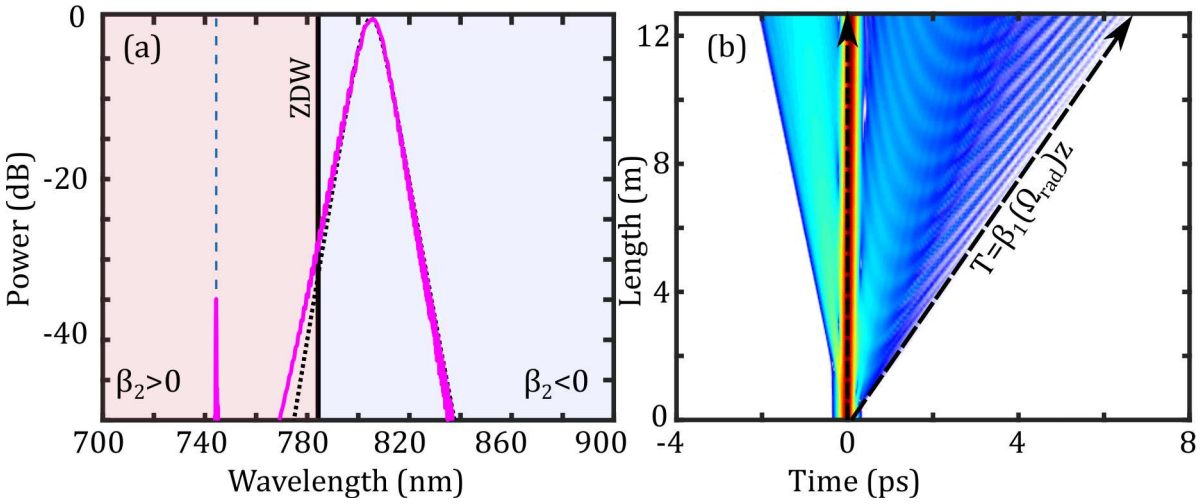

Figure 2.3: (a) Input (dashed line) and output spectrum (solid line) after propagation. (b) Emission of radiation by a bright soliton in time domain. Parameters: $t_0 = 45$ fs, $P_0 = 22.5$ W and $\lambda_{soliton} = 805$ nm. Fiber parameters at λ_0: $\beta_2 = -5.01 \cdot 10^{-3}$ ps^2/m, β_3=8.10·10^{-5} ps^3/m , $\lambda_{ZDW} = 784$ nm and $\gamma = 0.11 \cdot 10^{-3}$ W^{-1}m^{-1}.

only a process involving two photons from the soliton, one from a field with frequency ω_{in} and another one with frequency ω_g, then the two following phase-matching conditions [35] are found:

$$\beta(\omega_i) = \beta(\omega_g) \tag{2.10}$$

$$2\gamma P_0 = \beta(\omega_i) + \beta(\omega_g). \tag{2.11}$$

From the above relations we distinguish two kinds of interaction: on one hand, when the phase matching does not depend on the soliton parameters in Eq. (2.10). We will deeply study this process in the case of a interaction between dark solitons and a linear waves in Sec. 5.3. On the other hand when the phase matching condition is a function of the soliton phase in Eq. (2.11), it will be profoundly analyzed in chapter 4 in the special case where a bright soliton is orthogonally polarized to a CW.

An example of these interactions is shown in figure 2.4. The input is the superposition of a soliton at λ_{sol} =900 nm and a Gaussian pulse much weaker and longer in normal dispersion regime with $\lambda_{in} = 707$ nm. The spectrum of the input is shown in Fig. 2.4 (a) with a dashed black line. When both pulse propagate, they collide and a new frequency is produced. This process can be clearly seen in the temporal evolution plotted in Fig 2.4

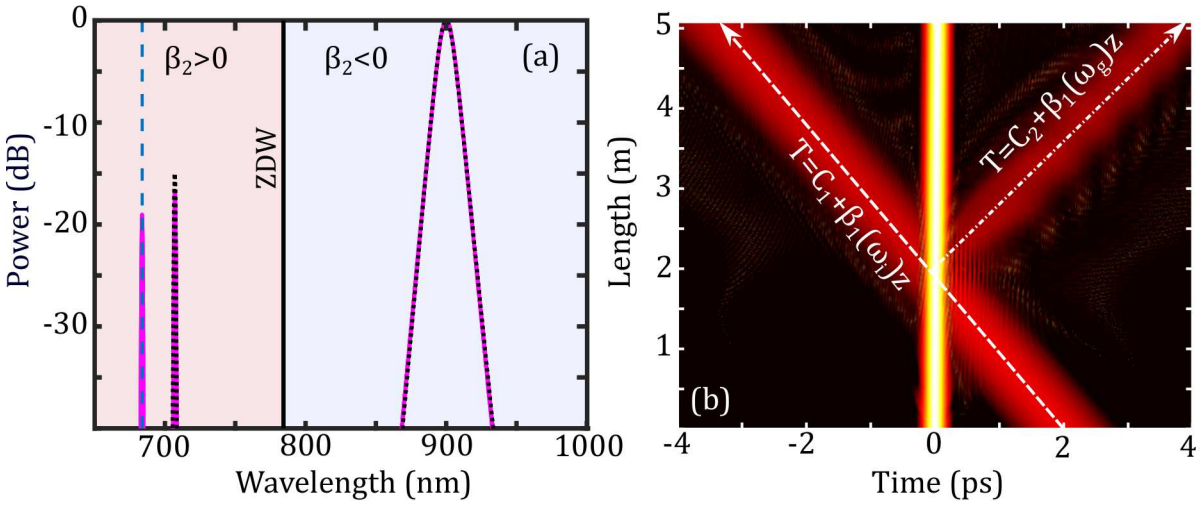

Figure 2.4: (a) Input spectrum (dashed) and output spectrum (solid) of the propagation of a soliton and a weak pulse. (b) Evolution of the interaction in the time domain. Dashed lines represent the trajectory of a linear wave with frequency ω_i and ω_g respectively. Parameters: $\lambda_{soliton} = 900$ nm, $\lambda_{in} = 707$ nm, t_0 =45 fs, and P_0 =112 W. Dispersion at $\lambda_{soliton}$: $\beta_2 = -25 \times 10^{-3}$ ps^2/m, β_3= 8.10·10^{-5} ps^3/m.

(b). We see that, when the two pulses temporally coincide, a third wave with a different velocity appears. The output spectrum of this process is shown in Fig 2.4 (a) with solid line. The vertical dashed blue line is the phase matching condition shown in Eq. (2.10), we see there is a perfect agreement between the theoretical prediction and numerical simulations.

Summary

- An equation for the temporal envelope of the electric field propagating in a single mode fiber has been presented. In the most general case takes into account Raman and Kerr effect and we will refer to it as GNLSE. When the model only takes into account Kerr nonlinearity and group velocity dispersion, the governing equation is called NLSE.
- NLSE has one class of solutions, which are called solitons. We have presented bright solitons, appearing in anomalous dispersion regime and dark solitons, which exist in normal dispersion regime.
- When perturbed, solitons can interact with dispersive waves via four wave mixing

or emit radiation via a mechanism known as Cherenkov radiation.

CHAPTER

THREE

INSTABILITY OF CONTINUOUS WAVE

Contents

A CW may be unstable when propagating in an optical fiber, which means that the initial wave may decay via FWM and generate new frequencies. The mechanisms triggering MI considered in the present chapter are twofold: the interplay of constant dispersion and nonlinearity, and parametric instability. The organization of the chapter is as follows: in the first section, a general framework to study the CW instabilities in the context of NLSE is derived. In the second section, MI generated in the scalar case of an homogeneous fiber is depicted. Finally, in the third section, the case of a medium with harmonically varying nonlinearity is described as an example of parametric instability.

3.1 Linear stability analysis

In this section, we perform a stability analysis that will set the basis to understand all the MI phenomena discussed along this thesis. The physical mechanism behind MI in optical fibers is the interplay between dispersion and Kerr nonlinearity, then even the most basic NLSE already describes MI for certain range of parameters, as it is shown in classical approaches [40]. However, the simplest equation does not exhibit all kind of instabilities

and effects described in the present manuscript, hence the employed model to illustrate the possible phenomena must be more general. We need to contemplate two crucial peculiarities: the first aspect is that studied phenomena involve large spectral regions, thus we need to consider a dispersion operator which takes into account all dispersive orders. The second particularity is that nonlinear wave propagation in multimode fibers can be reduced to propagation of light in medium with periodic nonlinearity [68], then a nonlinear coefficient γ which depends on z and has a period Λ should be considered. Therefore the most suitable starting point is the following generalized NLSE equation:

$$i\partial_z A + D(i\partial_T)A + \gamma(z)|A|^2 A = 0, \tag{3.1}$$

where $D(i\partial_T)$ is the dispersion operator and $\gamma(z)$ is a periodic function of z. The following form of $A(z,T)$ is supposed:

$$A(z,T) = \sqrt{P_0}(1+\epsilon(z,T))\mathrm{e}^{i\phi} \quad , \quad \phi = P_0 \int \gamma(z)dz. \tag{3.2}$$

$A(z,T)$ describes a CW with a small perturbation ϵ which verifies the condition $|\epsilon| \ll 1$. The supposed *ansatz* entails a subtle difference with MI in a homogeneous media: if we pay attention to ϕ, now it is a general function of z, instead of $\gamma P_0 z$ as it is found in classical linear stability analysis. After substituting the expression (3.2) in Eq. (3.1) and carrying out a linearization in ϵ, the following equation ruling the perturbation is found:

$$i\partial_z \epsilon + D(i\partial_T)\epsilon + \gamma(z)P_0(\epsilon + \epsilon^*) = 0. \tag{3.3}$$

Equation (3.3) can be solved if $\epsilon(z,T)$ is written in the following way:

$$\epsilon(z,T) = a(z)\mathrm{e}^{-i\Omega t} + b^*(z)\mathrm{e}^{+i\Omega t}, \tag{3.4}$$

where $\Omega = \omega - \omega_0$ is the frequency detuning from the initial CW with frequency ω_0. Coefficients $a(z)$ and $b^*(z)$ are two complex functions of z, whose evolution can be found by introducing Eq. (3.4) in Eq. (3.3). Then, grouping terms oscillating at the same frequency, a coupled system of equations is found:

$$i\frac{d}{dz}\begin{bmatrix} a \\ b \end{bmatrix} + \begin{bmatrix} D(\Omega)+\gamma(z)P_0 & \gamma(z)P_0 \\ -\gamma(z)P_0 & -\left(D(-\Omega)+\gamma(z)P_0\right) \end{bmatrix}\begin{bmatrix} a \\ b \end{bmatrix} = \begin{bmatrix} 0 \\ 0 \end{bmatrix} \tag{3.5}$$

We can simplify a little the obtained system by defining the following functions:

$$D_{even}(\Omega) = \sum_{n=1} \frac{\beta_{2n}}{(2n)!}\Omega^{2n} \quad , \quad D_{odd}(\Omega) = \sum_{n=1} \frac{\beta_{2n+1}}{(2n+1)!}\Omega^{2n+1}, \tag{3.6}$$

which are the even and odd symmetric parts of $D(\Omega)$. The dispersion operator in the Fourier domain can be written such as $D(\Omega) = D_{even}(\Omega) + D_{odd}(\Omega)$ and $D(-\Omega) = D_{even}(\Omega) - D_{odd}(\Omega)$. If a rotation of phase $(a, b) = (a, b)e^{iD_{odd}(\Omega)z}$ is performed, the following system of equations is found:

$$i\frac{d}{dz}\begin{bmatrix} a \\ b \end{bmatrix} + \begin{bmatrix} D_{even}(\Omega) + \gamma(z)P_0 & \gamma(z)P_0 \\ -\gamma(z)P_0 & -\left(D_{even}(\Omega) + \gamma(z)P_0\right) \end{bmatrix}\begin{bmatrix} a \\ b \end{bmatrix} = \begin{bmatrix} 0 \\ 0 \end{bmatrix}. \tag{3.7}$$

Note that, only even terms of dispersion relation play a significant role in the perturbation equation. There are two different mechanisms which can give rise to an unbounded behavior of (a, b). On one hand, effects of dispersion and a constant nonlinearity (i.e. $\gamma(z)$ =const). In this frame are included classical MI produced in anomalous dispersion regime and HOD terms. This regime is analyzed in section 3.2. On the other hand, when γ is a periodic function of z with period Λ. In this case, a new kind of instability arises, which we call parametric instability and will be deeply studied in section 3.3.

3.2 Modulation instability

When $\gamma(z)$ is a constant γ_0, Eq. (3.7) is a system of ordinary differential equations (ODEs) with constant coefficients. Within this limit, Eq. (3.7) is easily solved if functions $a(z)$ and $b(z)$ are expressed as $(a, b) = (C_1, C_2)e^{ikz}$, where C_1 and C_2 are two arbitrary constants. By introducing this *ansatz* in Eq. (3.7), the following algebraic system is obtained:

$$\begin{bmatrix} D_{even}(\Omega) + \gamma_0 P_0 - k & \gamma_0 P_0 \\ -\gamma_0 P_0 & -\left(D_{even}(\Omega) + \gamma_0 P_0 + k\right) \end{bmatrix}\begin{bmatrix} C_1 \\ C_2 \end{bmatrix} = \begin{bmatrix} 0 \\ 0 \end{bmatrix}. \tag{3.8}$$

In order to avoid trivial solutions for $C_{1,2}$, the system matrix must have a vanishing determinant, which lead us to the following condition over k:

$$k(\Omega) = \pm\sqrt{D_{even}(\Omega)\left(D_{even}(\Omega) + 2\gamma_0 P_0\right)}. \tag{3.9}$$

Physically, $k(\Omega)$ is the propagation constant of the small monochromatic perturbation at frequency Ω. Depending on the value of k, the CW may be stable or unstable. If k has a non-

vanishing imaginary part for a certain range of Ω, perturbations will grow exponentially and then we will say the CW is unstable. We will refer to these regions of frequency as instability bands. On the contrary, if k is purely real for a certain frequency, perturbations will remain bounded and we will say that this frequency is stable. A well-known example is the case where only up to second order dispersion is taken into account, where:

$$k = \pm\sqrt{\frac{\beta_2\Omega^2}{2}\left(\frac{\beta_2\Omega^2}{2} + 2\gamma_0 P_0\right)}. \tag{3.10}$$

If $\beta_2 > 0$, k remains purely real for every value of Ω, which means that light propagating in normal dispersion regime without HOD and constant nonlinear coefficient is always stable. However, if $\beta_2 < 0$, k is purely imaginary if $\Omega^2 < \frac{4\gamma P_0}{-\beta_2}$ and $\Omega \neq 0$. In figure 3.1 (a), the imaginary part of k with parameters $\beta_2 = -2.11 \times 10^{-26}$ s^2/m, $\gamma = 5$ W^{-1}·km^{-1} and P_0 =20 kW is reported. We see that unstable regions form two lobes surrounding the pump. This kind of instability was observed using an optical fiber for the first time in Ref. [119].
Neglecting HOD is an accurate model when we are far from ZDW or the involved phenomena are not very broadband. However, when these conditions are not met, HOD must be included. The next term of dispersion which contributes to k is β_4. If this dispersion order is included, then the expression of k is:

$$k = \pm\sqrt{\left(\frac{\beta_2\Omega^2}{2} + \frac{\beta_4\Omega^4}{4!}\right)\left(\frac{\beta_2\Omega^2}{2} + \frac{\beta_4\Omega^4}{4!} + 2\gamma_0 P_0\right)}. \tag{3.11}$$

If both β_2 and β_4 are positive, k is real for any value of Ω, so a CW is always stable in this limit. Nevertheless, if $\beta_4 < 0$ there are some frequencies which may become unstable even if the pump is in normal dispersion regime. In Fig. 3.1(b) the imaginary part of k with the presence of β_4 is displayed. The employed parameters are $\beta_2 = 9.28 \times 10^{-27}$ s^2/m, $\beta_4 = -1.83 \cdot 10^{-55}$ s^4/m and the same P_0 and γ_0 used in the previous example. In this case, MI bands are much narrower and they are far detuned from the pump (126 THz). MI by fourth order dispersion has also been observed in optical fibers [41], [120], [121] ,and recently reported in optical fiber cavities [122].

An overview of both regimes can be extracted from Fig. 3.1 (c). In this figure, we plot the imaginary part of k as a function of the pump wavelength. Dispersion parameters correspond to those of pure SiO_2 and are reported on figure's caption. We see that in anomalous dispersion regime, MI is characterized by the formation of two large spectral

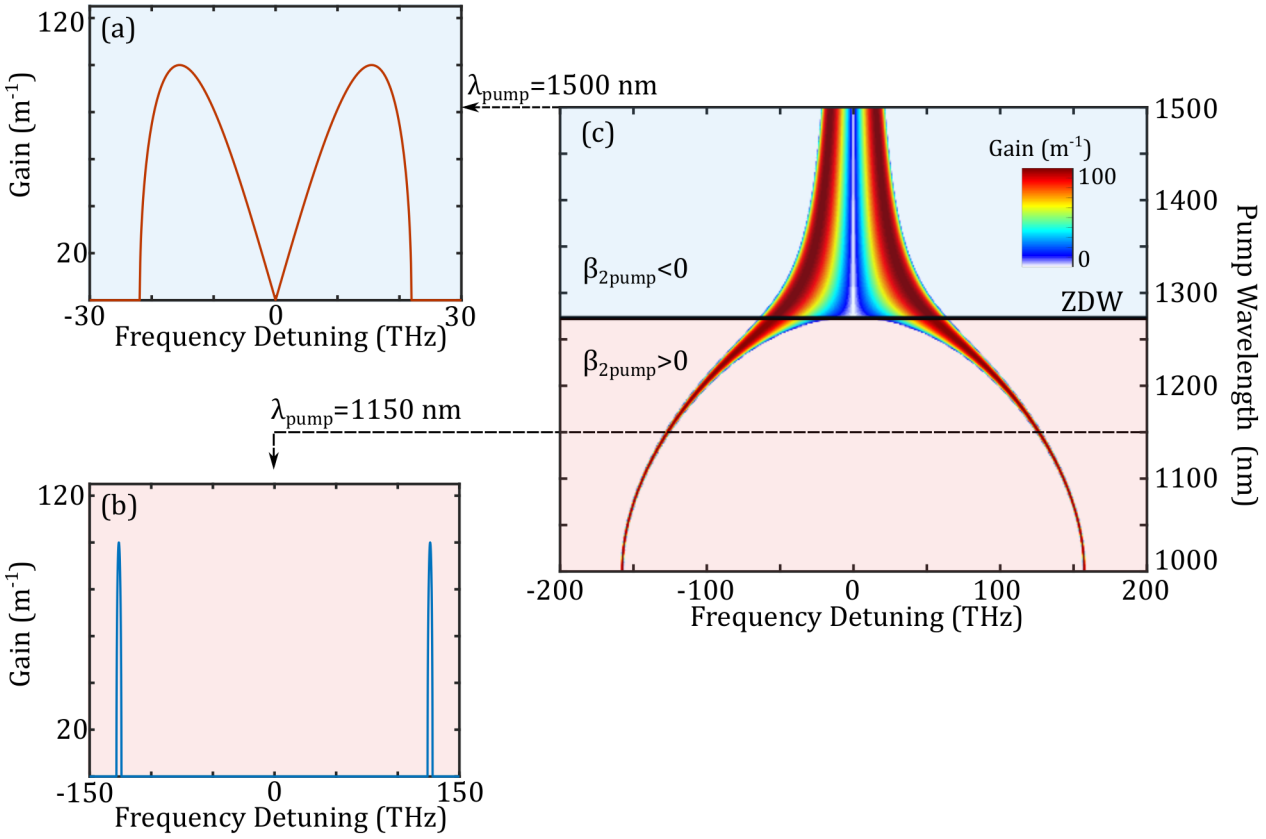

Figure 3.1: (a) Imaginary part of k for a carrier wavelength of 1500 nm. (b) Imaginary part of k for a carrier wavelength of 1150 nm. (c) Imaginary part of k as a function of the frequency detuning $\Omega/(2\pi)$ and pump wavelength. Dispersion parameters at 1300 nm are $\beta_2 = -2.37 \cdot 10^{-27}$ s^2/m, $\beta_3 = 7.91 \cdot 10^{-41}$ s^3/m and $\beta_4 = -1.83 \cdot 10^{-55}$ s^4/m. $\gamma_0 = 5$ W^{-1}·km^{-1}.

regions surrounding the pump, whereas when the pump is situated in normal dispersion regime, MI manifests as two narrow spectral bands which get further from the pump when we go deeper in normal dispersion regime.

3.3 Parametric instability

To illustrate how to analyze PR, we consider light propagation in a medium with harmonically varying nonlinearity with period Λ. This case will be relevant for the description of multimode nonlinear wave propagation [68], as shown in the third part of this manuscript. In the following we will describe the phase-matching arguments and the Floquet the-

ory which permits to calculate the central frequencies and gain profile of the generated frequency bands.

3.3.1 Phase-matching

In order to find parameter regions where perturbations a and b are unstable, we need to follow a different approach from the one employed in Sec. 3.2, since when γP_0 is a periodic function, the system coefficients (3.7) are a function of z. The first step is to reduce Eqs. (3.7) to a second order ODE, which is readily found by adding both equations and differentiating the resulting relation. By defining the function $\eta = a + b$, we obtain:

$$\ddot{\eta} + D_{even}(\Omega)\left(D_{even}(\Omega) + 2\gamma(z)P_0\right)\eta = 0. \tag{3.12}$$

$\gamma(z)P_0$ being a periodic function, the evolution of the perturbation η is ruled by the well-konwn Hill equation [123], which has been largely studied in the context of PR. In order to determine the instability regions, a simple multi-scale development can be employed [124]. As $\gamma(z)P_0$ is periodic, this function can be expressed as a Fourier series. Without loss of generality, only the m-th harmonic term is included in our calculation, then $\gamma(z) = \bar{\gamma}P_0 + \gamma_m P_0 \cos(2\pi m z/\Lambda)$, where $\bar{\gamma}P_0$ is the average value over one period and $\gamma_m P_0$ is the m-th coefficient of the Fourier series. The results can be trivially expanded for any of the remaining harmonics. Thus Eq. (3.12) is written as:

$$\ddot{\eta} + \left(k^2 + 2\epsilon\cos\left(\frac{2\pi m}{\Lambda}z\right)\right)\eta = 0, \tag{3.13}$$

where we have defined $k^2 = D_{even}(\Omega)(D_{even}(\Omega) + 2\bar{\gamma}P_0)$ and $\epsilon = 2\gamma_m P_0 D_{even}(\Omega)$. Expression (3.13) is another well-known equation in the context of PR and is called Mathieu equation. Now if we suppose a low power regime, i.e. $\epsilon \ll k^2$, a multi-scale technique can be employed. By writing $\eta = \sum_{n=0}\eta_n\epsilon^n$ and separating in different expressions each order of ϵ, an infinite hierarchy of equations is obtained:

$$\epsilon^0: \quad \ddot{\eta}_0 + k^2\eta_0 = 0, \tag{3.14}$$

$$\epsilon^1: \quad \ddot{\eta}_1 + k^2\eta_1 = -2\cos\left(\frac{2\pi m}{\Lambda}z\right)\eta_0, \tag{3.15}$$

$$\epsilon^2: \quad \ddot{\eta}_2 + k^2\eta_2 = -2\cos\left(\frac{2\pi m}{\Lambda}z\right)\eta_1, \tag{3.16}$$

$$\vdots$$

When ϵ is small enough, it is safe to keep only up to first order in ϵ^1. At order 0, η_0 is ruled by an homogeneous equation, then if k is real, η_0 is periodic and has as a general solution $\eta_0 = Ae^{ikz} + Be^{-ikz}$. On the contrary, η_1 is ruled by a non-homogeneous equation, thus even if k is real, there are parameter regions where η_1 can be unstable due to the forcing term written on the right hand side of Eq. (3.15). Conditions under which η_1 is amplified are found by introducing the general solution of η_0 in Eq. (3.15):

$$\ddot{\eta}_1 + k^2\eta_1 = -\left(Ae^{i(k+\frac{2\pi m}{\Lambda})z} + Be^{i(-k+\frac{2\pi m}{\Lambda})z}\right) + c.c. \tag{3.17}$$

Function η_1 is an unbounded solution if the natural frequency of the equation (k) is equal to the forcing frequency ($-k + 2\pi m/\Lambda$), which lead us to the parametric instability condition:

$$k^2 = D_{even}(\Omega)\left(D_{even}(\Omega) + 2\bar{\gamma}P_0\right) = \left(\frac{m\pi}{\Lambda}\right)^2. \tag{3.18}$$

It is necessary to emphasize that the obtained resonance condition takes only into account the first order in ϵ. The following orders of resonance can be obtained by solving the equation proceeding in an iterative way, i.e. we solve for the order η_1 and we introduce the solutions in the equation (3.16) and after we proceed in the same way for η_2 and so on and so forth. Physically, this result means that PR happens if the natural frequency of the system is a multiple of half the frequency of the parameter variation. The same result is found if a periodic dispersion is considered instead of a harmonic non-linearity as was shown in Ref. [58]. Some physical insight can be discovered if the limit $D_{even}(\Omega) \gg \gamma P_0$ is explored. By using a Taylor development at first order, Eq. (3.18) is approximated as:

$$2D_{even}(\Omega) + 2\bar{\gamma}P_0 = \frac{2m\pi}{\Lambda}. \tag{3.19}$$

If we take into account only up to second order dispersion, resonant frequencies are given by:

$$\Omega_m^2 = \frac{2}{\beta_2}\left(\frac{m\pi}{\Lambda} - \gamma P_0\right). \tag{3.20}$$

If the limit of a uniform fiber is considered (i.e. $\Lambda \to \infty$), we recover that MI can only happen in anomalous dispersion regime. In addition, within this limit, Ω_m^2 is the frequency with a maximum gain in the case when the dispersion regime is anomalous [40]. However, if Λ is a finite quantity, Ω_m^2 can also be positive in normal dispersion regime and thus, MI is possible. In Fig. 3.2 (a), Ω_m is plotted for different values of m and β_2. The employed parameters are $\Lambda = 0.6$ mm, $\bar{\gamma}$= 5 $W^{-1}\cdot km^{-1}$, $P_0 = 20$ kW and a dispersion corresponding

to pure silica neglecting terms over third order dispersion (at 1064 nm, β_2 =1.645 $\cdot 10^{-26}$ s^2/m and β_3 =4.428 $\cdot 10^{-41}$ s^3/m). We see how, when the pump wavelength gets closer to ZDW, generated bands get further from the pump, reaching the infinity when $\beta_2 = 0$. Each order m has an associated resonance frequency and it is symmetric with respect to the pump. For any pump wavelength, only a single pair of symmetric frequencies is generated. We can get a more general result if β_4 is included in Eq. (3.19), which bring us to the following expression for the resonant frequencies:

$$\Omega_m = \pm\sqrt{-\frac{6\beta_2}{\beta_4} \pm 2\sqrt{9\frac{\beta_2^2}{\beta_4^2} + \frac{3}{\beta_4}\left(\frac{2\pi m}{\Lambda} - 2\bar{\gamma}P_0\right)}}. \tag{3.21}$$

Including β_4 changes drastically band position in the neighborhood of ZDW, as it was shown with a dispersion oscillating fiber [125]. In figure 3.2 (b), Ω_m including β_4 = $-6.056 \cdot 10^{-56} s^4/m$ is reported. The rest of employed parameters are the same as for Fig. 3.2 (a). We can see that now, frequency detuning of instability bands does not go to infinity as the previous case. In addition to that, bands corresponding to values from m =1 to 3 produce two pairs of bands instead of one and are in normal dispersion regime. The limit of $m = 0$ is associated to the uniform case. In this case, we can see the close similarity between this band and the gain plotted in Fig. 3.1. For values of $m \leq 0$ there is only one pair of bands for each value of m and these bands are not restricted to only one dispersion region.

Equation (3.18) give us the position of the central frequency of instability bands, nevertheless it does not provide any information about the relative intensity and width of each band. To overcome this problem, we employ numerical Floquet analysis.

3.3.2 Floquet Analysis

The system Eq. (3.7) has periodic coefficients and to go deeper in the analisys of the solutions behavior, we use Floquet analysis [124], [126]. With this method, we can take advantage of the discrete symmetry of the problem, which has been exploited for the understanding of many periodic physical systems, being some relevant cases quantum mechanics [127] or photonic crystals [85]. Solutions of Eq. (3.7) can be constructed in the form:

$$\begin{bmatrix} a(z+\Lambda) \\ b(z+\Lambda) \end{bmatrix} = \mathbf{\Phi} \begin{bmatrix} a(z) \\ b(z) \end{bmatrix}, \tag{3.22}$$

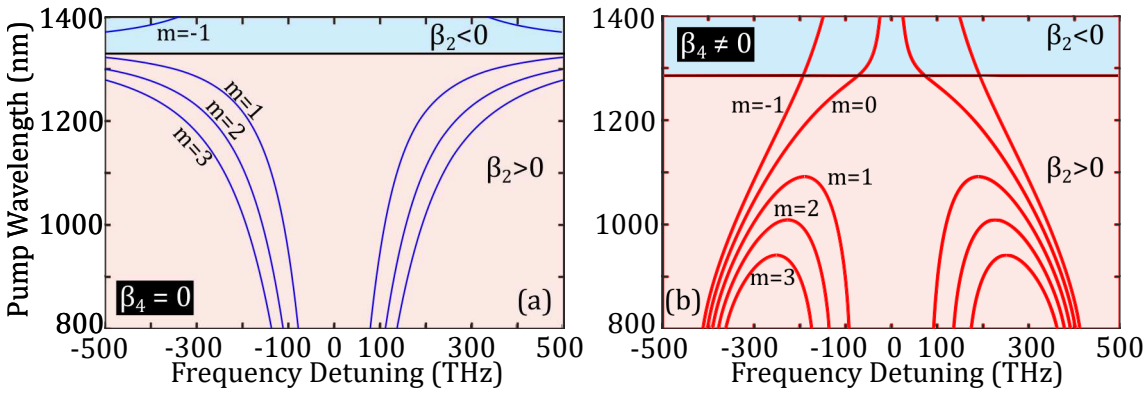

Figure 3.2: Ω_m as a function of pump wavelength neglecting β_4 (Fig. (a)) and including β_4(Fig. (b)). Dispersion at 1064 nm: β_2 =1.645 $\cdot 10^{-26}$ s^2/m, β_3 =4.428 $\cdot 10^{-41}$ s^3/m and $\beta_4 = -6.056 \cdot 10^{-56}$s^4/m. $\bar{\gamma} = 5$ W$^{-1}\cdot$km^{-1}, P$_0$ = 20 kW and $\Lambda = 0.6$ mm.

being Φ a matrix which describes discrete translations in z. The solution over n periods can be written using this matrix recursively such as $(a(n\Lambda), b(n\Lambda)) = \mathbf{\Phi}^n(a(0), b(0))$. Note that the whole solution of system (3.7) can be constructed by only solving the equations over one period. If the linear operator is written in such a basis (v_1, v_2) where its matrix representation is diagonal, the evolution over n periods is expressed as:

$$\begin{bmatrix} v_1(n\Lambda) \\ v_2(n\Lambda) \end{bmatrix} = \begin{bmatrix} \lambda_1^n & 0 \\ 0 & \lambda_2^n \end{bmatrix} \begin{bmatrix} v_1(0) \\ v_2(0) \end{bmatrix}. \tag{3.23}$$

Then in the diagonal basis, functions $(v_1, v_2)(z)$ after n periods are proportional to the initial condition. Therefore, stability of the system can be deduced from the proportionality constant, which are the eigenvalues $(\lambda_{1,2})$ of matrix Φ. Depending on the modulus of $\lambda_{1,2}$ three different cases are well identified for the asymptotic value of $v_{1,2}$:

$$v_{1,2}(n\Lambda) = \begin{cases} \infty & \text{if} \quad |\lambda_{1,2}| > 1 \\ 0 & \text{if} \quad |\lambda_{1,2}| < 1 \\ \text{periodic} & \text{if} \quad |\lambda_{1,2}| = 1 \end{cases} \tag{3.24}$$

If $|\lambda_{1,2}| > 1$, then $|v_{1,2}|$ will increases after each period, attaining infinity asymptotically, and we shall say the system is unstable. On the contrary if $|\lambda_{1,2}| < 1$, the modulus $|v_{1,2}|$ will decreases after each period, leading to 0 when $n \to \infty$. Then the system will be said to be stable. When $|\lambda_{1,2}| = 1$, then perturbations behave in a periodic manner. It is not always possible to find solutions $a(z), b(z)$ in a closed form, thus it is useful to find the

values of $\lambda_{1,2}$ numerically. Matrix Φ is found using the classical procedures to construct linear operators. This consists in solving the system over one period (z=Λ in this case) using as initial conditions two linearly independent vectors (e.g. (1,0) and (0,1)), then the two resulting solution vectors are the two columns of matrix Φ. Then the eigenvalues $\lambda_{1,2}$ can be found by calculating numerically the eigenvalues of Φ by standard procedures.

It is useful to define the gain (g), related to λ as $g = \frac{1}{\Lambda}\ln(\max(|\lambda_{1,2}|))$, thus stable solutions will have a negative gain, whilst unstable solutions will have a positive gain, which means they are amplified.

With the objective of illustrating Floquet analysis, a numerical simulation of Eq. (3.1) is carried out. A small coherent seed is included under the form of a hyperbolic secant of 1 fs duration and one tenth of the amplitude of the initial CW. We limit our study to the case were only β_2 is included in the dispersion operator and a varying nonlinearity of the form $\gamma(z) = \bar{\gamma}(1 + 0.25\cos\left(\frac{2\pi z}{\Lambda}\right) + 0.15\cos\left(\frac{4\pi z}{\Lambda}\right))$ is considered. In figure 3.3 (a), the profile of the nonlinear coefficient is displayed. In figure 3.3 (b) the output spectrum of a NLSE simulation is reported. All parameters employed in the numerical simulation are displayed in Fig. 3.3 caption. Vertical dashed lines correspond to phase-matching obtained via Eq. (3.19). The numerical simulation proves the appearance of new frequencies with a frequency detuning of $\approx$ 59 THz and $\approx$85 THz, whose origin is the harmonically varying non-linearity. We can see that the agreement between numerical simulations and phase-matching is perfect. In Fig. 3.3 (c) the corresponding numerical Floquet analysis calculated using the previously explained techniques is shown. Two bands with a gain bigger than zero arise also at $\approx$ 59 THz and $\approx$ 85 THz. Bandwidth and relative amplitude of bands corresponds well to numerical simulations reported in Fig. 3.3.

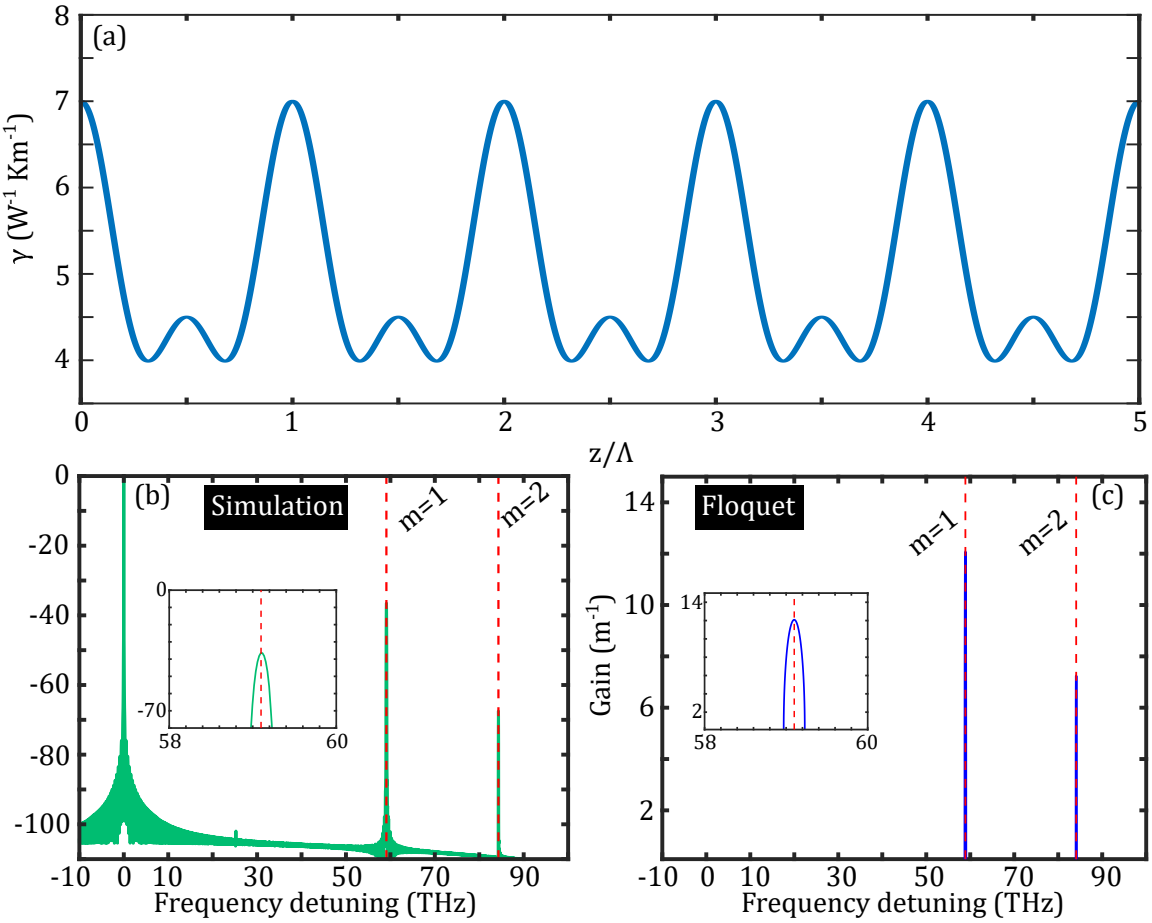

Figure 3.3: Figure (a) Evolution of the nonlinear parameter over five periods. (b) Output spectrum of a numerical simulation of NLSE using a harmonically varying γ. (c) Floquet stability analysis corresponding to propagation shown in (b). In both figures, dashed vertical lines represent frequencies predicted by phase-matching Eq. (3.19). . Parameters:$\bar{\gamma} = 5$ W^{-1} km^{-1}, $\beta_2 = 4 \times 10^{-25}$ s^{-2} m^{-1}, P_0=20 kW, L=0.7 m and $\Lambda = 1.1$ mm.

Summary

- We have presented a suitable model for describing all the MI effects presented in this manuscript, which are: classical MI produced only by the interplay between dispersion and nonlinearity and parametric instability, whose origin is the periodic variation of an external parameter.
- Classical MI in optics has been explained from a fundamental point of view. We have identified the conditions under which this phenomenon is triggered: anomalous dispersion regime and the presence of a negative fourth order dispersion.
- We have outlined how to calculate the parameters of the instability bands associated to parametric instability, both when only up to second order dispersion is taken into account and when all dispersion orders are considered.

Part II

Interaction of solitons and dispersive waves

CHAPTER

FOUR

INTERACTION OF ORTHOGONALLY POLARIZED BRIGHT SOLITONS AND DISPERSIVE WAVES

Contents

In this chapter we study the interaction between a bright fundamental soliton and a CW orthogonally polarized. As a result of this interaction, a new wave with a different frequency is generated in the same axis as the initial CW. The problem of a bright fundamental soliton interacting with dispersive waves polarized on the same axis has been a deeply studied subject. On the contrary, the configuration where the two waves do not share the same polarization has attracted considerably less attention. In the literature, only purely experimental observations [110] and some numerical results [128] have been reported. Despite these preliminary studies, a complete analysis which addresses this problem in a systematic way from a numerical, theoretical and experimental points of view was still missing. The aim of this study is to characterize the frequency of the new wave and the conditions under which this process is the most efficient. The chapter is organized as follows: in the first section 4.1, equations describing the envelopes of two orthogonally polarized fields in a birefringent media are presented. In the second section 4.2, we find the generated wave frequency using phase-matching arguments. In section 4.3, the conditions under which the new wave generation is the most efficient are found. In section 4.4, we

show the experimental results which confirm the validity of our model. Finally, in section 4.5 the stability of the soliton under fast-axis instability is analyzed.

4.1 Propagation equation

The evolution of two orthogonal nonlinear waves linearly polarized in a birefringent fiber is described by two coherently coupled nonlinear Schrödinger equations [40]:

$$\begin{aligned} i\partial_z A_x + D_x(i\partial_t)A_x + \gamma[|A_x|^2 + \frac{2}{3}|A_y|^2]A_x + \frac{\gamma}{3}A_x^* A_y^2 = 0, \\ i\partial_z A_y + D_y(i\partial_t)A_y + \gamma[|A_y|^2 + \frac{2}{3}|A_x|^2]A_y + \frac{\gamma}{3}A_y^* A_x^2 = 0. \end{aligned} \tag{4.1}$$

The dispersion operators are defined as:

$$D_x(i\partial_t) = \sum_{n\geq 2} \frac{\beta_{nx}}{n!}(i\partial_t)^n, \tag{4.2}$$

$$D_y(i\partial_t) = \Delta\beta_0 + \Delta\beta_1 i\partial_t + \sum_{n\geq 2} \frac{\beta_{ny}}{n!}(i\partial_t)^n, \tag{4.3}$$

where $\beta_n = \partial_\omega^n \beta(\omega)|_{\omega=\omega_0}$, $\Delta\beta_0 = \beta_{0y} - \beta_{0x}$ takes into account the difference of effective refractive index, $\Delta\beta_1 = \beta_{1y} - \beta_{1x}$ represents the mismatch of group velocities between axes and γ is the nonlinear coefficient. The axis with a bigger (smaller) β_0 is known as slow (fast) axis[1]. Without loss of generality, the x (y) axis is considered as the fast axis (slow axis), therefore $\Delta\beta_0 > 0$.

The involved nonlinear terms are SPM (first nonlinear term), XPM between axes (second term) and finally FWM. This last one is known as the coherent coupling term and allows the energy exchange between axes. The coefficients $2/3$ and $1/3$ appearing in Eq. (4.1) which couple the two components are given by the nature of the polarizability of silica and the polarization of the field.

This equation has been traditionally studied under two limiting cases, which are classified as a function of the relation between beat length, defined as $L_B = 2\pi/|\Delta\beta_0|$, and fiber length ($L_{fiber}$):

- High-birefringence (HiBi): in this case, the beat length is much shorter than the

[1]This notation is coherent with the literature describing birefringent media, where the axis with a lower (higher) refractive index is called fast (slow) axis.

fiber length ($L_{fiber} \gg L_B$). The coherent coupling term can be neglected because its contribution can be averaged to zero and, as a consequence, there is not an efficient exchange of energy between axes.

- Low-birefringence (LoBi): beat and fiber length are of the same order of magnitude ($L_{fiber} \approx L_B$), thus the coherent coupling term cannot be neglected, hence the energy exchange between axes is allowed. In this case, a wave propagating over the fast -axis can be unstable [129] due to that energy exchange. In the literature is common to neglect in this case the group velocity mismatch ($\Delta\beta_1 = 0$).

In the situation considered here, the birefringence is considered high enough to avoid fast axis instability as it will be shown at the end of the chapter. However we cannot neglect the coherent term because it is at the origin of the interaction under investigation, as it will be shown in the next sections.

4.2 Phase-matching

In this section we find the frequency of the generated wave by using phase-matching arguments. The procedure is standard and we followed a similar approach as reference [130], but adapting it for the special case of a soliton and a CW orthogonally polarized. We consider a soliton with frequency ω_0 polarized along the x-axis whose expression is $A_x = \sqrt{P_0}\mathrm{sech}(T/t_0)e^{iqz} = F(t)\mathrm{e}^{iqz}$, where $q = \gamma P_0/2$ and a CW polarized along the y-axis with frequency ω_p ($A_y = g(z,T)$). The frequencies of the waves are far enough from ZDW therefore dispersion orders higher than two are neglected, and the influence of Raman effect is considered to be negligible. If $g(z,T)$ is weak ($|g(z,T)| \ll |F(t)|$), we can linearize Eq. (4.1) as follows:

$$i\partial_z A_x - \frac{\beta_{2x}}{2}\partial_T^2 A_x + \gamma|A_x|^2 A_x = 0, \tag{4.4}$$

$$i\partial_z g - \frac{\beta_{2y}}{2}\partial_T^2 g + \frac{\gamma}{3}\left(2|F|^2 g + F^2 g^* e^{i2qz}\right) = 0. \tag{4.5}$$

Equation (4.4) is the NLSE introduced in chapter 2. The evolution of A_x is thus not influenced by $g(z,T)$ at first order, and it can be assumed to behave as an unperturbed fundamental soliton. Equation (4.5) gives the evolution of a linear wave (g) under the influence of the soliton. The field g can be written as the sum of a CW pump (second term)

and a generated wave (first term):

$$g(z,t) = \psi_g(z,T)e^{i(k_p z - \Omega_p t)} + \psi_p(z,T)e^{i(k_g z - \Omega_g t)}, \tag{4.6}$$

where $\Omega_{p,g} = \omega_{p,g} - \omega_0$, being ω_0 the frequency of the soliton and $\omega_{p,g}$ the frequency of pump (p) and generated wave (g). Here, we consider that the pump propagates linearly and without losing energy (its amplitude is constant), so its dispersion relation reads as $k_p = D_y(\Omega_p)$. By introducing Eq. (4.6) in Eq. (4.5) we obtain:

$$\begin{aligned} i\partial_z\psi_g + (D_y(i\partial_t) - k_g)\psi_g + \frac{\gamma}{3}\left(2|F|^2\psi_g + F^2\psi_g^* e^{i2qz}\right) = \\ - \frac{\gamma}{3}\left(2|F|^2\psi_p e^{i((k_p-k_g)z-(\Omega_p-\Omega_g)t)} + F^2\psi_p^* e^{i((2q-(k_p+k_g))z+(\Omega_p+\Omega_g)t)}\right). \end{aligned} \tag{4.7}$$

The right hand side terms of Eq. (4.7) acts as sources which can efficiently transfer energy to $\psi_g(z,T)$ if the z-dependence of the exponents vanishes, translating in the following phase-matching expressions [130] :

$$D_y(\Omega_g) = D_y(\Omega_p), \tag{4.8}$$

$$D_y(\Omega_g) = 2q - D_y(\Omega_p). \tag{4.9}$$

These conditions are the same that were introduced in Sec 2.4.2. The first resonance does not depend of the soliton parameters and it is known as phase-insensitive, while in the second one the soliton wave-number is explicitly present and it is called phase-sensitive. Note that the phase sensitive resonance appears because the coherent term of Eq. (4.1) was kept. If the coherent term were disregarded following the traditional limit employed for HiBi fibers, phase-sensitive resonances would not be accounted for in the model.

To illustrate the validity of this analysis, a numerical example is performed. We consider a soliton of peak power 188 W, time duration $t_0 = 210$ fs and central wavelength $\lambda_0 = 1430$ nm propagating in a 2 meters long PCF, whose parameters at 1430 nm are $\Delta\beta_0 = 295$ m^{-1}, $\Delta\beta_1 = -0.4$ ps $\cdot$ m^{-1}, $\beta_{2x} \approx \beta_{2y} = \beta_2 = -4.5 \cdot 10^{-26}$ s^{2}m^{-1} and $\gamma = 5$ W^{-1}km^{-1}. The CW has an average power of 0.1 W and a carrier wavelength of λ_p =1570 nm. In Fig. 4.1 (a), Eq. (4.9) is graphically solved. The red (blue) line represents the dispersion of linear waves on the y-axis (x-axis). Black line represents the right hand side of Eq. (4.9) for λ_p. The generated wave is found to be at $\lambda_g = 1318$ nm (at the intersection of the red line and

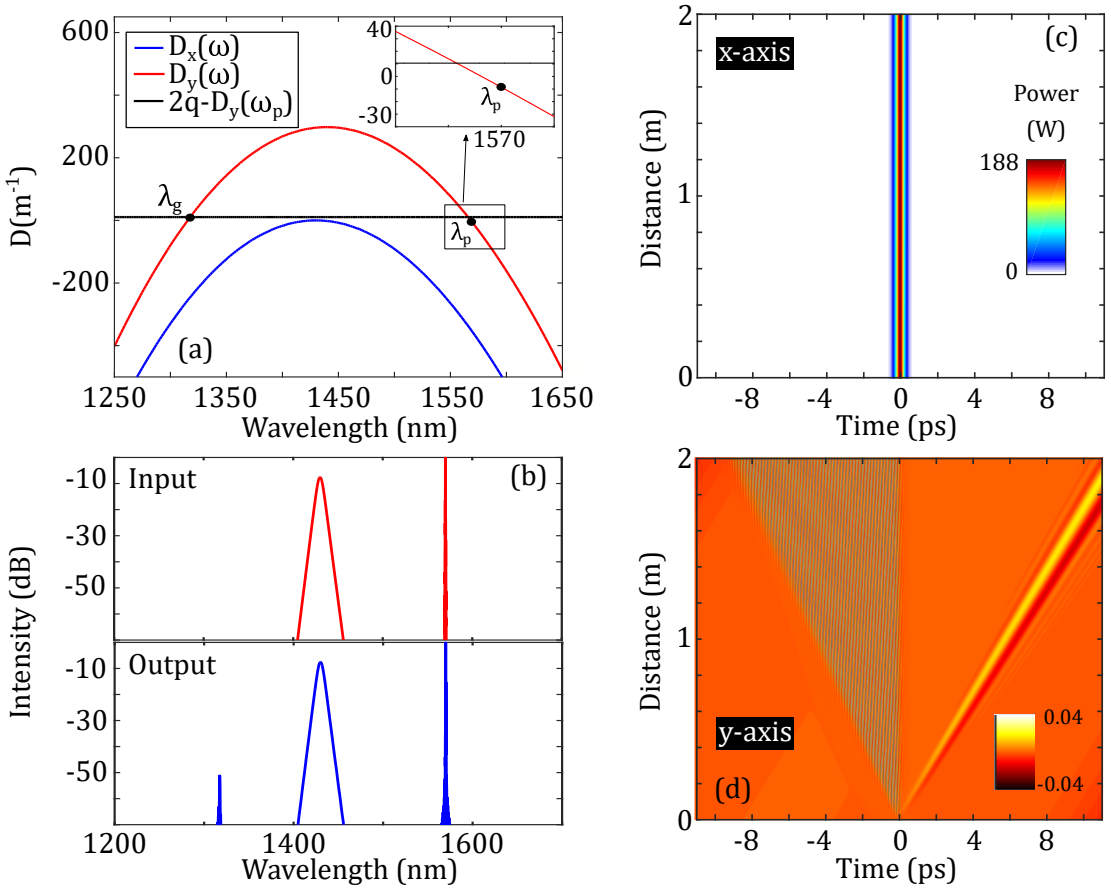

Figure 4.1: Interaction between a soliton and a CW. (a) Graphical solution of Eq. (4.9). (b) Input (top) output (bottom) spectrum after propagation.(c) Time domain evolution in the x-axis (fast axis). (d) Time domain evolution in the y-axis (slow axis), the represented quantity is $|A_y|^2/P_p - 1$.

the black one). In order to confirm these predictions, we report in Fig. 4.1 (b), the results of numerical solution of Eqs. (4.1), where the input (top) and output (bottom) spectrum are shown. It is remarkable that the soliton is not altered, as it is confirmed by looking at the temporal domain evolution shown in Fig. 4.1 (c), where the temporal evolution on the x-axis is reported. Figure 4.1(d) shows the temporal evolution along the y-axis. Over the CW background, it can be clearly seen the generated wave propagating faster than the carrier frequency. In addition, we can identify a localized wave emitted which travels slower than the carrier frequency reference frame and hence travels towards positive time delays. This wave rapidly detaches from the soliton and does not play any significant role.

4.3 Amplitude of generated wave

Phase-matching arguments just predict the generated frequency, but does not guarantee the efficient generation of the new wave. We thus have developed a deeper analysis of perturbation equations in order to fully understand the process [131]. The final result of this section is an analytical expression of the conversion efficiency. To obtain the expression of the efficiency, we followed the same method described in [130], but adapting the theory to a CW and a soliton orthogonally polarized. The starting point is Eq. (4.5), where we introduce the *ansatz* described in Eq. (4.6) and we suppose that phase-matching is verified. The fields ψ_p and ψ_g are considered to be spectrally narrow, thus temporal partial derivatives with higher order than two are neglected [130]:

$$i\partial_z\psi_{g,p} + iD'_g\partial_t\psi_{g,p} + \frac{\gamma}{3}\left(2|F|^2\psi_{g,p} + F^2\psi^*_{p,g}e^{i\Delta\omega t}\right) = 0, \tag{4.10}$$

where $\Delta\omega = \Omega_p + \Omega_g$. Equations (4.10) seem quite intricate, but they can be solved by an iterative process. The general solution of these equations is:

$$\psi_{g,p} = \left[C(T - D'_{g,p}z) + \frac{i\gamma}{3}\int_0^z F^2(T)\psi^*_{p,g}(T,z)e^{i(\Delta\omega T - S_{p,g}(T))}\right]e^{iS_{g,p}(T)}, \tag{4.11}$$

$$S_x = \frac{2\gamma P_0 t_0}{3D'_x}\tanh\left(\frac{T}{t_0}\right), \tag{4.12}$$

where C is a constant fixed by the boundary conditions. To solve this equation we consider that the pump is not depleted and thus it can be written as a constant such as $\psi_p = \sqrt{P_p}$. To obtain the solution for ψ_g, we introduce the solution of ψ_p in Eqs. (4.10) and we consider that the velocity mismatch between soliton, pump and generated wave is large enough

in order to consider $S_{g,p}(T) \approx 0$. This means that we neglect the phase induced by XPM between the soliton over the pump and generated wave. This approximation could not be done when pump or generated wave and the soliton have the same group velocity, as it was shown in [130]. By taking into account the initial conditions $\psi_g(z=0,T)=0$, we get:

$$\psi_g(\tau) = \frac{i\gamma\sqrt{P_p}}{3|D'_g|}\int_{T/t_0}^{(T+D'_g z)/t_0} dx F^2(x) e^{i\Delta\omega t_0 x} \approx \frac{i\gamma\sqrt{P_p}P_0}{3|D'_g|}\int_{-\infty}^{\infty} dx\, \mathrm{sech}^2(x) e^{i\Delta t_0 \omega x}, \quad (4.13)$$

where we have performed an asymptotic approximation, i.e. we look far enough from the soliton. The last integral can be solved in closed form:

$$|\psi_g| = \frac{\pi\gamma\Delta\omega P_{sol}\sqrt{P_p}t_0^2}{3|D'_g|}\sinh^{-1}\left(\frac{\Delta\omega t_0 \pi}{2}\right). \quad (4.14)$$

The obtained amplitude of the generated wave diverges for $|D'_g| \to 0$, but as we have previously assumed, this situation is not considered in our model. It is worth to note that the amplitude presented in Eq. (4.14) does not depend on T. To verify this result, the temporal domain of the simulation performed on last section is revisited. In figure 4.2 (a) the simulated temporal profile of $|\psi_g|^2$ is shown in solid blue line. To obtain this result, we take advantage of the fact that ψ_g and ψ_p are well resolved spectrally, then ψ_p can be filtered out from the output spectrum of the y-axis. The wave is almost squared-shaped, corroborating the obtained result by means of our analytic approach.

Taking advantage of the temporal shape of the generated wave, the energy can be approximated as $E_g = |\psi_g|^2 T_g$, where the time duration is given by $T_g = L_{fiber} D'_g$. In Fig. 4.2 (a) we can see the approximated temporal shape, which is represented by a red dashed line. Then, the energy of the generated wave is given by the following equation:

$$E_g = P_p\left(\frac{|\beta_2|\Delta\omega\pi}{3}\right)^2 \sinh^{-2}\left(\frac{\Delta\omega t_0\pi}{2}\right)\frac{L_{fiber}}{D'_g}, \quad (4.15)$$

where we have exploited the relation between power and duration of a fundamental soliton $P_0 = |\beta_2|\gamma^{-1}t_0^{-2}$. The energy of the generated wave is maximal when $\Delta\omega = 0$, which corresponds to the conservation of energy for a degenerated FWM between soliton, generated wave and pump. This fact is complemented by phase matching, so that the maximal of energy is attained when both energy and phase-matching are preserved.

This result can be verified by numerically integrating Eqs. (4.1). In Fig. 4.2 (b), a

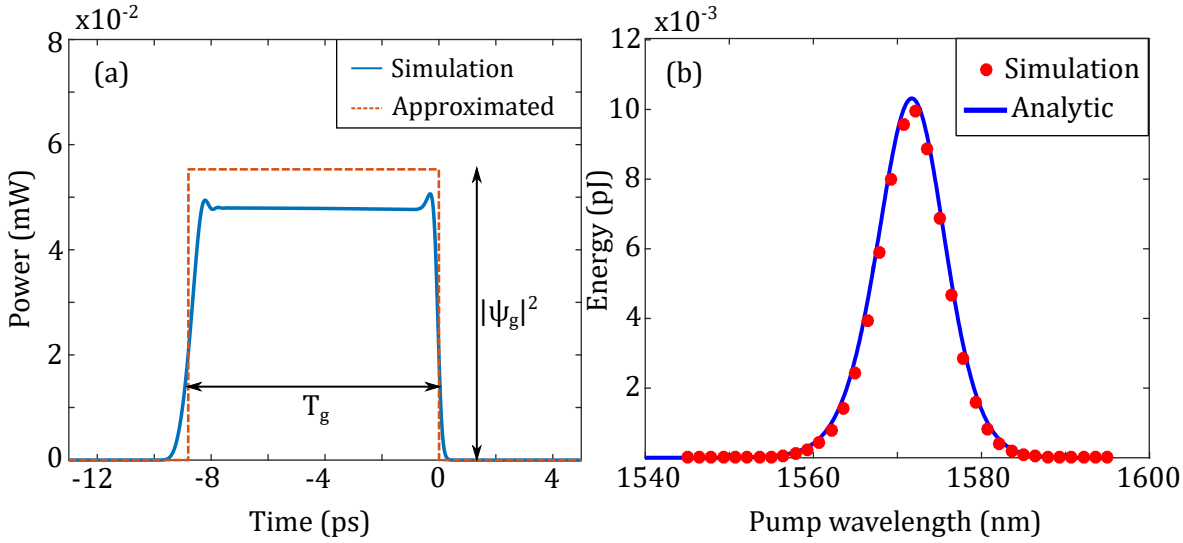

Figure 4.2: (a) Temporal profile of the generated wave at 1318 nm. (b) Energy of the generated wave, solid line stands for the analytic results while dots are obtained by numerical integration of Eq. (4.1).

comparison between the expression (4.15) and simulations is displayed. In the horizontal axis, we represent the corresponding pump wavelength and in the vertical axis, the generated wave energy. Blue line shows the predicted energy and red dots the corresponding result from numerical simulations. Both approaches have a good agreement, validating the employed theoretical derivation.

If phase-matching and the condition $\Delta\omega$ are merged, the frequency at which the generation is maximal is obtained:

$$\omega_g^2 = \frac{2(q - \Delta\beta_0)}{\beta_2}. \tag{4.16}$$

In the case of highly birefringent fibers, $\Delta\beta_0 \gg q$, and as the anomalous dispersion regime is considered ($\beta_2 < 0$), only solitons polarized along the fast axis can fulfill both energy and momentum conservation.

4.4 Experimental results

To confirm the validity of the model obtained in the previous sections, a series of experiments were carried out in the IRCICA by Florent Bessin, following the parameters from

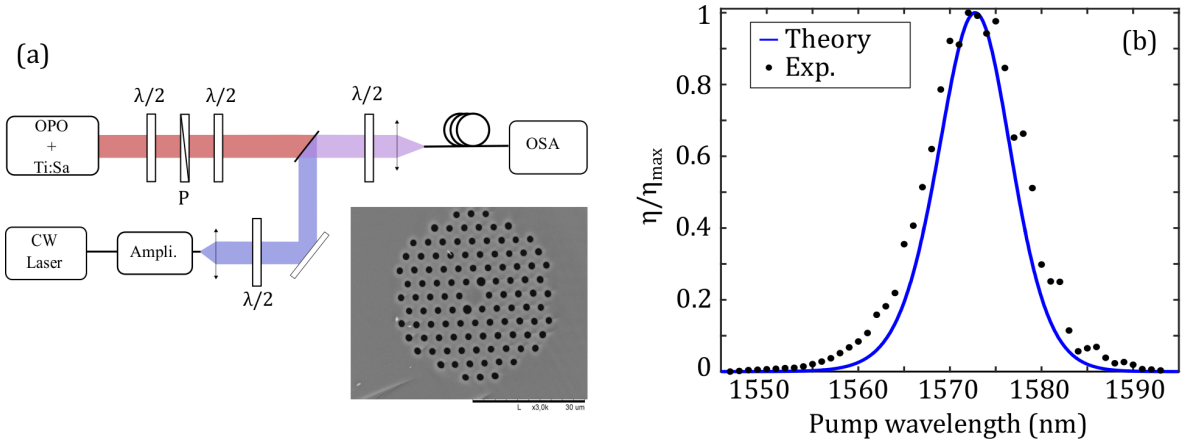

Figure 4.3: (a) Experimental setup used in experiments. OPO, optical parametric oscillator; BS, beam splitter; P, polarizer; $\lambda/2$, half-wave plate; Ampli, amplifier; OSA, optical spectrum analyzer. (b) Comparison between theoretical and experimentally measured (black dots) conversion efficiency. Soliton duration t_0= 133 fs.

my initial numerical and theoretical studies.

Figure 4.3 (a) shows a scheme of the experimental setup. Solitons were excited using Gaussian pulses of 250 fs at full width half maximum at the wavelength of 1430 nm, delivered by an optical parametric oscillator pumped with a Ti:Sa laser. In order to control the power to excite a fundamental soliton, a variable attenuation composed by a half-wave plate and a polarizator is placed just after the OPO. To control the polarization of the attenuator output, an additional half-wave plate is placed just after. This polarization is important because the transmission coefficient of the beam spliter (BS) depends on it. The CW is generated by a laser diode tunable in the range 1540-1600 nm and amplified using an erbium doped fiber amplifier. A $\lambda/2$ plate is placed just after to control the polarization of the radiation and put it orthogonally polarized to the soliton. After, the two beams are combined with a BS. Before injecting in the fiber, a $\lambda/2$ is placed, in this way, the polarization of the beams can be oriented along the correct neutral axis of the fiber.

The employed fiber is a 3 m long PCF fabricated at the IRCICA with parameters γ =5 W^{-1} km^{-1} and $\beta_2 = -4.5 \times 10^{-26}$ s^2/m at 1430 nm. This PCF was designed to be polarization mantaining, then the difference of effective index between axes is large $\Delta\beta_0 = 294$ m^{-1}. This special design can be noted on the fiber transverse plane (see the small inset showing the fiber in Fig. 4.3). The peculiarity lies in two bigger PCF holes, which increase the difference between effective refractive index of the two axes.

Generated wave energy can be directly measured experimentally by integrating the

corresponding portion of the spectrum. However, only a small fraction of the pump effectively interacts with the soliton over a finite fiber length. The portion of energy which efficiently interacts with the soliton is given by $E_p^{(int)} = P_p T_p$, where T_p is the time duration of the pump wave portion which interacts with the soliton. T_p can be expressed as a function of known paramaters as $T_p = |D'_g| L_{fiber}$. To take this into account, we introduce a conversion efficiency η as follows [132]:

$$\eta = \frac{E_g}{E_p^{(int)}} = \frac{|\psi_g|^2 T_g}{P_p T_p} = \left[\frac{\beta_2 \Delta\omega\pi}{3D'_g}\right]^2 \sinh^{-2}\left(\frac{\Delta\omega\pi t_0}{2}\right)\frac{D'_g}{D'_p}, \tag{4.17}$$

Figure 4.3 .(b) shows the comparative between the efficiency obtained by using the model (blue solid line) assuming a soliton of $t_0 = 133$ fs and the result obtained experimentally (black dots). Results are normalized to its maximum because we could not measure experimentally the absolute value of the energy. We can see that there is a good agreement between the model that we have developed and the experimental results. This outcome gives for the first time a global understanding between theory and experiments of the interaction between a CW and a soliton orthogonally polarized.

4.5 Soliton stability

In a linear birefringent medium, light propagating along one of the neutral axes keeps its polarization state. However, when the intensity is increased, the refractive index is susceptible to change as a result of the Kerr effect. In the case of a silica fiber, when light is polarized along the fast axis, the nonlinearity decreases the birefringence until the point where the fiber may become isotropic. If the intensity is still augmented, birefringence of the fiber is inverted and this fact leads to an unstable behaviour of light [133]. This phenomenon has been experimentally observed and numerically studied with solitons propagating in a birefringent PCF [134].

As it was previously shown, in order to observe the FWM process between soliton and CW, the soliton must be polarized along the fast axis, which may undergo to polarization instability if the power is big enough. To verify that we are far from the instability threshold, we carry out a stability analysis of the soliton using the classical procedures depicted in [129], [135]–[137] .

As a first step, Eq. (4.1) is written in normalized soliton units [40]:

$$[i\partial_z - \hat{q} - \frac{\text{sign}(\beta_2)}{2}\partial_T^2]u_x + [|u_x|^2 + \frac{2}{3}|u_y|^2]u_x + \frac{1}{3}u_y^2 u_x^* = 0,$$
$$[i\partial_z + ((\alpha_0 - \hat{q}) + i\alpha_1\partial_T - \frac{\text{sign}(\beta_2)}{2}\partial_T^2)]u_y + [|u_y|^2 + \frac{2}{3}|u_x|^2]u_y + \frac{1}{3}u_x^2 u_y^* = 0 \quad (4.18)$$

Where the new normalized variables are defined as:

$$z = \frac{z|\beta_2|}{\tau^2}\ ,\ \alpha_0 = \frac{\Delta\beta_0\tau^2}{|\beta_2|}\ ,\ \alpha_1 = \frac{\Delta\beta_1\tau}{|\beta_2|}\ ,\ \hat{q} = \frac{\gamma P_0}{2}\frac{\tau^2}{|\beta_2|}\ ,\ A_k = \sqrt{\gamma L_D}u_k e^{i\hat{q}z}\ ,\ T = \frac{t}{\tau}, \quad (4.19)$$

where τ is an arbitrary time and $L_D = \tau^2/|\beta_2|$. We write the envelopes as a stationary solution u_{0k} (where k stands for the polarization axis) perturbed by the functions $\delta(z,T)$ and $\epsilon(z,T)$ which verify $|\epsilon,\delta| \ll |u_{0k}|$:

$$u_x = u_{0x} + \epsilon\ ,\ u_y = u_{0y} + \delta. \quad (4.20)$$

By introducing these equations in Eq. (4.18), the following equation for the x-axis is found:

$$\begin{aligned}[i\partial_z - \hat{q} - \frac{\text{sign}(\beta_2)}{2}\partial_T^2](u_{0x}+\epsilon) + [(|u_{0x}|^2u_{0x} + 2|u_{0x}|^2\epsilon + u_{0x}^2\epsilon^*) + \quad (4.21)\\ + \frac{2}{3}(|u_{y0}|^2u_{x0} + u_{x0}u_{y0}\delta^* + u_{x0}u_{y0}^*\delta + |u_{y0}|^2\epsilon)] +\\ + \frac{1}{3}[u_{0y}^2u_{0x}^* + u_{0y}^2\epsilon^* + 2\delta u_{0y}u_{0x}^*] = 0.\end{aligned}$$

The corresponding equation for the y-axis can be readily obtained by just switching $\epsilon \to \delta$, x$\to$y. Now, let us assume a soliton propagating with x-polarization to be a stationary solution of Eq. (4.18). Then the functions u_{0k} can be written such as:

$$u_{0x} = \sqrt{2\hat{q}}\text{sech}(\sqrt{2\hat{q}}t)\ ,\ u_{0y} = 0. \quad (4.22)$$

These assumptions bring us to obtain the following equations for the perturbation:

$$[i\partial_z - \hat{q} - \frac{\text{sign}(\beta_2)}{2}\partial_T^2]\epsilon + 2|u_{0x}|^2\epsilon + u_{0x}^2\epsilon^* = 0$$
$$[i\partial_z + ((\alpha_0 - \hat{q}) + i\alpha_1\partial_T - \frac{sign(\beta_2)}{2}\partial_T^2)]\delta + \frac{2}{3}|u_{0x}|^2\delta + \frac{1}{3}u_{0x}^2\delta^* = 0. \quad (4.23)$$

Perturbations on the x-axis are ruled by the same equations as perturbations of a soliton in scalar NLSE, whose behavior is stable when HOD is absent. However, the possibility of an unstable evolution on the y-axis cannot be ruled out *a priori* . To analyze the exponential growth of δ, it is advantageous to write this function as:

$$\delta = a(T)e^{\kappa z} + b(T)^* e^{\kappa^* z} \tag{4.24}$$

By substituting in Eq. (4.23) we get the following eigenvalue problem:

$$\begin{bmatrix} \tilde{D}(i\partial_T) - \hat{q} + \frac{2}{3}|u_{0x}|^2 & \frac{1}{3}u_{0x}^2 \\ -\frac{1}{3}u_{0x}^2 & -(\tilde{D}(-i\partial_T) + \frac{2}{3}|u_{0x}|^2 - \hat{q}) \end{bmatrix} \begin{bmatrix} a \\ b \end{bmatrix} = \kappa \begin{bmatrix} a \\ b \end{bmatrix}, \tag{4.25}$$

where $\tilde{D}(i\partial_T) = \alpha_0 + i\alpha_1\partial_T - sign(\beta_2)/\partial_T^2$ is the normalized dispersion operator. This system will be unstable if some eigenvalues verify $Re(\kappa) > 0$, which means that perturbations will be amplified. The problem presented in Eq. (4.25) cannot be solved analytically, thus we implemented a numerical method to find eigenvalues approximately. To transform this differential operator into an algebraic one, a finite difference scheme is used [72], and the eigenvalues κ are calculated following a standard procedure. In figure 4.4, the real part of the eigenvalues with bigger modulus is shown. Under a certain critical power, they remain complex, but once a threshold is crossed, the eigenvalues become purely real which means the soliton is unstable. Physically this means the perturbations in the slow axis have an exponential growth because the soliton transfer energy to this axis. The choice of τ is arbitrary, so without any lose of generality, we chose it to make $\alpha_0 = 1$.

From Figure 4.4, we see that this critical power can be found near 1500 kW, and the performed experiments employ a soliton of a peak power of 180 W, thus we are well below the power regime where the soliton is not stable.

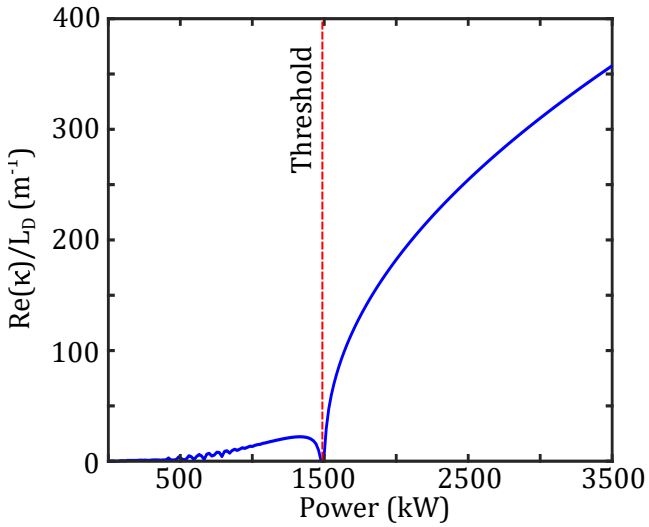

Figure 4.4: Stability analysis of the soliton using the same fiber parameters as the experiments depicted in Sec. 4.4. Parameters : $\alpha_0 = 1$, $\alpha_1 = -0.116$ and $\tau = 12.3$ fs.

Summary

We have analyzed the interaction of soliton and CW orthogonally polarized in a birefringent fiber. The presented results can be summarized as:

- We presented the equations that describe light propagation in a birefringent fiber, the coherently coupled nonlinear Schrödinger equation.
- The phase-matching conditions which allowed us to calculate the frequency of the generated wave have been described.
- An analytic model has been derived to predict under which conditions the interaction between solitons and CW is the most efficient. Predictions of this model have been verified by experimental results.
- We have numerically checked that, under our experimental conditions, the soliton is stable.

CHAPTER

FIVE

INTERACTIONS BETWEEN DARK SOLITONS AND DISPERSIVE WAVES

Contents

Like bright solitons, dark solitons can also emit Cherenkov radiation and interact with dispersive waves in the neighborhood of ZDW. Surprisingly, a global understanding of these problems with dark solitons was still missing in the vast literature of solitons in optical fibers. In the case of Cherenkov radiation, some studies were carried out in the 90s [102], [103] and 2000s [104]. However, these studies were restricted only to theoretical results and there were not any experimental evidence of this process. In this manuscript, with the objective to understand the experimental results obtained in our laboratory, all the calculations are shown in a systematic fashion and looked through a different prism. In this chapter we will show how to predict the frequency of emission and its efficiency, which will be calculated by adapting the theory for bright soliton [101] to the particularities of dark solitons.

The case of the interaction of dark solitons with weak waves was also still missing of a global understanding. This problem was partially adressed in [117] but only the phase

matching relation using a black soliton was found. In this chapter, we will calculate a general phase-matching relation which takes into account for an arbitrary grayness. In addition to predict the frequency of the new wave, we will calculate the efficiency of the process.

In both cases, Cherenkov emission and interaction between dark solitons with weak waves, the analytic calculations are compared by numerical solution of NLSE and experimental results.

The chapter is organized as follows: In the first section 5.1, the experimental setup is briefly described, with a particular emphasis on how dark solitons are generated. In the second section, the process of Cherenkov emission is analyzed, by predicting the frequency in Sec. 5.2.1 and the efficiency in Sec. 5.2.2 of the generated wave. After, in Sec. 5.2.2, the calculation of the process efficiency is reported. In the third section 5.3, the interactions between dark soliton-dispersive waves are tackled. Following the same logic, we will derive in 5.3.1 the phase-matching condition, which allows to predict the new wave frequency and finally, the process efficiency will be analyzed in section 5.3.2.

5.1 Experimental Setup

The experiments reported here were carried out at our laboratory by Tomy Marest, who designed a setup with the objective to generate single dark solitons in the femtosecond regime with a controllable grayness. The generation of single dark solitons presents some big challenges, but the most cumbersome is to give the pulse the correct odd-symmetric phase. If the phase does not verify this condition, then the dark pulse will split in two different gray solitons propagating with different group velocities [138]. There have been reported several methods to generate dark solitons in the litterature. Some relevant examples are experimental setups where a phase-mask is employed to taylor the pulse spectrum and generate dark pulses [139], [140], the interference between two chirped pulses [141] or the use of an intensity modulator [142]. In our case, we employed programmable spectral filters (named waveshapers) capable of controlling amplitude and phase. These filters are programmed to transform a pulse delivered by a laser to a supergaussian pulse with an intensity dip at the center and the correct phase. This dark pulse can approximate a dark soliton if the background is wide enough [143]. The employed method for generating dark solitons allows to control the grayness, then its effect over the generated frequency can be studied, in contrast to preceeding works where a train of solitons with uncontrolled grayness [105] was employed to study Cherenkov radiation.

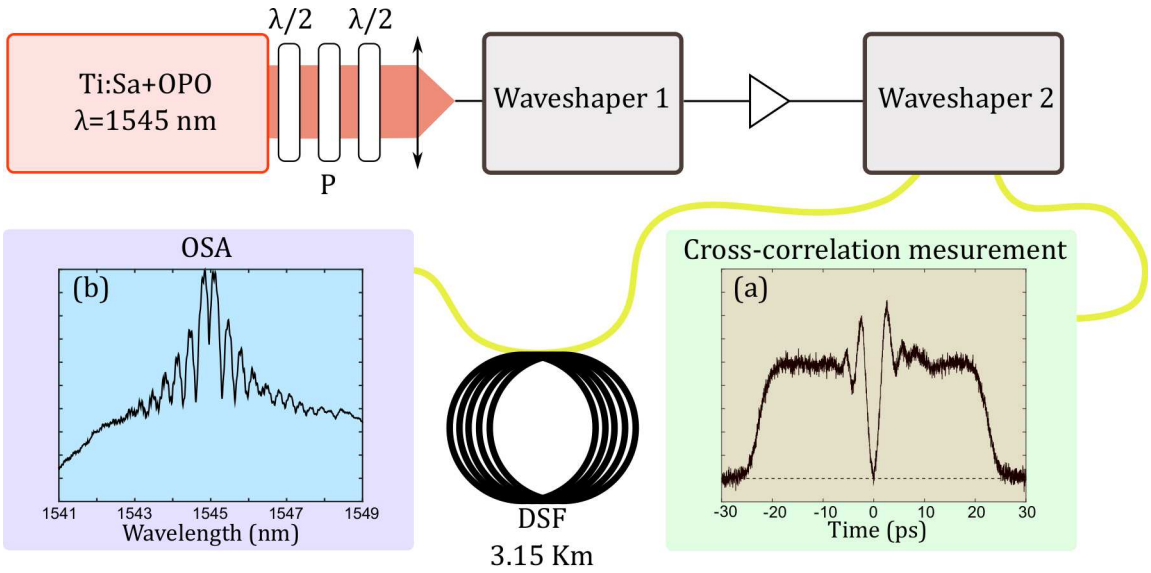

Figure 5.1: Experimental Setup. DSF parameters: ZDW 1549.5 nm, $\beta_3 = 1.15 \cdot 10^{-40}$ s^3/m at ZDW, $\gamma = 0.002$, $W^{-1}m^{-1}$

The experimental setup is displayed in Figure 5.1. Gaussian shaped pulses are delivered by an optical parametric oscillator (OPO) pumped by a Ti:Sa laser. They have a duration of 220 fs at FWHM and are almost Fourier transform limited. Their power and polarization are controlled by a variable attenuator and a half-wave plate. After, pulses go through a combination of waveshapers and amplifiers. The first waveshaper sets the correct intensity profile, then pulses are amplified and finally they get to a last waveshaper, which corrects the defects produced by the amplification and draws the odd-symmetric phase. Finally the dark pulse is injected in a dispersion shifted fiber (DSF), where the process under investigation will take place.

To confirm the temporal shape of the generated dark solitons, a cross-correlation measurement was developed. In the inset (a) of Fig. 5.1, the obtained temporal input is shown, whose shape corresponds well to the one expected from the configuration of waveshapers. In the inset (b) of Fig. 5.1, the spectrum of a dark pulse is shown. The observed oscillations correspond to the Fourier transform of the product of a finite background and a phase jump.

5.2 Emission of Cherenkov radiation by a dark soliton

5.2.1 Phase-matching

In order to find the phase-matching relation of Cherenkov radiation emitted by dark solitons, we adopted a method similar to the one followed with bright solitons [101]. However, in this case the procedure is more delicate due to two main reasons. On the one hand, the generated wave will propagate over a CW background, hence the dispersion relation is modified. To find this dispersion relation it is necessary to perform an asymptotic analysis, i.e to look at $|T| \gg 0$, where the soliton can be approximated as a CW background. On the other hand, the soliton does not necessarily travel at the same group velocity as the CW background, which requires also special attention.

Our starting point is Eq. (2.2) with HOD up to third order. We did not take into account Raman effect because it does not play a significant role, thus it can be safely neglected. The envelope is supposed to be a superposition of a dark soliton given by Eq. (2.8) and a small perturbation g:

$$A = (F + g)e^{i\gamma P_0}. \tag{5.1}$$

This way of writing the field is coherent with the results obtained from direct numerical simulations of NLSE. For example figure 5.2 (a) reports the evolution of a dark soliton with grayness ($\phi = 0$, i. e. black soliton) in the presence of HOD. From this simulation, we see the dark pulse propagating almost without deformation and some emitted radiation traveling to positive delay, whose origin is the Cherenkov emission. There is also the emission of a small gray soliton traveling toward negative delays. This small soliton quickly separates from the main dark soliton and we can consider that it does not play any significant role [103]. When *ansatz* written in Eq. (5.1) is substituted in NLSE, the following equation ruling the perturbation is found:

$$i\partial_z g + D(i\partial_T)g + \gamma(2|F|^2 g + F^2 g^*) - \gamma P_0 g = -\left(D(i\partial_T) + \frac{\beta_2}{2}\partial_T^2\right)F. \tag{5.2}$$

This equation is quite similar to the one obtained in [101], but now the soliton has a group velocity β_{1sol} fixed by its grayness. This problem is overcome by changing the reference frame $\tau = T - \beta_{1sol} z$. With this simple change, one of the main problems proposed at the beginning of this section has been solved. Now we write the perturbation as:

$$g(z,\tau) = C_1(z)e^{i(kz-\Omega\tau)} + C_2(z)e^{-i(kz-\Omega\tau)}, \tag{5.3}$$

where Ω is the frequency detuning of the generated wave from the soliton. It is easy to find the equation ruling C_1 and C_2:

$$i\begin{bmatrix}\dot{C}_1\\ \dot{C}_2\end{bmatrix}+\mathbf{M}\begin{bmatrix}C_1\\ C_2\end{bmatrix}=\begin{bmatrix}S\\ -S^*\end{bmatrix}, \tag{5.4}$$

where $\mathbf{M}$ is the following matrix:

$$\mathbf{M}=\begin{bmatrix}D(\Omega)-\beta_{1sol}\Omega-\gamma P_0-k+2\gamma|F|^2 & \gamma F^2\\ -\gamma F^{2*} & D(-\Omega)+\beta_{1sol}\Omega+\gamma P_0-k-2\gamma|F|^2\end{bmatrix}, \tag{5.5}$$

and $S=-\left(D(i\partial_T)+\frac{\beta_2}{2}\partial_T^2\right)F$.

If we look far from the soliton, where it tends to a CW background, then the system (5.4) reduces to:

$$\begin{bmatrix}D(\Omega)-\beta_{1sol}\Omega+\gamma P_0-k & \gamma P_0\\ -\gamma P_0 & D(-\Omega)+\beta_{1sol}\Omega-\gamma P_0-k\end{bmatrix}\begin{bmatrix}C_1\\ C_2\end{bmatrix}=\begin{bmatrix}0\\ 0\end{bmatrix}. \tag{5.6}$$

Equation (5.6) has non trivial solutions only if the determinant of its matrix is vanishing, which leads to the following expression for k [104]:

$$k_\pm=\frac{(D(\Omega)-D(-\Omega)-2\beta_{1sol}\Omega)\pm\sqrt{(D(\Omega)+D(-\Omega))(D(\Omega)+D(-\Omega)+4\gamma P_0)}}{2}, \tag{5.7}$$

where k_+ (k_-) corresponds to the expression with the $+$ ($-$). The frequency of the radiation can be found by solving $k(\Omega)=0$.

It is interesting to analyze the limit where the power is low ($\gamma P_0 \ll D(\Omega)$). By using a Taylor expansion, it can be readily found that phase-matching condition reduces to a simpler expression [105]:

$$D(\Omega)+\gamma P_0-\beta_{1,sol}\Omega\approx 0. \tag{5.8}$$

This expression can be interpreted by means of quasi-phase matching arguments. The wavenumber of the linear wave (k_{lw}) in a reference frame such as the soliton is at rest is given by $k_{lw}=D(\Omega)-\beta_{1sol}\Omega+2\gamma P_0$, where we have taken into account the nonlinear contribution due to XPM to the wavenumber, which is $2\gamma P_0$. The wavenumber associated to the dark soliton is $k_{DS}=\gamma P_0$. If the condition of quasi-phase matching $k_{DS}=k_{lw}$ is verified, then Eq. (5.8) is recovered. It is interesting to notice that this is the same equation obtained for the phase-matching of radiation emitted by dispersive shock waves, as shown in Ref. [144].

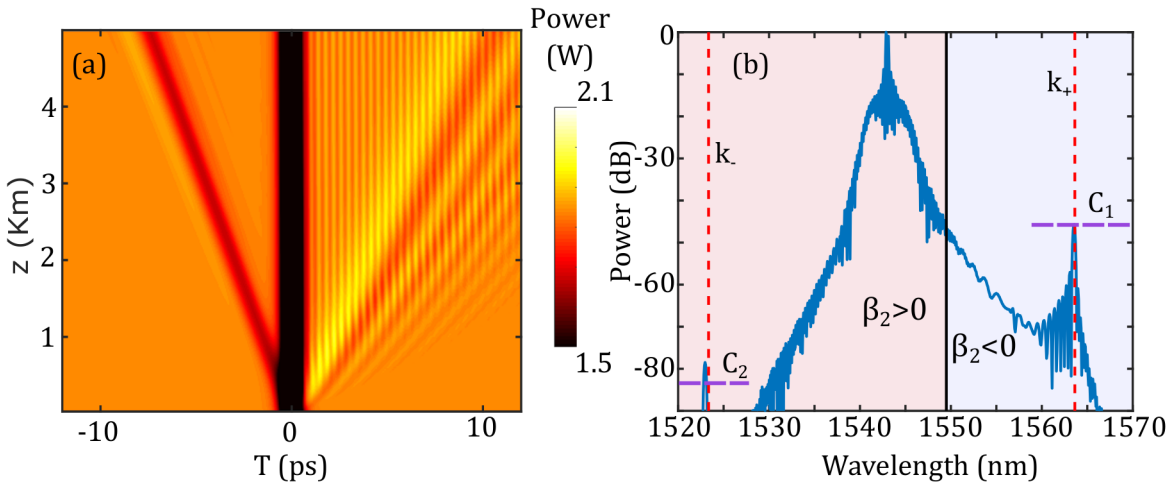

Figure 5.2: Cherenkov emission by a black soliton ($\phi = 0$). (a) Temporal evolution of the dark soliton. (b) Spectral output, black-solid line represents the ZDW and red-dashed line is the predicted by phase-matching wavelength of emission. Soliton parameters: $t_0 = 400$ fs, $\phi = 0$, $P_0 = 1.84$ W and $\lambda_0 = 1543$ nm. Dispersion parameters: $\lambda_{ZDW} = 1549.5$ nm, β_3 at ZDW: $\beta_3 = 1.15 \cdot 10^{-40}$ s^3/m.

To illustrate the accuracy of the predicted wavelength, the output spectrum of the previous simulation is shown in Fig. 5.2 (b). Black vertical line represents the ZDW and the two dashed red lines represent the resonance frequencies predicted by phase-matching. One of them (k_+) is efficiently amplified, while the other one (k_-) the transference of energy from the soliton is less important. Nevertheless both of them exhibit a good agreement with numerical simulation. The relative amplitude of both resonances given by Eq. (5.7) can be estimated by calculating the ratio between the amplitudes C_1 and C_2. We can determine C_1/C_2 obtaining the eigenvectors of matrix M in the resonance condition, i.e. $k_\pm = 0$:

$$\left|\frac{C_1}{C_2}\right| = \left|\frac{\gamma P_0}{D(\Omega_r) + \gamma P_0 - \beta_{1,sol}\Omega_r}\right|, \tag{5.9}$$

being Ω_r the frequency obtained from phase-matching. Denominator of Eq. (5.9) is expression (5.8), which is approximately zero when phase-matching is verified. Thus $|C_1| \gg |C_2|$, which means the frequency associated a k_+ is more efficient. The predicted difference of intensities between resonances using Eq. (5.9) is approximately of 37 dB. In figure 5.2 (b), the relation between C_1 and C_2 has been reported with dashed magenta lines. We can see that there is a good agreement between numerical simulations and theoretical predictions.

5.2.2 Amplitude of radiation

In the last section, it was shown that the frequency of Cherenkov emission is a function of the soliton grayness. However phase-matching does not give any information about the efficiency of the process, since it only reveals at what frequency momentum is conserved. Figure 5.3 (a) shows a false color plot of the output spectra from numerical simulations with different soliton grayness as initial condition. The horizontal axis represents the wavelength and the vertical axis the corresponding soliton grayness. Dashed line represents the wavelength at which phase-matching is verified. From these results, we see that the amplitude and wavelength depends on the grayness of the soliton. Radiation amplitude may be obtained by direct integration of the perturbation Eq. (5.2) as it has been already explored in [101] to obtain the amplitude of Cherenkov radiation from a bright soliton.

As we showed in the last section, $|C_1| \gg |C_2|$, thus the contribution of the second term of Eq. (5.3) is negligible, then the perturbation g can be considered of the form $g = G(z)\mathrm{e}^{-i\Omega_r t}$. By inserting this *ansatz* in Eq. (5.2), and neglecting the term $F^2 g^* e^{i2\Omega_r t}$ because of its fast temporal oscillations, the following equation is obtained:

$$i\partial_z G + i\bar{D}'(\Omega_r)\partial_\tau G + 2(\gamma|F|^2 - q)G = Se^{i\Omega_r \tau}, \tag{5.10}$$

where we have considered that k can be approximated by $k_+ \approx D(\Omega) + \gamma P_0 - \beta_{1,sol}\Omega$. The field g is considered to be spectrally very narrow, thus time partial derivatives with an order higher than two can be neglected ($\partial_T^n G = 0$, $n > 2$) and $\bar{D}'(\Omega_r) = -\beta_{1sol}\Omega_r + \beta_2\Omega_r + \beta_3/2\Omega_r^2$. Equation (5.10) admits the general solution:

$$G = \left(C_0 + \frac{\beta_3}{6}\int_0^{z'} dz[S]e^{i(\Omega_r(T+\bar{D}'(\Omega_r)z) - B(T+\bar{D}'(\Omega_r)z)}\right)e^{iB(T+\bar{D}'(\Omega_r)z)}, \tag{5.11}$$

where:

$$B(T+\bar{D}'(\Omega_r)z) = -\frac{2\gamma P_0 t_0\cos(\phi)}{\bar{D}'(\Omega_r)}\tanh\left(\frac{(T+\bar{D}'(\Omega_r)z)cos\ \phi}{t_0}\right). \tag{5.12}$$

By means of the change of variables $x \equiv (T+\bar{D}'(\Omega_r)z))/t_0$ and considering $G(z=0) = 0$, the amplitude can be written as:

$$C \approx \left|\frac{\sqrt{P_0}\beta_3\cos^3(\phi)}{6t_0^2\bar{D}'(\Omega_r)}\int_{-\infty}^{\infty} dx(4\mathrm{sech}^2(x) - 6\mathrm{sech}^4(x))e^{i\Delta\tilde{\omega}x}\right|, \tag{5.13}$$

where:

$$\Delta\tilde{\omega} = \left(\frac{\Omega_r t_0}{\cos(\phi)} + \frac{2\gamma P_0 t_0\cos(\phi)}{\bar{D}'(\Omega_r)}\right). \tag{5.14}$$

As the main contribution of this integral is in the neighborhood of $x = 0$, we can assume $\tanh(x) \approx x$. This lead to the following expression for the amplitude:

$$|G| \propto \frac{\cos^3(\phi)}{\bar{D}'(\Omega_r)} \Delta\tilde{\omega}^3 \sinh^{-1}\left(\frac{\pi\Delta\tilde{\omega}}{2}\right). \tag{5.15}$$

In order to compare this result with numerical simulations and experiments, we calculate the energy of the radiated wave, which can be approximated by supposing that it has a squared temporal shape, extending from the dark soliton center to the time delay of a linear wave with frequency Ω_r. Then, the generated wave energy is $E_g = T_g|G|^2$, where T_g is the time duration of the emitted wave which can be approximated by $T_g \approx D'(\Omega_r)L_{fiber}$. This argument to calculate the generated wave energy is the same as we employed in chapter 4 to calculate the energy of the generated wave. Both experimentally and numerically, the energy of radiated wave is obtained by directly integrating the spectrum.

Figure 5.3 (b) presents a comparative between numerical simulations (red line), theoretical prediction (blue line) and experiments (green dashed line). Results have been normalized to their maximum because the absolute value of energy is a quantity which can not be measured experimentally. Even though the agreement between the three curves is not perfect, it sheds some light on the physical understanding of the problem . We observe that there is a maximum of emission near $\phi = -\pi/4$. This fact can be explained as follows. The lower the grayness is, the closer to ZDW the resonance wavelength is situated, and then, the larger is the overlap of the soliton spectrum with anomalous dispersion regime. Like the bright soliton case [101] this fact increases the efficiency of Cherenkov emission. Nevertheless, for increasing values of $|\phi|$, the soliton spectrum becomes narrower, which traduces to a reduction of the overlapping between dark soliton and anomalous dispersion regime, being $|\phi| = \pi/2$ the limit where a dark soliton degenerate to a pure CW.

5.3 Interaction of a dark soliton with a dispersive wave

In this section, we analyze the interaction of a weak wave and a dark soliton. We consider that the weak wave is a finite temporal long pulse with a frequency different from that of the soliton. We assume that there is no temporal overlapping between the soliton and the input wave at the beginning of the process. As a consequence of the different group velocities, both pulses will concur at the same time position after some propagation, giving rise to the interaction. As the soliton produces a local variation of the refractive index, then like it happens in the interface between two media with different refractive index, one part

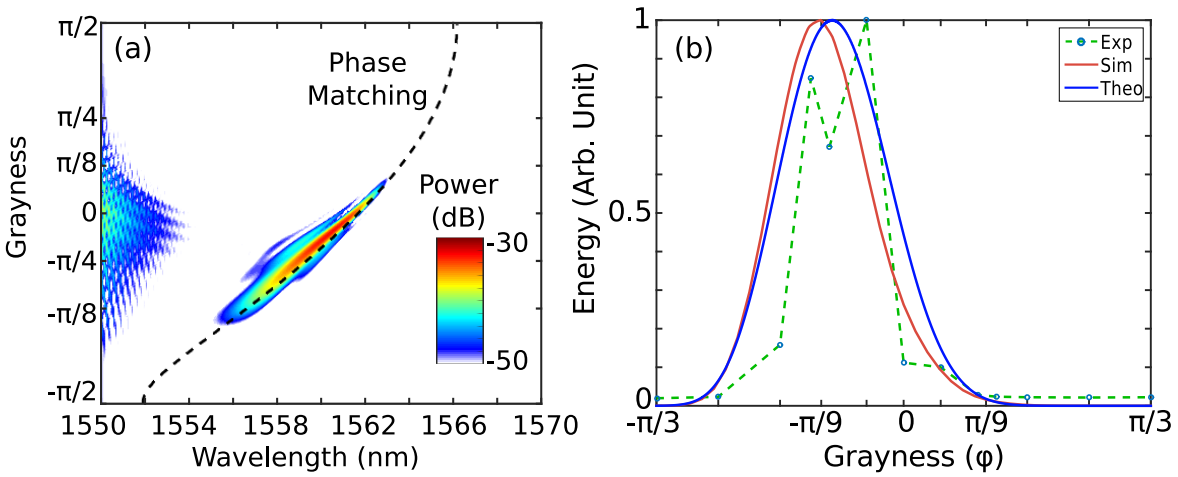

Figure 5.3: (a) False color plot of the power of the Cherenkov radiation as a function of wavelength (x-axis) and grayness (y-axis). Dashed-line represents the phase-matching condition as a function of grayness. Parameters: Fiber length 5 km, $t_0 = 400$ fs, $\lambda_{sol} = 1544$ nm, P_0 =1.54 W, $\beta_2 = 5 \cdot 10^{-28}$ s^2/m at 1544 nm, $\beta_3 = 1.15 \cdot 10^{-40}$s^{-3}/m. (b) Comparative of the energy predicted by theory (blue solid line), the one obtained by numerically solving NLSE (red line) and experimental results (dots and green dashed line).

of the energy of the weak wave will be reflected and the remaining will be transmitted. In our case dynamics is temporal, so concepts such as reflection and transmission may be misleading. Then reflection must be understood as a group velocity change, which necessarily translates in the generation of a new frequency. Transmitted wave is the portion of energy which does not interact with the soliton and goes through it without a change of frequency.

Figure 5.4 (a) shows the temporal evolution of a typical collision. This result has been obtained by direct integration of NLSE with HOD. Raman effect does not play any role in the collision process, thus it is neglected. At the beginning, a soliton with $\phi = \pi/8$ is placed at $T = 0$ and a weak Gaussian pulse with 5 % of amplitude of the soliton background is delayed by 5 ps. The soliton has a lower group velocity due its grayness, leading to the collision of the soliton and dispersive wave which takes place near 0.5 km. After, a part of the initial dispersive wave energy changes its group velocity and propagates toward positive time delays. This part is called reflected wave, while the remaining energy goes through the soliton without changing its velocity and is called transmitted wave.

5.3.1 Phase-matching

In this section, we detail the procedure to calculate the frequency of the reflected wave. Our starting point is Eq. (5.2), which describes the perturbation of a soliton. The perturbation equation is written as a superposition of a weak CW pump (ψ_p) and a generated wave (ψ_g):

$$g = \psi_p + \psi_g, \tag{5.16}$$

which inserted in Eq. (5.2) gives the following equation describing the dynamics of the generated wave:

$$\begin{aligned} &i\partial_z\psi_g + (D(i\partial_t) - k_g - i\beta_{1sol}\partial_t)\psi_g + \frac{\gamma}{3}\left(2|F|^2\psi_g + F^2\psi_g^* e^{i2\gamma P_0 z}\right) = \\ &-\frac{\gamma}{3}\left(2|F|^2\psi_p e^{i((k_p-k_g)z-(\Omega_p-\Omega_g)t)} + F^2\psi_p^* e^{i((2\gamma P_0-(k_p+k_g))z+(\Omega_p+\Omega_g)t)}\right). \end{aligned} \tag{5.17}$$

We have not considered here the source term associated to Cherenkov radiation because we supposed it to not be phase-matched and thus its role can be neglected. In the limit where the linear wave is spectrally narrow, ψ_g can be efficiently amplified if the dependence on z of the exponents in the right hand side of Eq. (5.17) vanishes, leading us to the expressions of phase-matching obtained in chapter 4:

$$k_p(\Omega_p) = k_g(\Omega_g), \tag{5.18}$$

$$k_p(\Omega_p) = 2\gamma P_0 - k_g(\Omega_g). \tag{5.19}$$

It is worth to note a crucial difference from the bright soliton case. Now the linear wave propagates over a background, which makes the dispersion relation to be different, as we discussed in section 5.2.1. Among these possible processes, the most efficient resonance is the one given by the first equation Eq. (5.18), as it has already been demonstrated for bright solitons [130] . Within the low power limit, phase-matching condition can be written as:

$$D(\Omega_p) - D(\Omega_g) = 2\beta_{1sol}(\Omega_p - \Omega_g). \tag{5.20}$$

When the soliton is black ($\phi = 0$), the expression obtained with a bright soliton is recovered, despite the fact that the linear waves propagate over a background. However, when the grayness does not vanish, solitons have an additional contribution to phase-number due to their intrinsic additional group velocity, which is present in a non-vanishing right hand side of Eq. (5.20). The presence of this term changes the generated wave frequency.

In figure 5.4, the output spectrum from the numerical simulation discussed previously

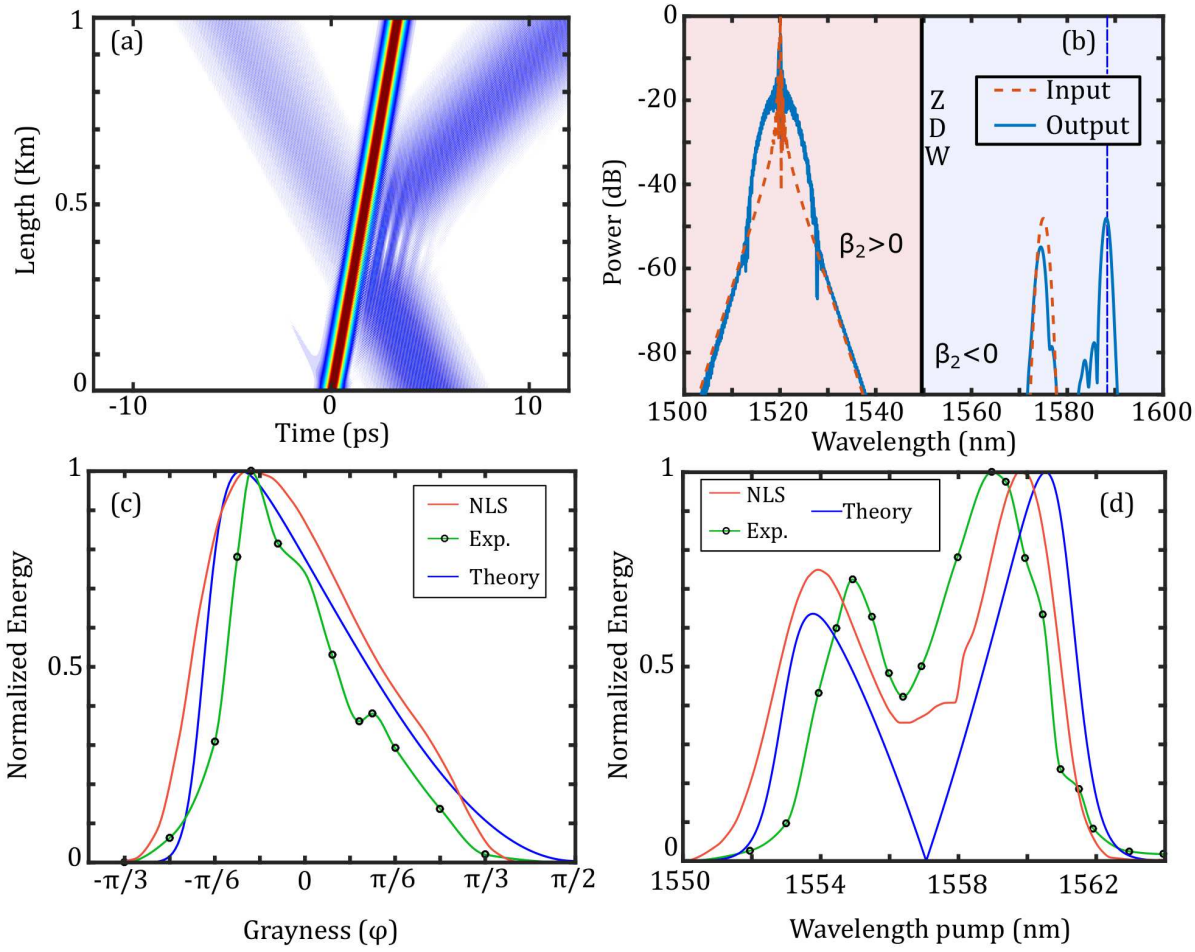

Figure 5.4: (a) Temporal evolution over 1 km propagation of the collision between a weak pulse with $\lambda_{pump} = 1575$ nm and a soliton with $t_0 = 300$ fs, $\lambda_0 = 1520$ nm and $\phi = \pi/8$. The represented quantity is $||A(T,z)|^2 - P_0|$ (b) Output spectrum of propagation shown in (a), dashed line represents input spectrum and the output spectrum is represented by the blue solid line. The black vertical line represents the ZDW. (c) and (d) Comparative among numerical simulation (red solid line), theory (blue line) and experiments (green line with experimental points in black). Parameters are reported in the text.

is shown. Dashed orange line represents the input spectrum and solid blue one is the output spectrum. Dashed blue vertical line is the corresponding frequency of resonance predicted by phase-matching. This result confirms that the obtained relation to find the generated frequency coincide with the results found by direct numerical integration of NLSE.

5.3.2 Amplitude of generated wave

The efficiency of the process can be calculated by taking advantage of the scattering picture introduced before. Here, the soliton is considered as the scattering potential and g plays the role of the scattered wave, where the reflected (transmitted) part is the generated (pump) wave. This way of thinking directly gives the process efficiency if wavepackets are of a finite time duration, however some modifications should be adressed if a pure CW is considered. Starting from the perturbation equation Eq. (5.1), a serie of transformations and approximations are needed to go towards finding a z independent Schrödinger equation, which will be found to rule the process. The employed procedure has been inspired from the one depicted in [145], but adapting the calculation to dark soliton peculiarities.

The first step is to write the perturbation in the form $g = \Psi(\tau)e^{ikz}$, where k is given by the expression (5.7) calculated either at Ω_p or Ω_g with the $+$ sign. This form of the perturbation can be supposed since both generated and pump have the same wavenumber, as given by Eq. (5.18). This change transforms the initial partial derivative equation in to an ordinary differential equation. The field $\Psi(\tau)$ accounts for both frequencies, pump and generated. When this form of $g(z,T)$ is substituted in Eq. (5.17) , non-phase matched terms are dropped and the low power approximation is done, to find:

$$\left[\left(D\left(i\frac{d}{dT}\right) - i\beta_{1sol}\frac{d}{dT}\right) - (2\gamma P_0\cos^2(\phi)\mathrm{sech}^2\left(\frac{T\cos(\phi)}{t_0}\right) + D(\Omega_p) - \beta_{1sol}\Omega_p)\right]\Psi = 0. \tag{5.21}$$

This equation can be simplified by performing a phase-rotation $\tilde{\Psi} = \Psi e^{i\Omega_{GVM}\tau}$, where we choose Ω_{GVM} such as $D'(\Omega_{GVM}) = \beta_{1sol}$. In this way, the first derivative appearing on the second term can be simplified. If only up to β_3 is considered, this frequency is given by the expression:

$$\Omega_{GVM} = \frac{-\beta_2 - \sqrt{\beta_2^2 + 2\sin(\phi)\beta_3\sqrt{\gamma\beta_2 P_0}}}{\beta_3}. \tag{5.22}$$

In the neighborhood of Ω_{GVM}, dispersion relation can be approximated by a parabola, hence HOD terms involving derivatives with order higher than 2 are safely neglected, then

the following equation is obtained:

$$\left(\text{sign}(\beta_2(\Omega_{GVM}))\frac{|\beta_2(\Omega_{GVM})|}{2}\frac{d^2}{dT^2} + (2\gamma P_0\cos^2(\phi)\text{sech}^2(T\cos(\phi)/t_0) - \Delta D)\right)\Psi = 0, \tag{5.23}$$

where $\beta_2(\Omega_{GVM}) = \beta_2 + \beta_3\Omega_{GVM}$ and $\Delta D = D(\Omega_p) - D(\Omega_{GVM})$. This expression is a z independent Schrödinger equation, with $\beta_2(\Omega_{GVM})$ playing the role of mass and the dark soliton being the scattering potential. Depending on the sign of $\beta_2(\Omega_{GVM})$, Eq. (5.23) exhibits different kinds of solution. If sign$(\beta_2(\Omega_{GVM}))$ is positive, solutions of Eq. (5.23) can be bound states, while if sign$(\beta_2(\Omega_{GVM}))$ is negative, we have a scattering problem. In our case, we are restricted to anomalous dispersion regime thus we will be interested in the scattering solution of Eq. (5.23). This kind of equations have been deeply studied in the context of quantum mechanics and it is usual to describe their solution by a reflexion (R) and transmission coefficient (T) verifying the condition $R + T = 1$. In the case of a hyperbolic secant shaped potential as the one given by Eq. (5.23), R is given by the expression [146]:

$$R = \frac{\cosh^2\left(\frac{\pi}{2}\sqrt{16\frac{|\beta_2(\Omega_{GVM})|}{\beta_2} - 1}\right)}{\cosh^2\left(\frac{\pi}{2}\sqrt{16\frac{|\beta_2(\Omega_{GVM})|}{\beta_2} - 1}\right) + \sinh^2\left(\frac{\pi t_0\Delta\Omega}{cos(\phi)}\right)}. \tag{5.24}$$

If $\phi = 0$, then the expression obtained when a bright soliton was studied is recovered [145], and R does not depend explicitly on β_2. The value $R = 1$ means a perfect reflection, which translates in a complete conversion to the generated wave. However the condition $R = 1$ is only found when $\Omega_{GVM} = \Omega_p$, i.e when pump and soliton have the same group velocity. This result means that the pump will need an infinite length to interact with the soliton in order to be completely converted, and we can conclude that it is physically impossible to have a total conversion from pump to generated frequency. Bright solitons are subjected at the same restriction [132], [145].

The simultaneous generation of a single soliton and a weak pulse with different frequency represents a real experimental challenge. The main obstacle to overcome is the synchronization of the two pulses delivered by two different lasers. The solution that we implemented was to only use one laser with a broad spectrum. In addition, waveshapers were modified in order to add a small pulse at the frequency of the initial dispersive wave. Nevertheless, the obtained pulse is long enough to be considered as a CW. Then, the theory

must be adapted to take into account the fact that we use in experiments quasi-CW instead of short pulses. To do so, we consider that only a energy portion E_0 of the initial dispersive wave interacts with the soliton, which can be approximated by $E_0 \approx P_{CW}(|\bar{D}'|L_{fiber})$, where $\bar{D}'$ is the group velocity difference between the soliton and CW and L_{fiber} is the fiber length. The energy of the generated wave can be obtained by using the definition of the reflection coefficient $R = E_{generated}/E_0$ [132]:

$$E_{generated} \propto |\bar{D}'(\Omega)|R = \left| \left(-\sqrt{\beta_2 \gamma P_0}\sin(\phi) + \beta_2 \Omega_p + \frac{\beta_3}{2}\Omega_p^2 \right) \right| R. \tag{5.25}$$

From Eq. (5.25) we can see that when a soliton interacts with a CW with the same group velocity, the generated wave energy goes to zero. In order to test the validity of these results, a series of experiments and numerical simulations are performed. These measurements consist in quantifying the generated wave energy by directly integrating the spectrum, as described in Sec. 5.2.2, and compare them with the expected result obtained by theoretical arguments. As already discussed, the absolute value of the energy cannot be obtained experimentally, then data are normalized to their maximum to be able to compare all three quantities. In a first case, the frequency of the initial CW pump was fixed to 1559 nm and the grayness of soliton with wavelength 1542 nm and $t_0 = 600$ fs is changed. The obtained results are displayed in Figure 5.4 (c), where the x-axis reports ϕ and the y-axis the corresponding normalized measured/calculated energy. One can notice a maximum near $-\pi/6$, then the efficiency of the process decreases rapidly to zero when going to negative grayness and it decreases in a smoother way for positive ϕ. All three results have a good agreement. In a second series of experiments, the grayness of the soliton was fixed to 0 and the CW pump wavelength is changed. In Figure 5.4 (d), the normalized energy as a function of wavelength is plotted. The energy goes to zero when the pump wavelength is near 1570 nm, because at this wavelength, CW pump and soliton have the same group velocity as predicted by Eq. (5.25). Conversion of energy has two maxima near 1553 and 1562 nm. In this case, there is also a good agreement between the three curves.

Summary

In this chapter, the interactions between dark solitons and dispersive waves have been analyzed. The results are summarized hereinafter:

- The radiation emission by a dark soliton has been studied. We presented a theo-

retical background in order to understand the experimental results obtained at our laboratory.

- A general understanding of the interactions between dark solitons and weak waves has been developed. We have found a general form of the phase-matching relation and amplitude for an arbitrary grayness of the solitons. These results show a good agreement with numerical simulations and experiments.

Part III

Nonlinear phenomena in multimode fibers

CHAPTER

SIX

STATE OF THE ART

Multimode optical fibers (MMF) are at the beginning of a new eve. These fibers are attracting much interest because of their capability to transport much more information than single-mode fibers thanks to spatial multiplexing. For imaging, it will traduce to an improvement of image quality [147]. For telecommunications, using the spatial degree of freedom may avoid the capacity crunch that optical systems are about to suffer [148].

MMF are known since the very beginning of optical fiber technologies and were already proposed as a way of multiplexing signals in the 80s [149]. Nevertheless, these guides were considered of low quality as a consequence of the intrinsic randomization of light when propagating along a MMF. At the origin of this randomization, there are the possible fiber imperfections and microbendings, whose effect is to arbitrarily couple modes and to convert the highest quality input beam into a low quality and speckled output. However, this speckle remains deterministic, that is the reason why this problem is overcome in linear optics by obtaining the transfer matrix and its principal modes [150].

Nonlinear optics in MMF also predates its counterpart in single-mode fibers. Its complexity made the subject almost unapproachable, although some remarkable findings such as the first observation of FWM in optical fibers were done using multimode fibers [151]. Single-mode fibers, especially PCF, have lead to spectacular results for the production of highly broadband light sources [94]. However, due to the small size of the core of single-mode fibers, it is easy to reach the power density threshold for silica damaging. By increasing the core size, intensity is reduced but guides may become multimode, and thus, the involved phenomena become much more complex [152]. The necessity to deeply understand the nonlinear effects which may be present and the opportunity of finding

new light sources rised an incredible research interest in this topic [153]. Among all the fiber kinds, there is one attracting the most attention because of its good qualities for observing multimode effects: highly multimode parabolic GRIN fibers. In these guides, the group velocity of waves is predominantly given by the material and thus all modes travel with similar velocity [66], increasing the temporal overlap between pulses carried by different modes and thus, the efficiency of nonlinear effects. In addition, GRIN fibers show self-imaging. By producing a periodic pattern of intensity in z, a variation of index is induced, giving birth to a vast amount of interesting physics. Research in multimode fibers has given three important breakthroughs: beam self-cleaning, multimode solitons and spatio-temporal modulation instability (Geometrical Parametric Instability).

Beam Self-cleaning: As previously mentioned, light propagating along a MMF in linear regime spreads its energy over all guided modes due to fiber imperfections. When the input power is increased, this phenomenon is reversed and the beam energy flows to the lowest order modes, mainly to the fundamental one [154], [155]. This effect has been observed either for CW [154] and for femtosecond pulses [156]. Self-cleaning may be related to light-condensation [157], [158], which is a phenomenon analog to Bose-Einstein condensates. Nevertheless, there is still some controversy about its theoretical explanation [159].

One of the most direct technological application is in high energy fiber lasers [160], where an active GRIN fiber could be employed to generate high-energy Gaussian beams.

Multimode solitons: Spatiotemporal solitons, also called optical bullets, have always attracted the attention of researchers [161]. These objects are waves confined both on transverse propagation plane and temporal domain due to diffraction and dispersion compensation by nonlinearity. These objects are not stable in Kerr bulk media [162], nevertheless multimode solitons (MMS) can exist in waveguides with Kerr nonlinearity as theoretically predicted in the 80s [163], [164]. MMS in MMF are characterized for having their energy distributed among several guided modes, and nonlinear effects compensate the eventual dispersion of modes.

The experimental demonstration of MMS was performed in 2013 [148] in optical fibers, where solitons were observed in a multimode GRIN fiber. In this experiment, a pulse which kept its temporal shape but spatially breathed was observed. The fiber was chosen in order to reduce the group velocity difference between modes and to avoid pulse splitting [165]. The observation of spatiotemporal solitons naturally brought to femtosecond supercontin-

uum generation. In references [166]–[168] a multimode supercontinuum was observed by injecting femtosecond pulses in a GRIN fiber. Specially remarkable was the ultra broad band emission associated to MMS. This new mechanism of frequencies broadening is added to the already existing ones as Cherenkov emission and FWM and it opens a new way to taylor emission of broad band light sources.

Geometrical Parametric Instability (GPI): A CW is unstable when propagated along a multimode GRIN fiber in normal dispersion regime, as theoretically predicted by S. Longhi [169]. The physical mechanism beneath this penomenon is the refractive index grating produced by the periodic intensity associated to self-imaging. This effect is very similar to the energy transfer from radial oscillations to longitudinal sound waves in a BEC trapped in a cigar potential [170].

GPI was first experimentally observed by K. Krupa et al [69]. In this experiment a quasi-CW pump at 1064 nm produced bands in the visible light spectral range. After this first observation, many studies have been carried out to obtain supercontinuum sources [171], [172], to relate GPI with second harmonic generation in a fiber [173], and even to observe a cascaded GPI [174], where GPI-produced bands themselves gove birth to new bands. GPI has been related to beam self-cleaning [155], but this connection remains unclear.

6.1 Mathematical and numerical modeling

To describe all the aforementioned effects in MMF, two different approaches have been employed: coupled mode nonlinear Schrödinger equation (CMNLS) and generalized nonlinear Schrödinger equation (GNLSE):

Coupled mode nonlinear Schrödinger equation: Initially proposed by Poletti and Horak [175] and simplified afterwards [176], this equation is written as:

$$\partial_z A_p = i\Delta\beta_0^{(p)} A_p - \Delta\beta_1 \partial_T A_p + \sum_{m=2} \frac{i^{m+1}}{m!} \beta_m \partial_T^m A_p + \frac{i n_2 \omega_0}{c} \sum_{l,m,n}^{N} S_{plmn}^K A_l A_m A_n^*, \qquad (6.1)$$

where A_p is the time envelope corresponding to the p-mode of the fiber, $\Delta\beta_0$ is the difference of phase velocity between modes at the carrier frequency ($\beta_0^{(p)} - \beta_0^{(1)}$), $\Delta\beta_1$ is the group velocity difference between modes and β_m are the rest of coefficients describing the modal dispersion. The last term takes into account the nonlinear coupling between modes

due to the Kerr effect, being S^K_{plmn} a 4-dimensional tensor describing the weight of each interacting term and which directly depends on the superposition integral of the spatial modes:

$$S^k_{plmn} = \frac{\int dxdy[F_p F_l F_m F_n]}{\left[\int dxdy F_p^2 \int dxdy F_l^2 \int dxdy F_m^2 \int dxdy F_n^2\right]^{1/2}}. \tag{6.2}$$

From a numerical point of view, this equation is advantageous when the number of considered modes is not very high, since the number of coupling terms increases as N^4 (being N the number of modes) and then the efficiency of evaluation also decreases. To overcome this problem, one proposed solution has been implementing highly parallel algorithms using GPU [177], following the already employed algorithms in long-distance single-mode simulation [178]. Another solution to solve this equation has recently been proposed [179], which is based on the real-space Gaussian quadrature integration of the nonlinear term instead of calculating the sum of overlapping modes.

From a physical point of view, Eq. (6.1) permits to resolve the modal content of the field, which can be an advantage for the interpretation of process involving a few different modes, such as intermodal FWM, XPM [43]... but can hide under its complexity collective effects such as GPI [180] or MMS.

Generalized nonlinear Schrödinger equation: This equation read as:

$$i\partial_z E + \frac{1}{2\beta_0}\nabla_\perp^2 E + \sum_{m=2}\frac{\beta_m}{m!}(i\partial_T)^m E - \frac{\beta_0\Delta}{r_c^2}r^2 E + \frac{\omega_0 n_2}{c}|E|^2 E = 0, \tag{6.3}$$

where $r^2 = x^2 + y^2$, $\nabla_\perp^2 = \partial_x^2 + \partial_y^2$ is the transverse Laplacian, E is the electric field envelope expressed in $\sqrt{W}/m$, $\beta_0 = \omega_0 n_0/c$, n_0 is the refractive index at the center of the core and β_m are the coefficients describing light dispersion. In the literature, the confining potential describing the guide (4th term in the equation) is commonly approximated as a parabola, which corresponds to a pure harmonic potential. Equation (6.3) bears a resemblance to Gross-Pitaevskii equation [181], used for describing Bose - Einstein Condensate, but in this case the Laplacian describes diffraction of light, z and t have exchanged their roles, the linear potential describes the waveguide geometry and last term describes Kerr effect. This equation, unlike CMNLS, describes the whole electric field evolution in 3+1 dimensions. From a numerical point of view, GNLSE is less efficient than coupled mode nonlinear Schrödinger equation when the number of involved modes is low, but it becomes competitive to describe highly multimode fibers. Equation (6.3) has been

successfully employed for describing GPI [69], [169] and MMS. It is worth to point out that this equation does not take into account the dependence on frequency of the guide. This is a very crude approximation, which can affect the shape and propagation constant of modes, and thus the nonlinear interaction among them.

CHAPTER

SEVEN

GEOMETRIC PARAMETRIC INSTABILITY IN UNIFORM GRIN FIBERS

Contents

In this chapter, geometric parametric instability is explained from a fundamental point of view. We describe a series of mathematical tools needed for the theoretical and numerical analysis of the phenomenon. We first derive an equation describing light propagation in a GRIN fiber. In the followed approach, our starting point is the unidirectional pulse propagation equation (UPPE). From this equation, GNLSE is found in section 7.1.1. In section 7.2, the numerical methods that we employed for numerically solving GNLSE are described. Finally, with all these tools, GPI in a constant core fiber will be studied in section 7.3.

7.1 Derivation of propagation equations

In the present section, we detail how to derive the GNLSE, which is the model we use for describing light propagation in multimode fibers. At the end of this section, the relation between GNLSE and a CMNLSE is outlined. The objective of this model is to describe

nonlinear phenomena happening in a relatively short fiber (length of the order of the centimeter), then all the assumed approximations that we will consider have sense in this context.

7.1.1 Generalized nonlinear Schrödinger equation

The starting point of our discussion is the so-called UPPE in the scalar limit, which is a reduction of Maxwell's equations where only the forward propagating field is taken into account:

$$\partial_z \tilde{E}(k_\perp, \omega, z) = ik_z \tilde{E}(k_\perp, \omega, z) + \frac{i\omega^2}{2\epsilon_0 c^2 k_z} \tilde{P}(k_\perp, \omega, z), \tag{7.1}$$

being $k_z = \sqrt{\beta^2 - k_\perp^2}$, where k_z, β and $k_\perp$ are respectively the z-component, modulus and transverse components of the wave vector. The function $\tilde{P}(k_\perp, \omega, z)$ represents the nonlinear polarizability of the material in the most commonly used version of the UPPE, but we will specify it better hereinafter. To refer to the electric field, we will use the following notation: $\tilde{E}(k_\perp, \omega, z)$ when the field is both spatially and temporally in Fourier domain, $\bar{E}(r, \omega, z)$ when it is only the temporal coordinate which is in Fourier domain and finally $E(r, T, z)$ when the electric field coordinates are time and space. UPPE was initially proposed to describe ultra-short and very intense pulse propagation in bulk media and gases [182], [183], and after it was adapted to model waveguides with strong refractive index contrast [184]. A one-dimensional version of this equation has been succesfully employed to describe interaction between fields and their own conjugates in bulk media and PCF [185], [186]. It is important to remark that in presence of Kerr effect, there is a coupling between forward and backward propagated fields [187], but in our case this effect is negligible and it is not taken into account. Indeed, forward-backward coupling becomes effective for values of intensity well above the range we are going to consider.

UPPE has at least two remarkable differences with the previous equations described until now:

- The whole field is written in frequency domain, both temporally and spatially unlike NLSE, GNLSE and CMNLSE, where the field is described in the time domain. By writing the equation in this way, diffraction can be exactly solved and the operator describing the propagation is constant (k_z). The other side of the coin is that in this representation Kerr-nonlinearity and the waveguide are included in the model in a less straightforward manner.

- In Eq. (7.1), the SVEA (slowly varying envelope approximation) has not been taken

into account, which means that $E(r,t,z)$ is a real quantity describing the fast oscillations of the carrier frequency. This kind of equations are called carrier resolved equations [72] while NLSE, GNLSE and coupled mode nonlinear Schrödinger equation are referred as envelope equations.

When P in expression (7.1) only considers the nonlinear contribution to polarizability, this equation describes light propagation in a nonlinear homogeneous media. In our case, light propagates in a waveguide, thus the expression must be modified to take this effect into account. To this aim, we assume the variations of refractive index to be weak, which is usually the case for an optical fiber. The linear contribution to polarizability in a waveguide with infinite parabolic refractive index is written as:

$$\bar{P}_L(r,\omega) = \epsilon_0 \left[\chi_1(r=0,\omega) - 2\Delta(\omega) n_{core}^2(\omega) \left(\frac{r}{r_{core}} \right)^2 \right] \bar{E}(r,\omega), \tag{7.2}$$

where we have employed the relation $n^2(\omega) = 1 + Re(\chi(\omega))$. The first term corresponds to the linear polarizability at the core center and the second one is a much smaller term ($\Delta \ll 1$) which takes into account the radial distribution of the refractive index. Then, the second term can be considered as a perturbation and be included as another contribution to P, while the first term fixes $\beta(\omega)$ [188]. Therefore, light propagates as if it were in a homogeneous medium with the same characteristics as the center of the core, but perturbed by a weak variation of the refractive index, the effect of which is to confine light. By assuming that the linear polarizability has the form of Eq. (7.2) , we are assuming that: i) The presence of the cladding is negligible, whose consequence will concern the shape of propagated modes and its dispersion relation. ii) The waveguide is perfect and its parameters do not change along the propagation. This hypothesis prevents the linear coupling between the different modes.

We can perform some simplifications in order to make the model easier to solve and to work with. The most evident is to use paraxial approximation, which consists in considering $\beta^2 \gg k_\perp^2$. From this assumption k_z can be expanded in a Taylor series, obtaining as a result $k_z \approx \beta(\omega) - k_\perp^2/(2\beta(\omega))$. After doing this approximation, the equation is called forward Maxwell equation (FME) and it was one of the first employed equations to explain supercontiuum generation in PCF [189]. By transforming back to spatial direct domain, the following equation is obtained:

$$\partial_z \bar{E}(r,\omega,z) = i\left(\beta(\omega) + \frac{\nabla_\perp^2}{2\beta(\omega)}\right)\bar{E}(r,\omega,z) - \frac{i\omega n_{core}(\omega)\Delta(\omega)}{c}\frac{r^2}{r_{core}^2}\bar{E}(r,\omega,z) + \\ + \frac{i\omega}{2\epsilon_0 c n_{core}}\bar{P}_{NL}(r,\omega,z), \quad (7.3)$$

The nonlinear contribution can not be easily obtained in time Fourier Domain, however it can be easily found in direct time domain. In order to write P_{NL}, we use the same approach employed in reference [40]. The first step is to express the electric field in the form: $E = \frac{1}{2}\mathcal{E}(r,z,t)\exp(i\beta_0 z - i\omega_0 t) + c.c$, where $\beta_0 = \omega_0 n_{core}(\omega_0)/c$, being ω_0 an arbitrary frequency and $n_{core}(\omega_0)$ the refractive index at the core center at frequency ω_0. The most convenient choice for ω_0 is the carrier frequency of the pulse. Then, by only keeping terms oscillating at frequency ω_0 and neglecting the THG term and the interaction of $\mathcal{E}$ and its own conjugate, we obtain that the nonlinear polarizability verifies:

$$P_{NL} = \frac{3\epsilon_0}{4}\chi^{(3)}_{xxxx}E(r,t,z)\int_0^{+\infty} R(t)|\mathcal{E}(r,t-t',z)|^2 dt', \quad (7.4)$$

where $R(t)$ is the Raman response function and it is given in section 1.4.2. The next step is to change the reference frame from the laboratory to a one traveling at the group velocity of ω_0. Then by performing the change of variables $\partial_z = \partial_z + i(\omega-\omega_0)\beta_1$, we obtain :

$$\partial_z \bar{\mathcal{E}}(r,\omega,z) = i\left(D(\omega) - d(\omega)\nabla_\perp^2\right)\bar{\mathcal{E}}(r,\omega,z) - iG(\omega)\frac{r^2}{r_{core}^2}\bar{\mathcal{E}}(r,\omega,z) + \chi\mathcal{F}(f_{NL}), \quad (7.5)$$

where $D(\omega) = \sum_{n=2}(d^n\beta(\omega_0)/d\omega^n)(\omega-\omega_0)^n$; $d(\omega)$ and $G(\omega)$ are respectively the Taylor development of $1/(2\beta(\omega))$ and $\omega n_{core}(\omega)\Delta(\omega)/c$ around ω_0, $\mathcal{F}$ is the Fourier transform, $\chi = \omega_0 n_2/c$ and f_{NL} is:

$$f_{NL} = \left(1 + \frac{i}{\omega_0}\partial_t\right)\mathcal{E}\int_0^{+\infty} R(t)|\mathcal{E}(r,t-t')|^2 dt'. \quad (7.6)$$

From Eq. (7.5), we can identify the four different physical effects taking part in light propagation: material dispersion, diffraction, guide effect and nonlinearity. At lowest order of the Taylor developments of $d(\omega)$ and $G(\omega)$, and also neglecting the self-steepening

effect, Eq. (6.3) described in chapter 6 is recovered:

$$i\partial_z\mathcal{E} + \frac{1}{2\beta_0}\nabla_\perp^2\mathcal{E} + \sum_{m=2}\frac{\beta_m}{m!}(i\partial_T)^m\mathcal{E} - \frac{\beta_0\Delta}{r_c^2}r^2\mathcal{E} + \frac{\omega_0 n_2}{c}|\mathcal{E}|^2\mathcal{E} = 0, \tag{7.7}$$

The most remarkable physical feature which comes thereof this approximation is that, neglecting dispersion of $d(\omega)$ and $G(\omega)$ implies that the spatial behavior of light does not depend on its frequency. This means that the guided modes shape is the same in the whole spectrum. We will restrict to problems where neglecting higher orders of $d(\omega)$ and $G(\omega)$ is a safe approximation. Disregarding these contributions has lead to a good agreement between numerical simulations and experimental results [69].

Coupled mode nonlinear Schrödinger equation

Writing Eq. (7.5) as coupled mode equation allows us to find some physical insights. Therefore if the electric field is written as $E = \sum_p F_p(r)A_p(t,z)$ where F_p is the corresponding mode spatial profile as given by Eq. (1.15), and A_p is the envelope associated to the m-th spatial profiles, a system of coupled equation describing the envelopes can be obtained [175]

$$\begin{aligned}\partial_z A_p = {} & iD_p(i\partial_t)A_p + \\ & + \frac{in_2\omega_0}{c}\left(1 + \frac{i}{\omega_0}\partial_t\right)\sum_{l,m,n} S^K_{plmn}A_l\int_0^\infty R(t)A_m^*(t-t',z)A_n(t-t',z)dt',\end{aligned} \tag{7.8}$$

being S_{plmn} the superposition integral defined in Eq. (6.2) and the corresponding dispersion relation which is expressed such as:

$$\beta_p(\omega) = D(\omega) - \frac{\sqrt{2\Delta}}{r_{core}}(2p+1), \tag{7.9}$$

where we have only considered modes with $m = 0$. Dispersion operator is composed by two terms in contrast to Eq. (7.7). The first one describes material dispersion and it is the same as Eq. (7.7). The second term is due to the waveguide and corresponds to $\Delta\beta_0$ in Eq. (6.1). Note that the waveguide only contributes to dispersion via a constant term, which means that all modes travel exactly at the same group velocity and share all dispersion orders higher than 1. The underlying reason for this result is because guide dispersion has been neglected. Nevertheless, the real dispersion of the mode can be calculated taking into account the dependence on ω of the relative difference of refractive index Δ.

Then, if the number of considered modes is high enough, both equations (7.7) and (7.8) are completely equivalents and both describe the same physics. In this manuscript, we will use as a model GNLSE (Eq. (7.7)) instead of CMNLS (Eq. (7.8)).

7.2 Numerical methods for solving GNLSE: The Hankel transform

The geometry of circular optical fibers is radially symmetric. In most cases, the beam exciting the fiber also presents circular symmetry and it is injected at the center of the fiber. This fact will reduce the number of considered dimensions, since the beam will keep its circular symmetry during the whole propagation. By writing the Laplacian in cylindrical coordinates and assuming circular symmetry, we obtain the following equation:

$$i\partial_z\mathcal{E} + \frac{1}{2\beta_0}[r^{-1}\partial_r(r\partial_r)]\mathcal{E} - D(i\partial_T)\mathcal{E} + \frac{\beta_0\Delta}{r_{core}^2}r^2\mathcal{E} + \chi f_{NL} = 0. \tag{7.10}$$

Equation (7.10) can be solved using the split-step method, which consist in breaking Eq. (7.10) in two different steps [40]. The first one accounts for the linear effects which in this case consists in diffraction, guide and dispersion, and the other one accounts for nonlinear contributions.

Linear part The linear part of Eq. (7.10) is composed of the first four terms in the right hand side. To solve this part, we employed a pseudo-spectral method, which consists in transforming the differential operator to a domain where it is a constant. In Cartesian coordinates, such a transformation is a Fourier transform and in that case, the fast Fourier transform (FFT) can be employed. However, the spatial Fourier transform of a function in cylindrical coordinates and circular symmetry is the Hankel transform (HT) of order 0, which transforms $r^{-1}\partial_r(r\partial_r)$ to $-s^2$, where s is the corresponding associated frequency to this integral transformation. The forward and backward HT of p-order are defined as:

$$f_2(s) = 2\pi\int_0^\infty f_1(r)J_p(2\pi rs)rdr \quad , \quad f_1(r) = 2\pi\int_0^\infty f_2(s)J_p(2\pi rs)sds, \tag{7.11}$$

J_p being the Bessel function of order p. As in the case of Fourier transform, there are algorithms to calculate this transform efficiently. These methods are depicted in reference [190] for the zero-order HT and generalized to order p in [191] and are called discrete

Hankel transform (DHT). In this operation, sampling points are not equally spaced as in the FFT. In the DHT points are given by scaling zeros of the corresponding Bessel function ($r_i = (u_i/u_N)\ R$), where r_i is the ith-point of the grid, u_i verifies the condition $J_p(u_i) = 0$ and R is the maximum radius. In a similar fashion, s points are scaled in the way ($s_i = (u_i/u_N)/R$). Even if DHT provides a good efficiency, it is still far from the performance obtained by the FFT algorithm. Nevertheless the reduction of one spatial coordinate makes the solution of Eq. (7.10) much more efficient than solving Eq. (7.7) by means of FFT.

Nonlinear part The nonlinear part is composed by the last term in Eq. (7.10). This part of the equation is solved in two different ways, depending whether Raman effect is included or not. If Raman scattering is not taken into account, we use the approximation:

$$\mathcal{E}(r, T, z + \Delta z)) \approx \mathcal{E}(r, T, z) \exp(i\chi|\mathcal{E}|^2 \Delta z), \tag{7.12}$$

where Δz is the length of the step. However, when Raman scattering is included, we solve the nonlinear part by means of a Runge-Kutta method of fourth order (RK4) [192]. This way of solving the equation is equivalent to the algorithm employed to integrate numerically the nonlinear part of the (1+1)D GNLSE, reiterated for each spatial point used to sample the field $\mathcal{E}$.

7.3 Geometric parametric instability in a uniform fiber

Geometric parametric instability is a kind of modulation instability whose origin resides in the spatio-temporal behavior of light in multimode fibers. In this section, we will analyze GPI within the limit of an axially uniform fiber. To describe the mechanism which triggers GPI, we start studying the spatial dynamics of a CW beam in a parabolic GRIN fiber. After, the temporal coordinate shall be included. Then we will study the dynamics of perturbations over the CW and under which conditions MI can be produced.

7.3.1 Spatial evolution

In section 1.5.2, we discussed the periodic behavior of intensity in a GRIN fiber, referred as self-imaging, and we found the intensity evolution as a periodic pattern of interference of several modes in the linear regime. In this section, we analyze the evolution of a CW by

means of GNLSE in the monochromatic limit (i.e. $\partial_T = 0$):

$$i\partial_z E(r,z) = \frac{1}{2\beta_0}\nabla_\perp^2 E(r,z) - \frac{\beta_0 g_0}{2} r^2 E(r,z) + \chi|E(r,z)|^2 E(r,z), \tag{7.13}$$

where we have defined the quantity $g_0 = 2\Delta/r_{core}^2$. The inclusion of Kerr nonlinearity does not destroy the self-imaging process and the beam keeps its periodic behavior [193]. Moreover, it has been shown that Eq. (7.13) admits self-similar solutions with the form of Gaussian beams which are linearly stable, and these solutions breath with the same periodicity as a beam in the linear limit [194]. The evolution of E can be approximated by means of a variational approach if the field is supposed to have a Gaussian shape [193]. Here, we only report field's intensity obtained through variational techniques, since the phase will not play any relevant role in our analysis:

$$|E(x,y,z)|^2 = A_0^2 \left(\frac{a_0}{a(z)}\right)^2 \exp\left(-\frac{r^2}{a(z)^2}\right), \tag{7.14}$$

where A_0^2 stands for the initial intensity in $\mathrm{W/m^2}$, a_0 is the initial radius of the beam and $a(z)$ is the evolution of the beam radius, which is the solution of the following equation (overdots stand for the z derivative):

$$\ddot{a} + g_0 a + \frac{C}{a^3} = 0 \quad , \quad C \equiv \left(\frac{n_2 a_0^2 A_0^2}{2n_0} - \frac{1}{\beta_0^2}\right). \tag{7.15}$$

From Eq. (7.14), we can see that $a(z)$ is enough to describe the whole beam intensity dynamics. Equation (7.15) has analytic solution, and for the initial conditions $a(0) = a_0$ and $\dot{a}(0) = 0$ it is written as:

$$a^2(z) = a_0^2(\cos^2(\sqrt{g_0}z) + \mathcal{C}\sin^2(\sqrt{g_0}z)), \tag{7.16}$$

where $\mathcal{C} = (1-\mathcal{P})/(\beta_0^2 a_0^4 g_0) = -C/(g_0 a_0^4)$ and $\mathcal{P} = n_2\beta_0^2 A_0^2 a_0^2/(2n_0)$ is a dimensionless parameter related to beam collapse [193], [195]. For high enough values of power ($\mathcal{P} > 1$), $\mathcal{C}$ becomes negative and thus $a(z)$ is complex, which translates to the collapse of the beam. Therefore, including nonlinearity introduces an upper limit of the initial injected power. Nevertheless, we will consider intensities which are far below this limit. The period of $a(z)$ is the same as the self-imaging pattern that was obtained in section 1.5.2, which is $\xi = \pi/\sqrt{g_0}$, and it does not depend on the intensity.

Note also that, when $\mathcal{C} = 1$, the beam does not experience self-imaging because

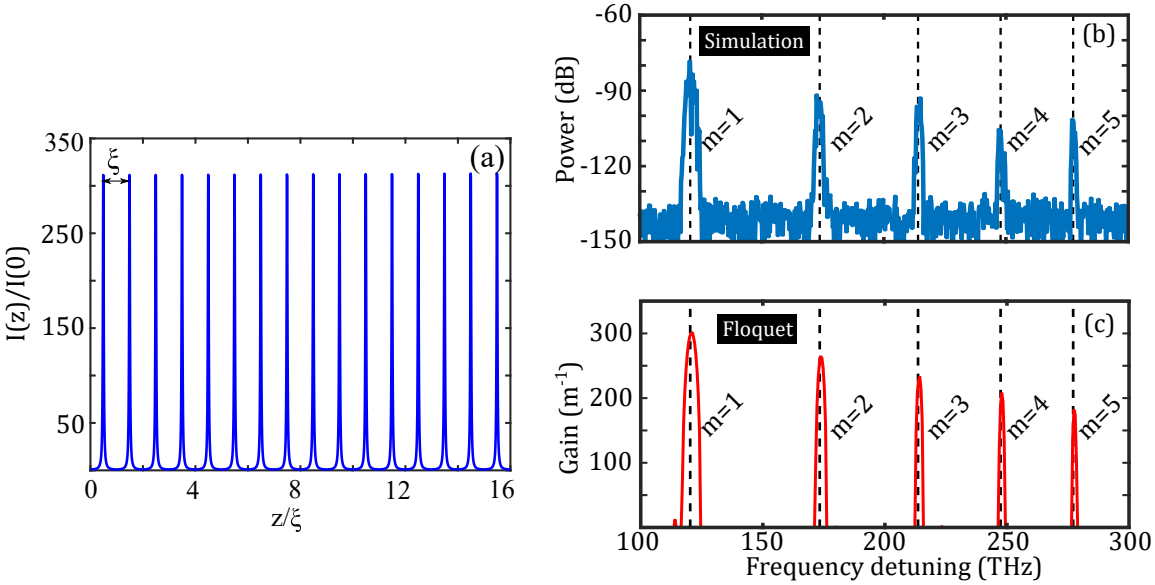

Figure 7.1: (a) Evolution of the intensity at the core center obtained in the stationary limit of Eq. (7.10). (b) Output spectrum obtained by numerically solving Eq. (7.10). Black dashed lines correspond to the central frequencies predicted by Eq. (7.23). (c) Floquet spectrum obtained from Eq. (7.20). The parameters are:$n_0 = 1.47$, $n_2 = 3.2 \cdot 10^{-20}$ m^2/W, $r_{core} = 26$ μm, $\Delta = 8.8 \cdot 10^{-3}$, λ_0 =1064 nm, $A_0^2 = 20$ GW/cm^2, $a_0 = 20$ μm, and fiber length 2.2 cm.

$a^2(z) = a_0^2$. In the linear propagation regime (i.e. $A_0 \to 0$), it corresponds to the limit where $a_0 = (r_{core})/(2\beta_0^2 R^2 \Delta)^{1/4}$, which is the radius of the fundamental mode reported in [66] and in subsection 1.5.2.

In Fig. 7.1 (a), an example of numerical solution of Eq. (7.13) is shown. The represented quantity corresponds to the intensity at the center of the fiber ($I(z) = |E(z, x = 0, y = 0)|^2$), normalized to the initial intensity. Fiber length has been normalized to the self-imaging period, which corresponds to $\xi \approx 600$ μm. Employed parameters are displayed in Figure's caption.

7.3.2 Spectrum of GPI of a constant core fiber

Having described the spatial behavior of light, we now include the time coordinate in order to find out which frequencies are unstable. In this section, as commonly done in the literature, we assume that the waveguide refractive index does not depend on the frequency. We follow a slightly different approach from the original one developed by S. Longhi [169].

We assume a spatiotemporal field of the form:

$$\mathcal{E} = (1 + \delta E(t,z))E_s(x,y,z), \tag{7.17}$$

where $E_s(x,y,z)$ is the approximated spatial field from Eq. (7.14) and $\delta E(z,t)$ is a small perturbation homogeneous in the transverse plane. By substituting this *ansatz* in the GNLSE, it can be readily found that:

$$iE_s\partial_z\delta E = E_s D(i\partial_T)\delta E + \chi|E_s|^2 E_s(\delta E + \delta E^*). \tag{7.18}$$

Equation (7.18) depends on the transverse coordinates (x,y), but the number of dimensions can be reduced by projecting over the field E_s. Then by multiplying Eq. (7.18) by E_S^* and after integrating over (x,y), we get:

$$i\partial_z\delta E = D(i\partial_T)\delta E + \frac{\chi A_0^2 a_0^2}{2a^2(z)}(\delta E + \delta E^*). \tag{7.19}$$

An important remark is that this equation is very similar to the one obtained for the one dimensional case with a harmonically varying nonlinearity in section 3.3. Indeed, Eq. (7.19) allows us to physically understand GPI. The periodic intensity of the beam produces a z-dependent effective nonlinearity, which triggers MI as we have shown in chapter 3. As we did in there, the field δE is expressed as $\delta E = a(z)e^{i\Omega t} + b^*(z)e^{-i\Omega t}$ and following the same steps depicted in Chapter 3, we obtain:

$$\ddot{\eta} + D_{even}(\Omega)\left(D_{even}(\Omega) + 2F(z)\right)\eta = 0, \tag{7.20}$$

where $F(z) = \chi A_0^2 a_0^2/2/a^2(z)$ and $\eta = a + b$. The function $F(z)$ has a period ξ. Thus, expression (7.20) is a Hill's equation whose resonances verify:

$$D_{even}(\Omega)\left(D_{even}(\Omega) + 2F_{av}\right)) = \left(\frac{m\pi}{\xi}\right)^2, \tag{7.21}$$

m being an integer number and F_{av} the average value of $F(z)$ over one period and which is calculated as:

$$F_{av} = \frac{1}{\xi}\int_0^\xi F(z)dz = \frac{\chi A_0^2}{2\sqrt{\mathcal{C}}}. \tag{7.22}$$

If we consider dispersion up to second order, the central frequencies of GPI bands are

located at the following frequencies:

$$\Omega_m^2 = \frac{2}{\beta_2}\left(-F_{av} + \sqrt{F_{av}^2 + g_0 m^2}\right). \tag{7.23}$$

where m is an integer number. Note that, at the low intensity limit (i.e. $F_{av} \to 0$), $\Omega^2 \approx 2m/(\beta_2\zeta)$, which is the relation used in reference [69] to predict the GPI generated frequencies. As we discussed in Chapter 3 when dispersion over second order is disregarded, there is an infinite set of Ω_m which can verify Eq. (7.23).

Figure 7.1 shows a comparative between numerical simulations (b) and Floquet analysis (c). Numerical simulations have been obtained by directly solving Eq. (7.7) using a CW perturbed by a weak random noise. The propagation length corresponds to a 2.2 cm long fiber. Gain presented in Fig. 7.1 (c) has been obtained by means of Floquet theory, depicted in section 3.3.2. Vertical dashed lines correspond to the central frequencies predicted by Eq. (7.23). Predictions of bandwidth and position of the bands found by Floquet theory are in very good agreement with numerical simulations from GNLSE.

Summary

- We have described the model that we use to describe light propagation in multimode fibers. We have explained which are the necessary approximations and we have discussed their limits. The model is a GNLSE where the waveguide dispersion has been neglected.

- To solve GNLSE, we take advantage of the cylindrical symmetry of the fiber. Besides, we consider that light excitation is centered. These hypothesis allow us to suppose the propagation to have a circular symmetry. Then, to numerically integrate GNLSE we use a split-step method with a Hankel transform of order zero implemented.

- We described GPI in a constant core fiber. We analyzed at first the spatial behavior of light (stationary limit) and after we included the time coordinate. We employed quasi-phase-matching arguments and Floquet analysis to predict the bandwidth and frequency of instability regions. This analysis showed a good agreement with numerical simulations.

CHAPTER

EIGHT

GPI IN A PERIODICALLY MODULATED GRIN FIBER

Contents

Up to now, we have considered fibers with a constant core diameter. Within this situation, light propagating in a GRIN fiber exhibited a periodic behavior (self-imaging), inducing then a periodic evolution of the effective refractive index and, as a consequence, the production of new spectral bands via GPI [196]. In this chapter, we will consider fibers with varying core. A sketch of the fibers under consideration is shown in Fig. 8.1 (a). The effect of periodically varying the core will be to change the overall spatial pattern and as a result, new characteristic spectral bands will arise. Then the precise knowledge of the spatial evolution of light becomes a central point to determine the output spectrum, as it was the case when a fiber with constant core was studied. We have found an analytic approximation of the spatial profile of the beam under two different limits depending on the relation between the modulation period and the self-imaging distance. These approximations are described in Sec. 8.1. The first one, happens when the modulation period is close to the self-imaging distance ξ. In this case, we observe a "Moiré-like" effect, where a longer period modulates the self-imaging pattern. The second one, consists in a modulation period much longer than the self-imaging distance, which results into an adiabatic modulation pattern. After the spatial behavior is characterized, the temporal coordinate is included and the effects of the modulation over the GPI spectrum

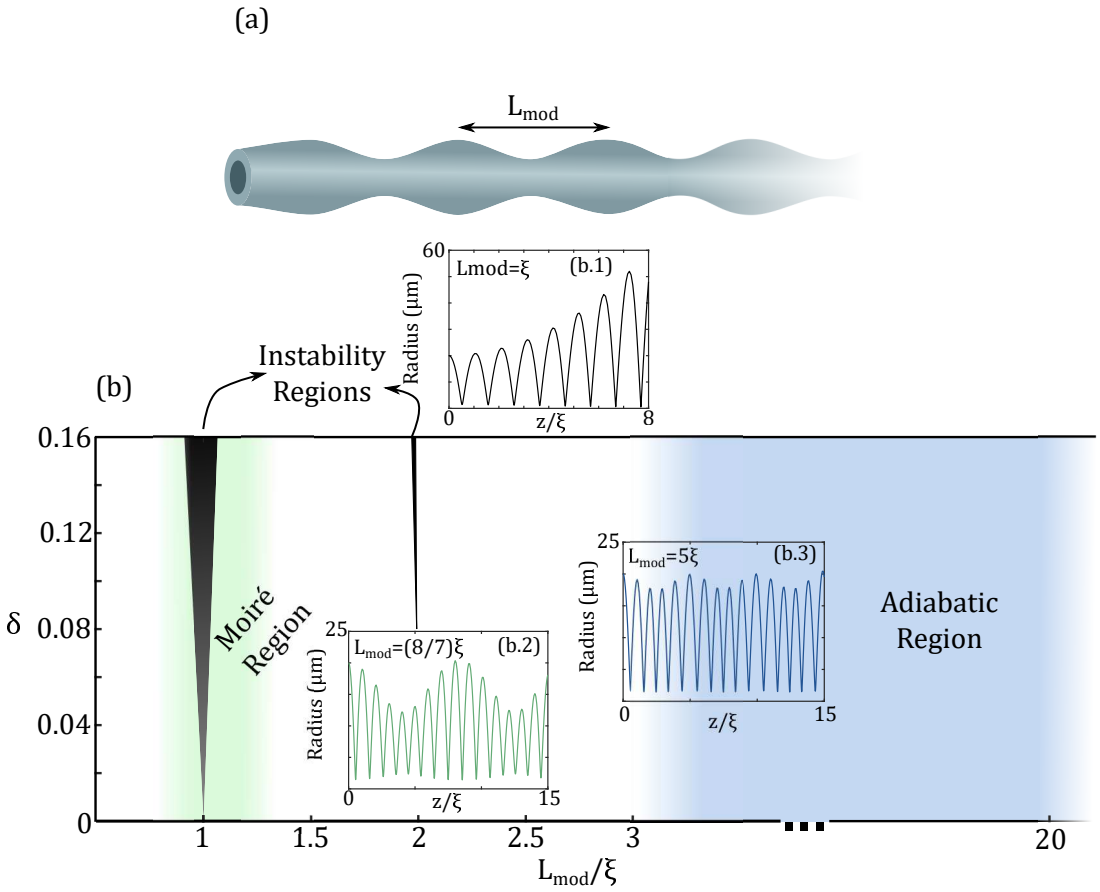

Figure 8.1: Fig. (a) Sketch of a harmonically modulated fiber with period L_{mod}. Fig(b) Floquet map displaying the different different behaviors of Eq. (8.3) as a function of L_{mod}/ξ and δ.

are characterized in section 8.2.

8.1 Spatial dynamics of light in a modulated GRIN fiber

In section 7.3.1, the spatial dynamics of light in a constant core fiber was studied. We found that the evolution of the beam was periodic and it could be obtained in a closed form. In the present section, we analyze the spatial evolution of light in a varying core fiber. The evolution of a Gaussian beam (see Eq. (7.14)) can be obtained by means of the moments method [197]. The whole dynamics of the beam intensity is described by its radius $a(z)$,

whose evolution is given by the following equation:

$$\ddot{a} + g(z)a + \frac{C}{a^3} = 0, \tag{8.1}$$

where $g(z) = 2\Delta/r_{core}^2(z)$, being $r_{core}^2(z)$ the radius of the core. Expression (8.1) is a singular Ermakov equation, whose solutions can be generally found within the form [198], [199]:

$$a(z) = \sqrt{u^2(z) - \frac{Cv^2(z)}{W^2}} \tag{8.2}$$

where $u(z)$ and $v(z)$ are two linearly-independent solutions of the equation:

$$\ddot{x} + g(z)x = 0, \tag{8.3}$$

and W stands for the Wroskian $W = u\dot{v} - \dot{u}v \neq$const. The initial conditions for $u(z)$ and $v(z)$ are $u(0) = a_0$, $\dot{u}(0) = \dot{a}(0)$ and $v(0) = 0$, $\dot{v}(0) \neq 0$ respectively. We shall restrict to a periodic evolution of the radius core r_{core}, which we express in the following form: $r_{core} = r_0(1 + \delta\cos(k_{mod}z))$, where $k_{mod} = 2\pi/L_{mod}$, being L_{mod} the modulation period and δ its depth. Given the fact that $g(z)$ is periodic, this function can be expressed as a Fourier series, then Eq. (8.3) read as:

$$\ddot{x} + \left(g_0 + \sum_{m=1}^{\infty} \alpha_m \cos\left(mk_{mod}z\right) + \beta_m \sin\left(mk_{mod}z\right)\right) x = 0, \tag{8.4}$$

where $g_0 = 2\Delta/r_0^2$, r_0 being the average value of the radius. Coefficients α_m and β_m are the respective coefficients of the Fourier development. From g_0 we can define a self-imaging distance ξ, which would correspond to the self-imaging period of a non-modulated fiber. Expression (8.4) is a Hill's equation and, as we have already discussed in section 3.3, this equation has parameter regions where its solutions are unstable, i.e. they increase exponentially with z. These regions are called Arnold Tongues and their tips verify that the natural frequency of the equation ($\sqrt{g_0}$) is a multiple of half the frequency of variation $\sqrt{g_0} = mk_{mod}/2$, which translates to the following condition over the self imaging-distance: $L_{mod} = m\xi$. In Fig. 8.1 (b.1), the evolution of $a(z)$ calculated using Eq. (8.1) with $L_{mod} = \xi$ is shown. Outside these regions, solutions of Eq. (8.2) behave in periodic (or quasiperiodic) manner. Moreover, even if the condition $L_{mod} = m\xi$ is satisfied, there is a threshold on the modulation depth δ for the emergence of parametric instability, which in general increases for higher-order resonances. Parameter regions exhibiting a spatially unstable behavior

will be avoided, since our final objective is to study how the GPI spectrum is modified by the core modulation, and if the spatial evolution is not periodic or quasi-periodic, there will not be GPI.

Within the stable regions, we distinguish three different regimes as a function of the ratio L_{mod}/ξ: $L_{mod} \ll \xi$, $L_{mod} \approx \xi$ and $L_{mod} \gg \xi$. The first case is the least interesting, since core variations are averaged and the uniform fiber is recovered. The case where the self-imaging distance is close to the modulation period ($L_{mod} \approx \xi$) will be refered as Moiré-like pattern. In Fig. 8.1 (b.2) the evolution of the radius of a Gaussian beam with $L_{mod} = (8/7)\xi$ calculated using Eq. (8.1) is displayed. Finally, the regime where the modulation period contains several self-imaging distances will be called adiabatic. Figure 8.1 (b.3) displays the evolution of the beam radius in a modulated fiber with $L_{mod} = 5\xi$ calculated using Eq. (8.1).

In figure 8.1(b) a sketch of the different regimes of $a(z)$ is displayed. This graphic is a Floquet analysis of equation (8.3) as a function of L_{mod} and δ, and it has been obtained following the numerical recipe for finding Floquet exponents described in section 3.3.2. In this sketch, Arnold tongues are the black-shadowed regions and arise from $L_{mod} = \xi$ and $L_{mod} = 2\xi$. The tongue corresponding to $L_{mod} = 3\xi$ does not appear because the modulation depth is not big enough and the instability threshold is not overcome. The case where $L_{mod} \approx \xi$ is in the vicinity of the first Arnold Tongue is green colored, while the adiabatic regime ($L_{mod} \gg \xi$) is painted in blue.

8.1.1 Period of modulation close to self-imaging period

When modulation period has a length close to ξ, self-imaging is modulated by a long range envelope, reminiscent of a Moiré effect produced by the beating of two spatial frequencies. We associate them to the intrinsic oscillations of light in a GRIN fiber and the modulation period. Considering the depth of modulation to be small enough to avoid spatial instabilities, an accurate approximation of the evolution of $a(z)$ can be found analytically. Expanding up to second order the term $1/r_{core}(z)$, equation (8.3) read as:

$$\ddot{x} + \frac{2\Delta}{r_0^2}(1 - 2\delta\cos(k_{mod}z) + 3\delta^2\cos^2(k_{mod}z))x = 0. \tag{8.5}$$

Two independent solutions are needed for completely solving Eq. (8.5). The solutions can be obtained by multi-scale techniques [124]. By defining the dimensionless coefficients:

$w = \sqrt{2\Delta}/r_{core}/k_{mod}$, $\epsilon = w^2\delta$ and $\bar{z} = k_{mod}z$, the following equation is found:

$$\ddot{x} + \left(w^2 - 2\epsilon\cos(\bar{z}) + \frac{3\epsilon^2}{w^2}\cos^2(\bar{z})\right)x = 0. \tag{8.6}$$

Since we are assuming $L_{mod} \approx \xi$, the parameter $w \approx 1$, so that a multi-scale analysis up to first order can be safely performed. Then, by following the standard procedure of defining $\bar{z}_n = \epsilon^n\bar{z}$ and $x = \sum_{n=0}\epsilon^n x_n$ and splitting in different equations powers of ϵ, an infinite set of equations is obtained. In this infinite system, the function x_1 can be found by keeping terms up to order ϵ^2:

$$\epsilon^0: \quad (D_0^2 + w^2)x_0 = 0, \tag{8.7}$$

$$\epsilon^1: \quad (D_0^2 + w^2)x_1 = -2(D_1D_0 - \cos(\bar{z}_0))x_0, \tag{8.8}$$

$$\epsilon^2: \quad (D_0^2 + w^2)x_2 = -2(D_1D_0 - \cos(\bar{z}_0))x_1 - \left(2D_2D_0 + D_1^2 + \frac{3}{2w^3}\cos(\bar{z}_0)\right)x_0, \tag{8.9}$$

where $D_n = \partial_{\bar{z}_n}$. The solution corresponding to order zero in ϵ is:

$$x_0 = A(\bar{z}_1, \bar{z}_2)e^{iwz} + A^*(\bar{z}_1, \bar{z}_2)e^{-iwz}, \tag{8.10}$$

where $A(\bar{z}_1, \bar{z}_2)$ is a complex function. This solution has to be substituted in Eq. (8.8) and the term $D_1D_0x_0$ must be imposed to vanish. The reason why this condition is needed is because $D_1D_0x_0$ oscillates at the natural frequency of the system (w), then in order to construct bounded solutions, this term must vanish. In the literature, terms which lead to resonances are referred as secular. Taking into account this assumption and solving Eq. (8.8), the following expression is obtained:

$$x_1 = A(\bar{z}_2)\left(\frac{-e^{i(w+1)\bar{z}_0}}{2w+1} + \frac{e^{i(w-1)\bar{z}_0}}{2w-1}\right) + c.c, \tag{8.11}$$

where $c.c$. denotes complex conjugate. Finally, x_1 is introduced in equation (8.9) and by imposing again secular terms to vanish we get:

$$A = \frac{C}{2}e^{i(\phi\bar{z}_2+\beta)} \quad , \quad \phi = \frac{8w^2-3}{4w^3(4w^2-1)}, \tag{8.12}$$

being C and β two real constants depending on the boundary conditions. By merging the results of x_0 and x_1 the following equation is found:

$$x = C\left[\cos(\tilde{w}z+\beta)+\epsilon\left(\frac{\cos((\tilde{w}-1)z+\beta)}{2w-1}-\frac{\cos((\tilde{w}+1)z+\beta)}{2w+1}\right)\right]+O(\epsilon^2), \quad (8.13)$$
$$\tilde{w} = w\left(1+\frac{\delta^2(8\omega^2-3)}{4(4\omega^2-1)}\right).$$

Functions $u(z)$ and $v(z)$ are obtained by imposing their corresponding boundary conditions:

$$u(z) = \frac{(4g_0-k^2)a_0}{(4+2\delta)g_0-k^2}\left(\cos(\sqrt{g_0}\sigma z)+\frac{\delta g_0}{k}\left(\frac{\cos((\sqrt{g_0}\sigma-k)z)}{2\sqrt{g_0}-k}-\frac{\cos((\sqrt{g_0}\sigma+k)z)}{2\sqrt{g_0}+k}\right)\right), \quad (8.14)$$

$$v(z) = -B\left(\sin(\sqrt{g_0}\sigma z)+\frac{\delta g_0}{k}\left(\frac{\sin((\sqrt{g_0}\sigma-k)z)}{2\sqrt{g_0}-k}-\frac{\sin((\sqrt{g_0}\sigma+k)z)}{2\sqrt{g_0}+k}\right)\right), \quad (8.15)$$

where,

$$W = -B\frac{(4g_0-k^2)a_0}{(4+2\delta)g_0-k^2}\sqrt{g_0}\sigma, \quad (8.16)$$

$$\sigma = 1+\frac{\delta^2(8g_0-3k^2)}{4(4g_0-k^2)}. \quad (8.17)$$

Equations $u(z)$ and $v(z)$ give the evolution of the beam radius through the expression (8.2). In figure 8.2.(a), a comparative between the numerical solution of Eq. (8.1) and the analytic solutions obtained Eqs. (8.14)-(8.17). The represented quantity is the intensity of the beam at the core center normalized to its initial value.

The functions $u(z)$ and $v(z)$ are combinations of trigonometric functions whose periods are not necessarily commensurate, therefore $a(z)$ has a quasi-periodic evolution. However, for δ small enough, the assumption of $\sigma \approx 1$ can be safely adopted. Within this limit, $a(z)$ is described as a combination of functions with period L_{mod} or ξ. If L_{mod} and ξ are chosen in such a way that they are commensurate, then the beam will evolve periodically but with a longer period $L = p\xi = qL_{mod}$, being p and q two integer numbers. This result evokes a Moiré pattern, because a superposition of two periodic functions with two similar frequencies gives birth to a new function but with a longer period. When ξ and L_{mod} are not commensurate, we will always be able to find a p and q which approximate with a good degree of precision the actual quasi-periodic behavior of $a(z)$. The fact that periods

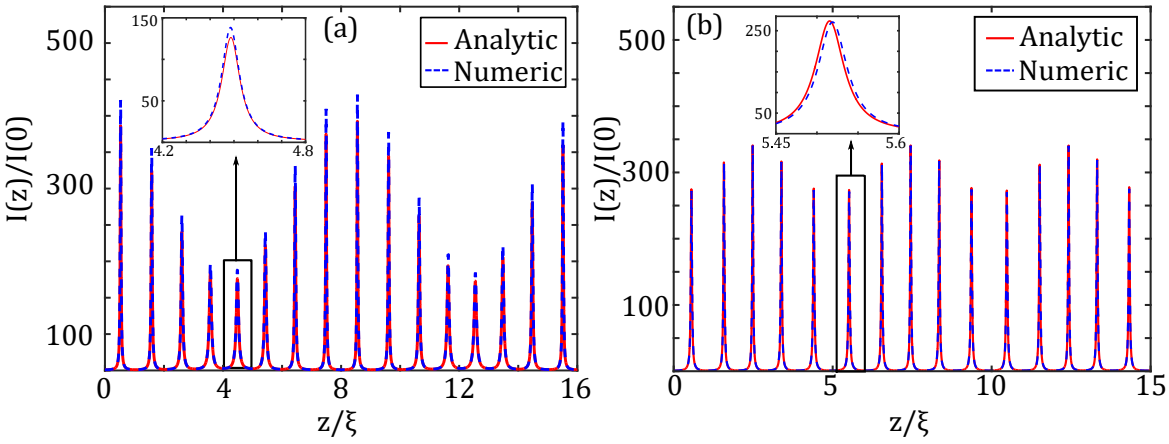

Figure 8.2: Evolution of the intensity at core center calculated from numerical solution of Eq. (7.15) (blue dashed line) and obtained analytic solutions (red solid line). Fig. (a) Moiré with $L_{mod} = (8/7)\xi$, Fig. (b) adiabatic with $L_{mod} = 5\xi$.

are not commensurate will not affect qualitatively the output spectrum, as will be shown later.

8.1.2 Adiabatic modulation of the core

When L_{mod} is much longer than ξ, then the aforementioned parameter ϵ will become bigger and multi-scale development will not converge to the actual evolution of $a(z)$. To overcome this problem, the Wentzel-Kramers-Brillouin (WKB) approximation is employed [124]. Our starting point is Eq. (8.3) after performing the change of variables $\bar{z} = kz$:

$$k^2\ddot{x} + g(\bar{z})x = 0. \tag{8.18}$$

By using the WKB approximation, x can be estimated as:

$$x = \sqrt[4]{g(\bar{z})}\left(C_1 \exp\left(\frac{i}{k}\int_0^{\bar{z}} d\bar{z}'\sqrt{g(\bar{z}')}\right) + C_2 \exp\left(-\frac{i}{k}\int_0^{\bar{z}} d\bar{z}'\sqrt{g(\bar{z}')}\right)\right), \tag{8.19}$$

where C_1 and C_2 are two constants depending of the boundary conditions. Then, if the appropriate conditions are imposed, $a(z)$ is found as:

$$a(z) = \sqrt{a_0^2\sqrt{\frac{g(0)}{g(z)}}\cos^2(\phi(z)) - \frac{C}{a_0^2\sqrt{g(0)g(z)}}\sin^2(\phi(z))}, \tag{8.20}$$

where the phase $\phi(z) = \int_0^z dz' \sqrt{g(z')}$ can be analytically obtained and reads as:

$$\phi(z) = \frac{2\sqrt{g_0}}{k\sqrt{1-\delta^2}} \left(\tan^{-1} \left[\sqrt{\frac{1-\delta}{1+\delta}} \tan\left(\frac{kz}{2}\right) \right] + \pi m \right), m = \left\lfloor \frac{z}{L_{mod}} + \frac{1}{2} \right\rfloor, \tag{8.21}$$

In Fig. 8.2 (b), a comparison between the numerical solution of $a(z)$ obtained from Eq. (7.15) and the obtained result with $L_{mod} = 5\xi$ is displayed. We see that there is a remarkable agreement between the two results. If the limit $\delta \to 0$ is considered, $a(z)$ can also be expressed as a combination of trigonometric functions with period L_{mod} and ξ. Hence if both periods are commensurate, $a(z)$ will have a period $L = pL_{mod} = q\xi$, like in the case where $L_{mod} \approx \xi$. Strictly speaking, $\delta \neq 0$ thus $a(z)$ will evolve in a quasi - periodic fashion, nevertheless this behavior can always be approximated to be periodic, as discussed in the case where $L_{mod} \approx \xi$.

8.2 Effects of modulation on the spectrum

As we have previously shown, a periodic modulation of the core produces a more complex spatial evolution of the beam. In this section we will show that, the bigger richness of the spatial behavior traduces in the appearance of new spectral lines, the central frequency and gain of which are found by following the same arguments formerly employed to describe GPI in a constant core fiber.

For the shake of simplicity, we will consider periods L_{mod} and ξ to be commensurate, i.e. $qL_{mod} = p\xi$. Then, perturbations are ruled by a modified equation (7.20), where now $F(z)$ has a period L instead of ξ. Thus the central frequency of GPI bands is given by the expression:

$$\frac{\beta_2\Omega^2}{2}\left(\frac{\beta_2\Omega^2}{2} + 2F_{av}\right) = \left(m\,\frac{\pi}{L}\right)^2, \tag{8.22}$$

where we have considered that F_{av} can be approximated by the F_{av} of a constant fiber. Note that the only difference between the PR condition found in the modulated case Eq. (8.22) and the constant core case Eq. (7.21) is the period appearing on the right hand side of the equation. Hence, the position of instability bands will be given by the following expression:

$$\Omega_m^2 = \frac{2}{\beta_2}\left[-F_{av} + \sqrt{F_{av}^2 + \frac{\pi^2 m^2}{L^2}}\right]. \tag{8.23}$$

The resulting spatial dynamics can be considered to have a period $L = qL_{mod} = p\xi$, thus

band position can be related to ξ as follows:

$$\Omega_m^2 = \frac{2}{\beta_2}\left[-F_{av} + \sqrt{F_{av}^2 + \frac{g_0 m^2}{p^2}}\right]. \tag{8.24}$$

Notice that, when m is an integer multiple of p, we recover the resonances of the constant core fiber. Therefore it is advantageous to write $m = m_1 p + m_2$, which leads to the following expression of the central frequencies:

$$\Omega_{m_1,m_2}^2 = \frac{2}{\beta_2}\left[-F_{av} + \sqrt{F_{av}^2 + g_0\left(m_1 + \frac{m_2}{p}\right)^2}\right]. \tag{8.25}$$

The number m_1 ($m_1 \neq 0, m_2 = 0$) accounts for the principal bands of PR, which corresponds to the same resonances given by a constant core fiber. The number m_2 ($m_1 \neq 0, m_2 \neq 0$) corresponds to the secondary resonances. These instability bands are a direct consequence of the modulation of the fiber. We consider that each secondary band is associated to a principal band, therefore to avoid any ambiguity in band position, the values of m_2 must be restricted to the following intervals, for p even:

$$p = 2n \Rightarrow \begin{cases} -n+1 \leq m_2 \leq n, & m_1 \neq 0, \\ 1 \leq m_2 \leq n, & m_1 = 0, \end{cases} \tag{8.26}$$

and for p odd as:

$$p = 2n+1 \Rightarrow \begin{cases} -n \leq m_2 \leq n, & m_1 \neq 0, \\ 1 \leq m_2 \leq n, & m_1 = 0. \end{cases} \tag{8.27}$$

Physically, the splitting of bands is associated to a doubly periodic behavior, i.e. the intrinsic periodicity of light in GRIN fibers and the additional modulation of the core. The splitting of bands due to a doubly periodic behavior of light has been also studied in the case of a dispersion modulated PCF [200].

In Fig. 8.3(a) the output spectrum of a numerical simulation of a periodically modulated fiber is reported. Dashed lines correspond to the frequencies predicted by Eq. (8.25). The amplitude of modulation is shallow and is $\delta = 0.12$. Modulation period belongs to the Moiré-like regime and is $L_{mod} = 8/7\xi$. The fiber length is 3 cm and parameters are displayed in figure's caption. The spatial evolution of the beam was plotted in Fig. 8.2(a). This example shows clearly the splitting of bands associated to a modulated fiber. The output spectrum is composed by three principal bands and, in their vicinity, there are some

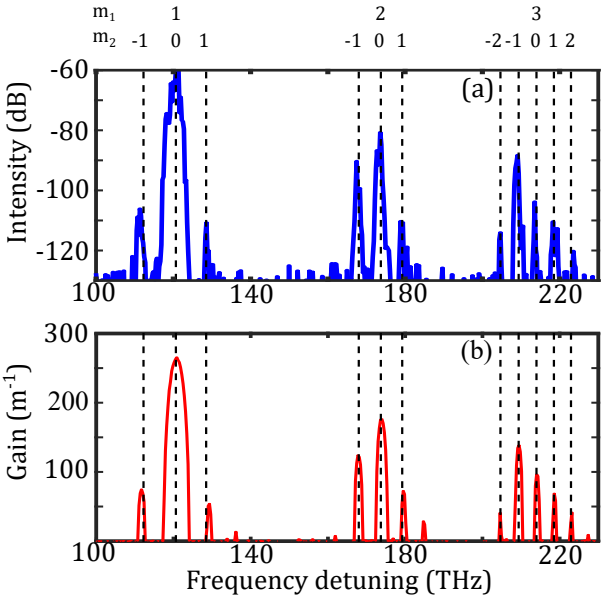

Figure 8.3: (a) Output spectrum obtained by solving numerically GNLSE (7.10). Black dashed lines corresponds to unstable frequencies obtained from Eq. (8.25). (b) Floquet spectrum obtained from Eq. (7.20). Parameters: $\delta = 0.12$, $L_{mod} = (8/7)\xi$, $A_0^2 = 20\,\mathrm{GW/cm^2}$ and fiber length 3 cm.

secondary bands. The agreement between central frequencies predicted by the theory and their actual position in numerical simulations is excellent.

The width and position of bands can also be predicted by Floquet analysis, as we described in chapter 7. In Fig. 8.3(b), the corresponding Floquet map is shown. We recall that this analysis can be performed using Eq. (7.20). However, now $a(z)$ has been obtained using expressions Eqs. (8.14-8.15). The agreement between numerical simulations and Floquet analysis is remarkable.

It is interesting to study how the position and width of generated bands change as a function of L_{mod}/ξ. In Fig. 8.4 (a) we extend the Floquet analysis presented in Fig (8.3) (b) to more values of L_{mod}/ξ within the regime $L_{mod} \approx \xi$. Modulation periods L_{mod} have been chosen to be commensurate and verify $L_{mod} = (n+16)\xi/(n+12)$, being n an integer number running from 0 to 20. Therefore, the period L will verify $L = (n+16)\xi$. Dashed lines represent the frequencies predicted by Eq. (8.25). We see that the position of principal bands do not change and they split in secondary bands, whose frequency gets further from principal bands when the ratio L_{mod}/ξ is increased. Secondary bands are found at $m_2 = \pm 4$ because from the definition of the modulation period, each value of n generates

an overall period L composed of four slow oscillations. Both Floquet map and predicted frequencies show a good agreement.

The second case corresponds to modulation periods which are longer than self-imaging distances, and the spatial behavior corresponds to the adiabatic limit studied in section 8.1. In order to obtain commensurate periods, L_{mod} is chosen to verify $L_{mod} = (12+n)\xi/4$, where n is an integer ranging from 0 to 64. The corresponding overall period is $L_{mod} = (n+12)\xi$. In Fig. 8.4 (b) the Floquet map is shown. Here we see two principal bands which split in some secondary bands. For the smallest modulation period, only two secondary bands appear for each band with $m_2 = \pm 4$. When L_{mod} is increased, then secondary bands get closer to the principal bands and in addition, new bands with different values of m_2 appear. Finally, at the highest considered values of L_{mod}/ξ, bands cluster around the principal ones.

In order to give support to Floquet maps, some numerical simulations have been carried out. Results are plotted in Fig. 8.4 (c) and (d). To get rid of any randomness which would hinder the comparison, the initial noise has been implemented as a coherent seed (in form of a 1 fs sech with an intensity 10^{-5} weaker than the initial CW pump) to the initial CW. We can see that there is a good agreement between the results obtained by direct integration of the equation and Floquet analysis. The choice of L_{mod} is equispaced, regardless whether periods are commensurate or not. This implies there are not quantitative changes in the output spectrum between a periodic or quasi-periodic behavior.

We have shown that the periodic modulation of GRIN fibers modifies the GPI spectrum adding new spectral bands. We have developed a theory able to predict frequency and bandwidth of the instability bands. In our simulations, we have used realistic parameters, which provides a solid evidence that the described effects can be observed experimentally. From the application point of view, the generation of multiple GPI sidebands in periodically modulated GRIN fibers can be exploited to optimize the spectral extent and/or the spectral power density of high power supercontinuum sources based on highly multimode fibers.

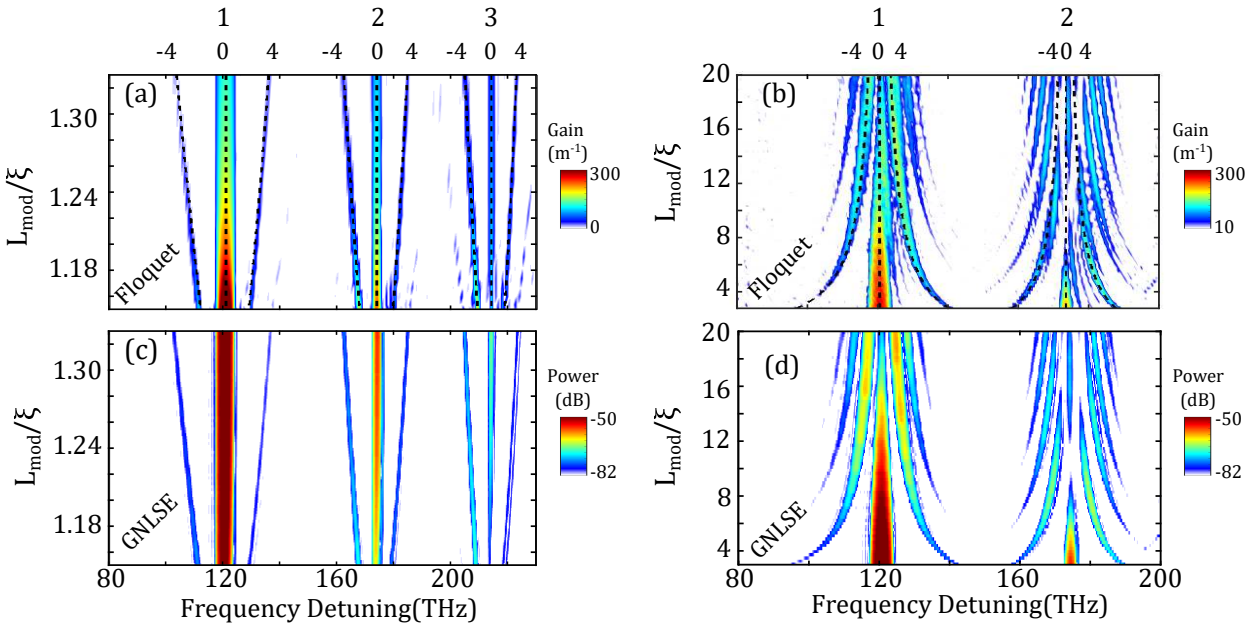

Figure 8.4: (a) and (b) Gain map obtained with numerical Floquet analysis as a function of the ratio L_{mod}/ξ for (a)$L_{mod} \approx \xi$ and (b)$L_{mod} \gg \xi$. (c) and (d) Direct numerical integration of Eq. (7.10) for (c) $L_{mod} \approx \xi$ and (d) $L_{mod} \gg \xi$. The parameters are $\beta_2 = 16.55 \cdot 10^{-27}$ s^2/m, $a_0 = 20$ μm, $r_{core} = 26$ μm, and A_0= 20 GW/cm^2.

Summary

- We have analyzed the spatial evolution of light in a periodically modulated fiber. The parameter regions (L_{mod}, δ) where the beam does not experience a stable behavior have been identified. In addition, we have defined three different regimes of bounded evolution of light, being the most remarkable when $L_{mod} \approx \xi$ and $L_{mod} \gg \xi$. Moreover, we have found an analytic approximation to describe beam evolution in both limits.

- The effects over the GPI spectrum of the fiber modulation have been investigated. We have shown that the double periodicity present in the system results in the splitting of GPI bands. Bandwidth and central frequency of unstable regions can be predicted by means of Floquet analysis and phase-matching arguments respectively. Our theoretical approach presented a good agreement with numerical simulations.

CHAPTER

NINE

FAST AND ACCURATE MODELING OF MULTIMODE DYNAMICS

Contents

In chapter 7, we found that light propagation in a GRIN fiber can be seen as light traveling in a medium with varying nonlinearity. Using this result, we obtained the gain of GPI bands. In the present chapter, we generalize this result and find an equivalent (1+1)D GNLSE that mimics the whole spatio-temporal dynamics present in (3+1)D GNLSE equation [68]. This result allows to reduce a 3+1 dimensional model to an equivalent one with 1+1 dimensions. Within this simplification, the obtained advantages are twofold. Theoretical analysis of the different possible phenomena will become much simpler, and the needed computational time for solving the equation will be drastically shortened. The chapter is organized as follows: in section 9.1, the modified (1+1)D GNLSE is derived from the (3+1)D GNLSE. In section 9.2, propagation of CW is analyzed and finally, in section 9.3, femtosecond pulse propagation in a GRIN fiber is studied.

9.1 Derivation of an equivalent (1+1)D NLSE equation

The starting point of our derivation is (3+1) D GNLSE:

$$i\partial_z\mathcal{E} + \frac{1}{2\beta_0}\nabla_\perp^2\mathcal{E} + \beta(i\partial_T)\mathcal{E} - \frac{\beta_0 g(z)}{2}r^2\mathcal{E} + \chi f_{NL}(\mathcal{E}) = 0, \tag{9.1}$$

where $g(z) = 2\Delta/r_{core}^2(z)$ and f_{NL} the nonlinear response given in Eq. (7.6). We consider a perfect waveguide, the beam injection is assumed to be centered and with spatial Gaussian shape. The beam experiences a perfect self-imaging pattern with period ξ and we consider intensities which are far below the beam-collapse. The field $\mathcal{E}$ is supposed to verify the following *ansatz*:

$$\mathcal{E}(x,y,z,t) = F_s(x,y,z)A(z,t), \tag{9.2}$$

where $F_s(x,y,z)$ is the field distribution in the transverse to propagation plane and $A(z,t)$ is a temporal envelope homogeneous in the plane (x,y) depending on z and t. By inserting the *ansatz* in equation (9.1), the following expression is obtained:

$$A\left[i\partial_z F_s + \frac{1}{2\beta_0}\nabla_\perp^2 F_s - \frac{\beta_0 g(z)}{2}r^2 F_s\right] + F_s\left[i\partial_z A + D(i\partial_t)A + \chi|F_s|^2 f_{NL}(A)\right] = 0. \tag{9.3}$$

Function F_s is chosen in such a way that the first term of Eq. (9.3) vanishes. We assume then F_s to verify $|F_s| = \frac{1}{\sqrt{\pi}a(z)}\exp\left(-\frac{r^2}{2a(z)^2}\right)$, where $a(z)$ evolution is given by Eq. (7.15) if the core is constant, while if $g(z) \neq const.$ is described by Eq. (8.1). Note that, when $g(z)$ is constant, $F(z)$ will be an exact solution, whereas if the core size changes with z the supposed spatial behavior is an approximation. By multiplying by F_s^* and integrating over (x,y) Eq. (9.3), we obtain the following equation for $A(z,t)$:

$$i\partial_z A + D(i\partial_T)A + \gamma(z)f_{NL}(A) = 0 \quad , \quad \gamma(z) = \frac{n_2\omega_0}{cA_{eff}(z)} = \frac{n_2\omega_0}{2c\pi a^2(z)}, \tag{9.4}$$

where $A_{eff}(z) = 2\pi a^2(z)$ is an effective area which is calculated using the standard definition $A_{eff} = (\iint |F_s|^2\mathrm{dxdy})^2/\iint |F_s|^4\mathrm{dxdy}$. Equation (9.4) is a (1+1)D NLSE where the spatial effects are summarized by the periodic nonlinear coefficient. Physically, the self-imaging pattern generates a z-varying effective area A_{eff}, due to the periodic beam focusing, which thus couples the spatial evolution to the temporal envelope $A(z,t)$ [68]. In Eq. (9.3) we notice that the first term, which gives the evolution of F_s in z, the Kerr effect does not appear. This means that the supposed F_s evolves in a linear fashion. To verify the

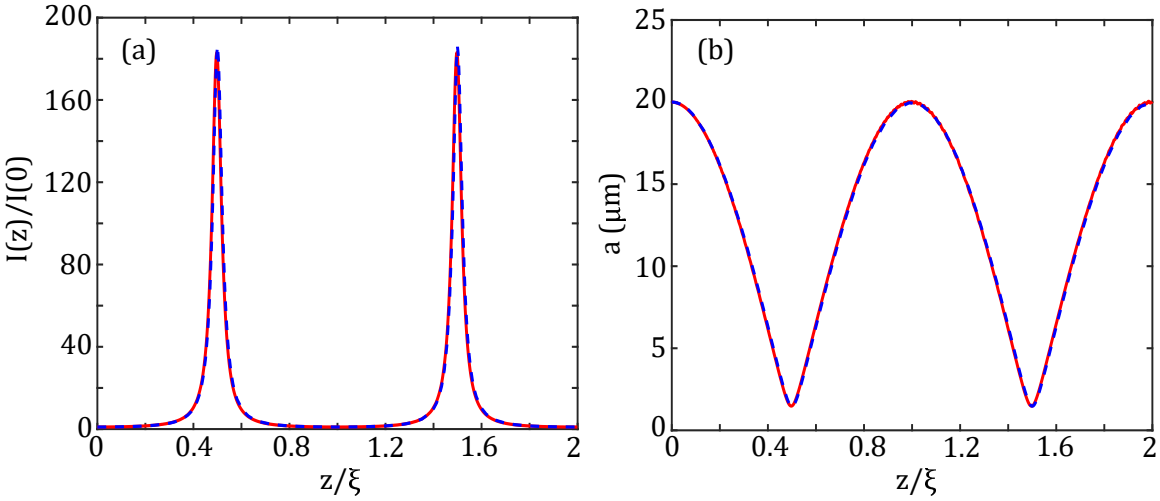

Figure 9.1: Comparative spatial evolution: (a) Intensity at the beam center normalized to its initial value. (b) Evolution of the beam size $a(z)$. Parameters: $\Delta = 0.011$, $r_{core} = 26$ μm, $n_{core} = 1.461$, $\lambda_0 = 1550$ nm, $\xi = 0.546$ mm, P_0 =75 kW and $a_0 = 20$ μm.

validity of this assumption, we have solved Eq. (9.3) in the stationary limit ($\partial_t = 0$) with parameters $\Delta = 0.011$, $r_{core} = 26$ μm, $n_{core} = 1.461$, $\lambda_0 = 1550$ nm, $P_0 = 75$ kW and $a_0 = 20$ μm. The results are compared with the assumed shape of F_s in Figure (9.1). In Figure 9.1 (a) we report the intensity at the beam center normalized to its initial value, and in Fig. 9.1 (b) the evolution of the beam radius is plotted . Results obtained by solving Eq. (9.1) are represented by solid curves whereas the results found by solving the equation of $a(z)$ are displayed with dashed lines. We see there is a good agreement between both results, which validates the assumption that F_s can be approximated by the spatial linear evolution of the beam. To point out the accuracy of (1+1)D NLSE equation to predict the temporal and spectral dynamics of (3+1)D GNLSE, a series of simulations are carried through. Two different regimes are considered: the propagation of a CW in normal dispersion regime and the evolution of femtosecond pulses in both anomalous and normal dispersion regime.

9.2 CW propagation in a GRIN fiber

To show the good accuracy of Eq. (9.4) to mimic the dynamics of Eq. (9.1), the first physical effect that we study is GPI. We will analyze two different kinds of fiber: a constant core and a periodically modulated fiber. We recall that the central frequencies of GPI bands

verify the equation:

$$D_{even}(\Omega)(D_{even}(\Omega)+2F_{av})=\left(\frac{m\pi}{\Lambda}\right)^2, \tag{9.5}$$

being Λ the spatial period of light. GPI is a process arising from random noise. To facilitate a quantitative comparision between both models and to get rid of any randomness, we seed the CW with a broadband coherent noise (a 1 fs sech with one tenth of the CW amplitude). The first analyzed case involves a constant core fiber. In this limit, the spatial period is equal to the self-imaging distance ($\Lambda = \xi$). We suppose a 6 cm long fiber with $r_{core} = 26$ μm and dispersion calculated using Sellmeier formula for germanium doped SiO_2 [74] with a doping mole fraction of $X = 0.11$. The carrier wavelength is 1064 nm and peak power P_0 is 75 kW. The initial size of the beam is a_0 =20 μm. Raman and self-steepening effects are neglected. At this frequency, the relative refractive index difference is $\Delta = 0.011$, the refractive index at the center of the core is n_{core} =1.466 and the self-imaging period is $\xi = 0.549$ mm. The output spectra are displayed in Fig. 9.2 (a). Dashed blue curve stands for the (1+1)D NLSE (Eq. (9.4)), while solid red line represents the result of (3+1)D GNLSE (Eq. (9.4)). The first feature we notice is that both models reproduce the generation of GPI bands whose position is well foreshadowed by the theory. These predictions are obtained through expression (9.5) and are represented by the dashed vertical lines. In the small inset, the first GPI band is zoomed and we can observe that the agreement between both models is almost perfect. The first two bands ($\pm$133 and $\pm$180 THz) correspond to $m = 1$ in Eq. (9.5). The fact that one harmonic can generate two pairs of GPI bands is due to HOD, as we discussed in section 3.3. The third band ($\pm$180 THz) corresponds to $m = 0$ and it is associated to the presence of a negative β_4.

The second studied case is GPI in a modulated fiber. Chosen fiber parameters are the same as in chapter 8. The modulation period is chosen to be commensurate with ξ and verifies $L_{mod} = 10/9\xi$. The spatial period can be approximated as $\Lambda = 10\xi = 6.2$ mm and the total fiber length is 6 cm. Input is a CW Gaussian beam with initial radius $a_0 = 20$ μm and a peak power of 126 kW, which corresponds to an initial intensity of 10 GW/cm^2. Evolution of the beam radius $a(z)$ has been calculated using expressions Eq. (8.14) and Eq. (8.15). In this case, both Raman and self-steepening effects have been included, although they do not play any significant role. In figure 9.2 (b), the output spectrum of simulations using (3+1)D GNLSE (solid blue) and (1+1)D GNLSE (red-dashed) are plotted. The unstable frequencies predicted by the theory are plotted as dashed black lines. The two models reproduce the typical band splitting due to the double periodicity, as we explained in previous chapters. These bands are well-predicted by the theory developed in section 8.2.

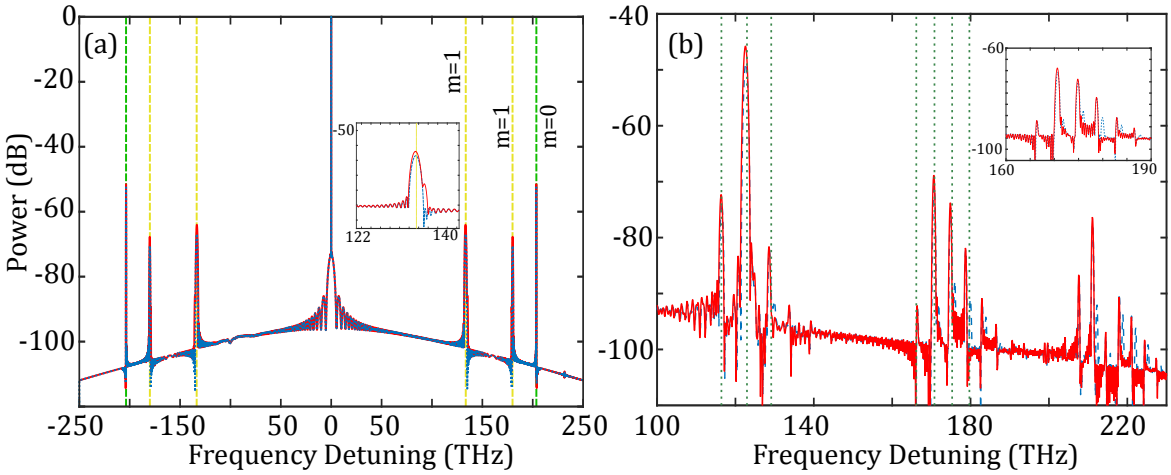

Figure 9.2: Comparative between (1+1)D GNLSE (solid red curve) and (3+1)D GNLSE (blue dashed curve) using CW as an input. (a) Constant core fiber, (b) modulated core fiber.

We see that the agreement between the results is remarkable for the first group of bands, where both simulation results are superposed. The second and third group of bands also show a good agreement, but there are some minor differences between both models. We can see that there are some bands appearing on (3+1)D GNLSE simulations which are not reproduced by (1+1)D GNLSE , as it is shown in the included inset. Simulation time needed to solve Eq. (9.4) was 1 minute, while it takes roughly 250 minutes to solve (3+1) D equation, which is 250 times faster.

9.3 Pulse propagation in a GRIN fiber

In this section we will study short pulse propagation in a GRIN fiber. The first case we consider is another paradigmatic example of spatio-temporal effect in GRIN fibers, which is the radiation emission by multimode solitons. A soliton propagating in a medium with varying nonlinearity emits radiation at frequencies according to the following phase-matching condition [201], [202]:

$$D(\Omega) - \delta\beta_1\Omega = \frac{2\pi}{\xi}m + \gamma_{av}\frac{P_s}{2}, \quad m = 0, \pm1, \pm2..., \tag{9.6}$$

where $\delta\beta_1$ takes into account the additional group velocity of the soliton acquired due to nonlinear effects such as Raman scattering [203], $D(\Omega) = \beta_2\Omega^2/2 + \beta_3\Omega^3/6$ is the dispersion operator in the frequency domain, and $\gamma_{av} = n_2\omega_0\beta_0\sqrt{g}/(2\pi c)$ is the averaged

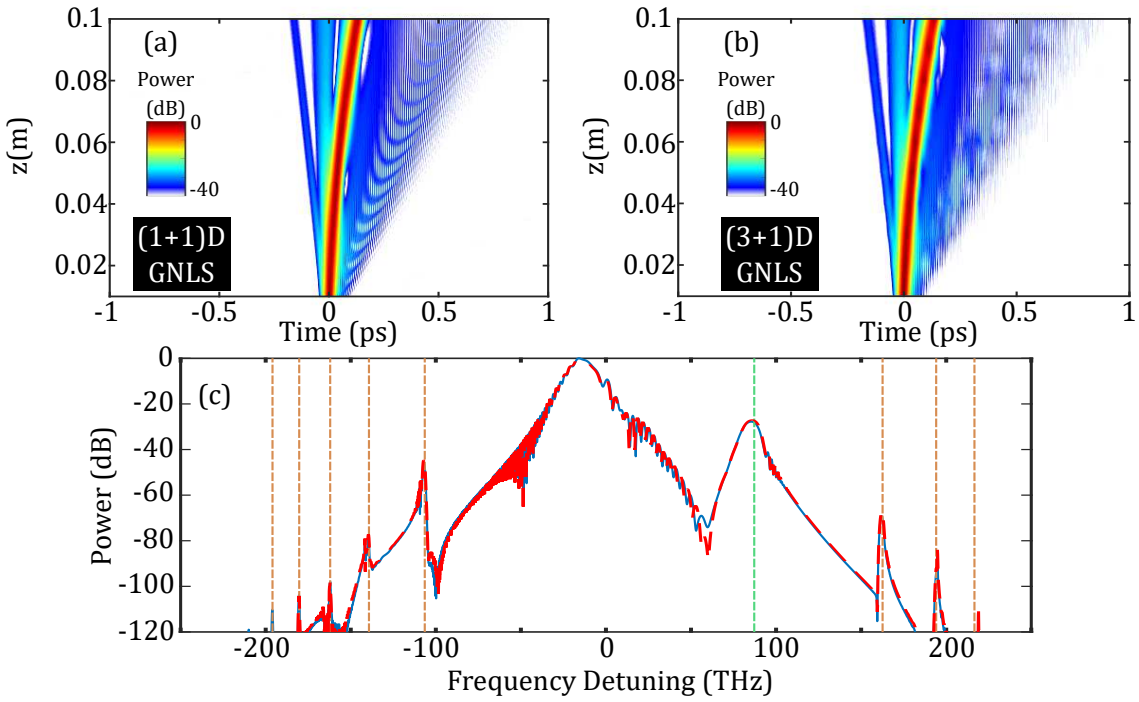

Figure 9.3: Propagation of a multimode soliton in a GRIN fiber. (a)-(b) Report the temporal evolution obtained using Eq. (9.4) for (a) and Eq. (9.1) for (b). (c) Calculated output spectrum, using Eq. (9.4) the red-dashed curve and using Eq. (9.1) for the blue-solid curve. Vertical dashed lines correspond to phase-matching conditions calculated with Eq. (9.6). Orange dashed lines correspond to values m$\neq$0, green dashed line corresponds to Cherenkov Emission. The estimated additional inverse group velocity of the soliton is $\delta\beta_1 = 0.3 \cdot 10^{-12}$ s/m. Simulation parameters: $a_0 = 30$ μm, t_0= 15 fs, P_0= 430 kW, n_{core}= 1.4605, β_2= -22$\cdot 10^{-27}$ s^2/m, β_3= 1.32$\cdot 10^{-40}$ s^3/m.

value of the nonlinear coefficient. Note that the expression predicting the frequency of Cherenkov emission Eq. (2.9) is recovered if in Eq. (9.6) the values of $\delta\beta_1$ and m are set to zero. In figure 9.3 the results of a numerically calculated propagation of a soliton using Eq. (9.4) and (9.1) are reported. In this simulation, the self-steepening effect has been neglected. In Figures 9.3 (a) and (b) we report the temporal evolution of both models, where we can clearly see how the soliton suffers a time shift due to the presence of Raman effect. Figure 9.3 (c) shows the superposition of the output spectrum, where we can see that the agreement between the two models is perfect. Both simulations are also coherent with the frequency of emitted radiation predicted by Eq. (9.6). The chosen parameters are reported in figure's caption.

As a second example, femtosecond pulse propagation in normal dispersion is studied. It has been observed that intense femtosecond pulses propagated in normal dispersion regime emit radiation [204], but the physical mechanism behind is still unknown. The chosen fiber parameters are a dispersion calculated using the Sellmeier formula with a doping mole fraction of $X = 0.11$ and $r_{core} = 26$ μm. We consider a Gaussian pulse with 250 fs at FWHM of duration at a carrier wavelength of 800 nm, where fiber dispersion is normal. Self-steepening and Raman effect have been included. Peak power has been chosen to be 500 kW and beam radius is a_0 =15 μm, which corresponds to an intensity of 70 GW/cm^2.

In figure 9.4 (a) and (b) temporal evolution of the pulse is displayed, calculated using (1+1)D GNLSE and (3+1) D GNLSE equations respectively. At 4 cm we see how the pulse sheds some radiation. The agreement between both simulations is remarkable. In figure (c), both output spectrum are compared. We see both spectra have a good agreement and specially striking is the accordance of spectral broadening of the pulse due to SPM. The bigger bands of emitted radiation have a frequency detuning of 132 THz and 173 THz, which appear in both models with a close amplitude. There is also a spectral band with a frequency detuning of 116 THz which appears in (1+1) D model but it is absent in the case of (3+1) D model. In Fig. 9.4 we show the spectral evolution of both models. We can see that the pulse spectrum broadens at the beginning of the propagation due to SPM. Near 2.5 cm, we can see that the pulse emits some radiation. This emission has been associated to GPI [204], but the relation is still unclear. Indeed, we believe this problem could entail a richer dynamics, since from our point of view, a shock wave perturbed by the varying nonlinearity could also emit resonant radiation, in analogous manner to a shock wave perturbed by HOD [205]. The reasons to support the hypothesis are: i) the frequencies of emission are not symmetric respect to the pump, ii) the distance at which the bands appear coincides with shock formation. More precisely, this phenomenon could be similar to the radiation emission by a shock wave in presence of negative β_4, where resonant radiation emission and MI coexist. We have performed intensive numerical simulations and we have observed that the produced radiation can be affected by noise, but we have not found a suitable way to predict the wavelength of emission. In parallel to numerical and theoretical analysis, we have been carrying out experiments using femtosecond lasers, but the obtained results are not yet conclusive. Therefore, a theoretical and experimental understanding of this problem is still in progress.

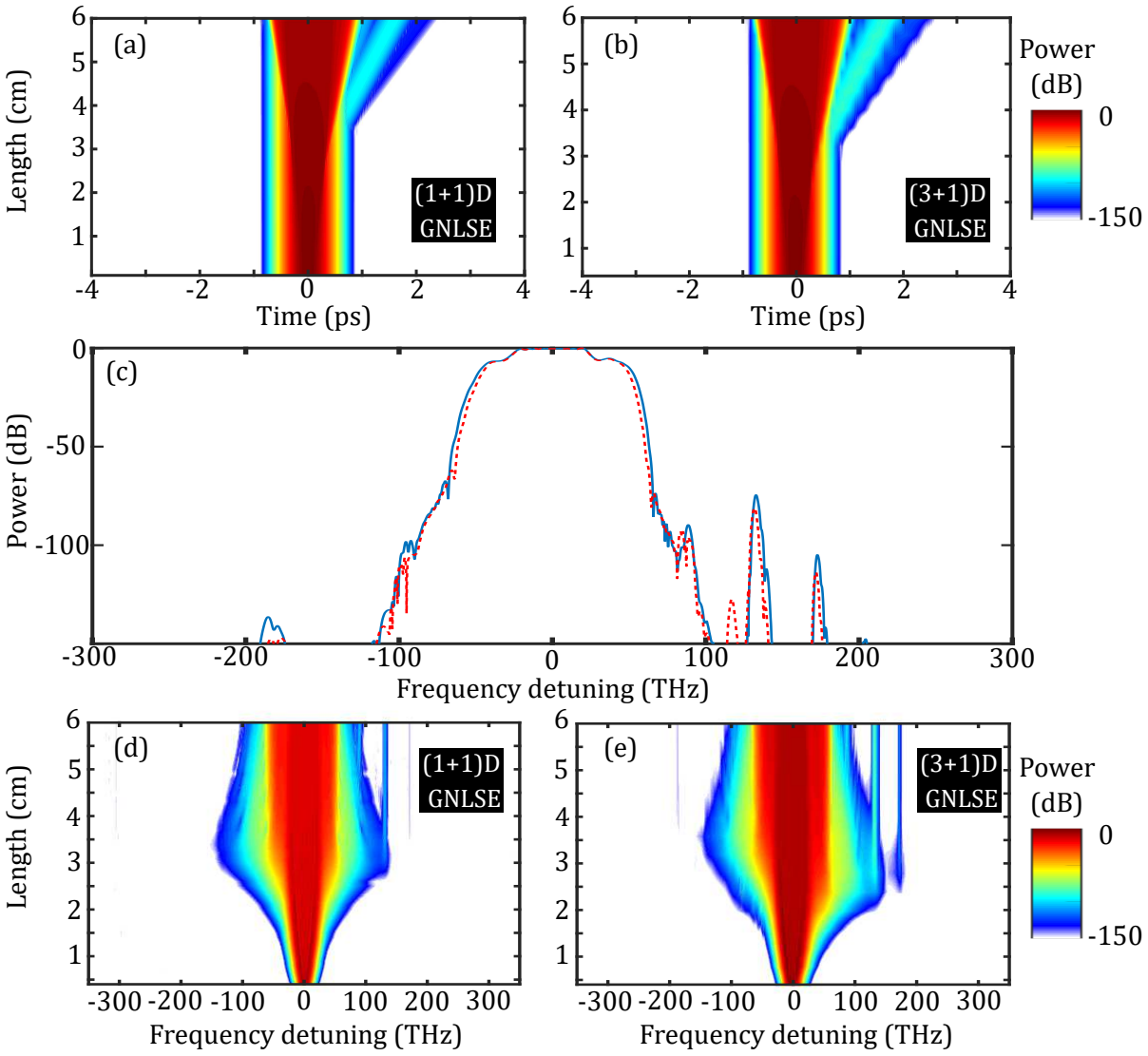

Figure 9.4: Comparative between (1+1) D GNLSE and (3+1) D GNLSE using femtosecond pulses. (a) and (b) are the respective temporal evolution. Figure(c) shows a comparative between output spectrum calculated using Eq. (9.4) the red-dashed curve and using Eq. (9.1) for the blue-solid curve. Figures (d) and (e) show the spectral evolution.

Summary

- We have derived a (1+1)D GNLSE that reproduces the spatiotemporal dynamics when a stable self-imaging is considered. This equation was characterized for having a periodic nonlinear coefficient, which summarizes the spatial evolution of light.
- The obtained model has been compared with (3+1)D GNLSE in two different limits: In the CW and femtosecond regimes. In both cases, the agreement between models was remarkable. We think that this result can be of great help in the analysis of complex phenomena hidden by the complex burden of (3+1)D GNLSE. Nevertheless, this model is only valid when a stable self-imaging is considered, and cannot describe phenomena such as azimutal instabilities, turbulence or spatial self-cleaning.

CONCLUSION

In this thesis we have studied two fundamental nonlinear phenomena taking place in optical fibers: interaction between solitons and dispersive waves and nonlinear propagation in multimode fibers. This manuscript has been focused on the theoretical aspects, putting special emphasis on finding analytic and numerical approaches which can shed some light into the physics of the involved phenomena. The most relevant results are summarized hereinafter.

- The first studied problem was the interaction between a soliton and a CW orthogonally polarized, whose result was the generation of a new frequency co-polarized with the initial CW. We described how to predict the generated wave frequency through phase-matching conditions and we found a closed expression to estimate efficiency of the process. The obtained results were confirmed by experimental measurements carried out in our laboratory using a highly-birefringent PCF. The objective of this study was to develop a complete understanding of the problem, concerning numerical simulations, analytic theory and experiments. We believe that the achievement of this objective can improve the knowledge of bright soliton dynamics and their interactions with dispersive waves in optical fibers.

- A considerable part of this manuscript was devoted to dark solitons and their interactions with dispersive waves in the neighborhood of ZDW. We have studied two important effects: on the one hand, the emission of radiation by a dark soliton, as in the case of Cherenkov radiation. Here, we reviewed how to predict the generated wave frequency. The amplitude of this newly generated wave was found by adapting the theory developed for bright solitons. On the other hand, interactions between dark solitons and CW have been considered. In this case, a generalized expression to predict the generated wave frequency was derived. In addition, an analytic expres-

sion to foresee the efficiency of the process was obtained. The theoretical results have shown a good agreement with experimental measurements obtained in the context of T. Marest's PhD.

- Concerning multimode nonlinear phenomena, the fist step was to derive a model to describe light propagation in GRIN fibers. The objective of this derivation was to discern which were the assumed approximations and the limits of the model. Once the propagation equation was defined, we explained GPI in a constant core. We shown that band position and width can be predicted using Floquet analysis. We also reported a phase-matching relation to find the central frequency of instability bands.

- GPI in a periodically modulated GRIN fiber was studied. To understand the effects of this perturbation, it was necessary to describe light spatial behavior at first. Two regimes were identified (Moiré-like and adiabatic) and an analytic approximation to describe beam propagation was found, whose overall result shown remarkable agreement with direct numerical simulations. The main effect of the periodic modulation is a splitting of GPI bands. The analytic description of the spatial behavior allowed us to predict band position and gain in the output spectrum of numerical simulations. These results explored for the first time the effects of changing periodically the diameter of a multimode fiber and we believe they will help to understand the rich nonlinear dynamics of GRIN fibers.

- The last presented result was a reduction of a (3+1)D GNLSE equation, to an equivalent (1+1)D GNLSE with varying nonlinearity. We showed that this reduction was able to reproduce with good accuracy the complex multimode dynamics both in the femtosecond and CW regime. Within the presented approach, computation time is dramatically reduced and moreover, theoretical analysis is greatly simplified. We believe this reduction can become a useful tool to find the insights of multimode solitons or GPI in modulated fibers.

Presented research naturally brings to the following opened lines and questions:

- In section 9.1, we derived a GNLSE that described light propagation in GRIN fibers. We assumed several major approximations that could drastically affect the spatiotemporal dynamics of the fiber. One of them was neglecting guide dispersion, this approximation may affect the spatial shape of the generated bands. We believe that a

systematic study involving numerical simulations, analytic approaches and experiments should be carried out in order to understand this highly complex problem.

- In our model, we neglected the waveguide disorder and we considered a spatially coherent input beam. Within this conditions, there is no beam self-cleaning. We think that a next step could be to introduce disorder in the waveguide model and study how affects to the GPI process.
- An experimental confirmation of band splitting in a periodic multimode fiber is still missing. Reaching a precise periodic modulation of a GRIN fiber at millimeter scale is a challenging technical problem. At this moment, our laboratory is developing new methods to achieve this delicate process.
- Radiation emission by a femtosecond pulse in normal dispersion regime of a GRIN fiber may be produced by a shock-wave perturbed by the periodic nonlinearity. To better understand whether the emission is a consequence of GPI or a shock, we propose to study dynamics of a step using the (1+1)D NLSE found in the last chapter.

BIBLIOGRAPHY

[1] T. H. Maiman, "Optical and microwave-optical experiments in ruby," *Phys. Rev. Lett.*, vol. 4, pp. 564–566, 11 Jun. 1960 (cit. on p. 1).

[2] P. A. Franken, A. E. Hill, C. W. Peters, and G. Weinreich, "Generation of Optical Harmonics," *Physical Review Letters*, vol. 7 (4), pp. 118–119, Aug. 1961 (cit. on pp. 1, 12).

[3] J. A. Armstrong, N. Bloembergen, J. Ducuing, and P. S. Pershan, "Interactions between light waves in a nonlinear dielectric," *Phys. Rev.*, vol. 127, pp. 1918–1939, 6 Sep. 1962 (cit. on p. 1).

[4] P. D. Maker, R. W. Terhune, and C. M. Savage, "Intensity-dependent changes in the refractive index of liquids," *Phys. Rev. Lett.*, vol. 12, pp. 507–509, 18 May 1964 (cit. on p. 1).

[5] R. Y. Chiao, C. H. Townes, and B. P. Stoicheff, "Stimulated brillouin scattering and coherent generation of intense hypersonic waves," *Phys. Rev. Lett.*, vol. 12, pp. 592–595, 21 May 1964 (cit. on p. 1).

[6] R. L. Carman, R. Y. Chiao, and P. L. Kelley, "Observation of degenerate stimulated four-photon interaction and four-wave parametric amplification," *Phys. Rev. Lett.*, vol. 17, pp. 1281–1283, 26 Dec. 1966 (cit. on p. 1).

[7] F. P. Kapron, D. B. Keck, and R. D. Maurer, "Radiation losses in glass optical waveguides," *Applied Physics Letters*, vol. 17 (10), pp. 423–425, 1970 (cit. on p. 1).

[8] R. H. Stolen, E. P. Ippen, and A. R. Tynes, "Raman oscillation in glass optical waveguide," *Applied Physics Letters*, vol. 20 (2), pp. 62–64, Jan. 1972 (cit. on pp. 1, 13).

[9] R. H. Stolen and E. P. Ippen, "Raman gain in glass optical waveguides," *Applied Physics Letters*, vol. 22 (6), pp. 276–278, 1973 (cit. on p. 1).

[10] E. Ippen and R. Stolen, "Stimulated brillouin scattering in optical fibers," *Applied Physics Letters*, vol. 21 (11), pp. 539–541, 1972 (cit. on p. 1).

[11] R. Stolen and A. Ashkin, "Optical kerr effect in glass waveguide," *Applied Physics Letters*, vol. 22 (6), pp. 294–296, 1973 (cit. on p. 1).

[12] R. H. Stolen, "The early years of fiber nonlinear optics," *Journal of Lightwave Technology*, vol. 26 (9), pp. 1021–1031, May 2008 (cit. on p. 1).

[13] G. P. Agrawal, "Nonlinear fiber optics: Its history and recent progress," *J. Opt. Soc. Am. B*, vol. 28 (12), A1–A10, Dec. 2011 (cit. on p. 1).

[14] P. G. Drazin and R. S. Johnson, *Solitons: an introduction*, Second Edition. Cambridge texts in applied mathematics, 1989 (cit. on p. 1).

[15] N. J. Zabusky and M. D. Kruskal, "Interaction of "Solitons" in a Collisionless Plasma and the Recurrence of Initial States," *Physical Review Letters*, vol. 15 (6), pp. 240–243, Aug. 1965 (cit. on p. 1).

[16] S. Burger, K. Bongs, S. Dettmer, W. Ertmer, K. Sengstock, A. Sanpera, G. V. Shlyapnikov, and M. Lewenstein, "Dark Solitons in Bose-Einstein Condensates," *Physical Review Letters*, vol. 83 (25), pp. 5198–5201, Dec. 1999 (cit. on p. 2).

[17] L. Khaykovich, F. Schreck, G. Ferrari, T. Bourdel, J. Cubizolles, L. D. Carr, Y. Castin, and C. Salomon, "Formation of a Matter-Wave Bright Soliton," *Science*, vol. 296 (5571), pp. 1290–1293, May 2002 (cit. on p. 2).

[18] K. E. Strecker, G. B. Partridge, A. G. Truscott, and R. G. Hulet, "Bright matter wave solitons in Bose–Einstein condensates," *New Journal of Physics*, vol. 5, p. 73, Jun. 2003 (cit. on p. 2).

[19] J. Wu, R. Keolian, and I. Rudnick, "Observation of a Nonpropagating Hydrodynamic Soliton," *Physical Review Letters*, vol. 52 (16), pp. 1421–1424, Apr. 1984 (cit. on p. 2).

[20] T. Heimburg and A. D. Jackson, "On soliton propagation in biomembranes and nerves," *Proceedings of the National Academy of Sciences*, vol. 102 (28), pp. 9790–9795, Jul. 2005 (cit. on p. 2).

[21] M. Segev, B. Crosignani, A. Yariv, and B. Fischer, "Spatial solitons in photorefractive media," *Physical Review Letters*, vol. 68 (7), pp. 923–926, Feb. 1992 (cit. on p. 2).

[22] C. Conti, M. Peccianti, and G. Assanto, "Observation of Optical Spatial Solitons in a Highly Nonlocal Medium," *Physical Review Letters*, vol. 92 (11), Mar. 2004 (cit. on p. 2).

[23] A. Ferrando, M. Zacarés, P. F. de Córdoba, D. Binosi, and J. A. Monsoriu, "Spatial soliton formation in photonic crystal fibers," *Optics Express*, vol. 11 (5), pp. 452–459, Mar. 2003 (cit. on p. 2).

[24] Y. V. Kartashov, B. A. Malomed, and L. Torner, "Solitons in nonlinear lattices," *Reviews of Modern Physics*, vol. 83 (1), pp. 247–305, Apr. 2011 (cit. on p. 2).

[25] A. Hasegawa and F. Tappert, "Transmission of stationary nonlinear optical pulses in dispersive dielectric fibers. I. Anomalous dispersion," *Applied Physics Letters*, vol. 23 (3), pp. 142–144, Aug. 1973 (cit. on p. 2).

[26] L. F. Mollenauer, R. H. Stolen, and J. P. Gordon, "Experimental Observation of Picosecond Pulse Narrowing and Solitons in Optical Fibers," *Physical Review Letters*, vol. 45 (13), pp. 1095–1098, Sep. 1980 (cit. on p. 2).

[27] A. Hasegawa, "Numerical study of optical soliton transmission amplified periodically by the stimulated Raman process," *Applied Optics*, vol. 23 (19), pp. 3302–3309, Oct. 1984 (cit. on pp. 2, 19).

[28] J. P. Gordon and H. A. Haus, "Random walk of coherently amplified solitons in optical fiber transmission," *Optics Letters*, vol. 11 (10), pp. 665–667, Oct. 1986 (cit. on p. 2).

[29] R.-J. Essiambre and G. P. Agrawal, "Timing jitter of ultrashort solitons in high-speed communication systems I General formulation and application to dispersion-decreasing fibers," *Journal of the Optical Society of America B*, vol. 14 (2), pp. 314–322, Feb. 1997 (cit. on p. 2).

[30] G. P. Agrawal, *Fiber-optic communication systems*, Fourth Edition. Wiley-Interscience, 2010 (cit. on p. 2).

[31] H. A. Haus and W. S. Wong, "Solitons in optical communications," *Rev. Mod. Phys.*, vol. 68 (2), pp. 423–444, Apr. 1996 (cit. on p. 2).

[32] J. E. Prilepsky, S. A. Derevyanko, and S. K. Turitsyn, "Temporal solitonic crystals and non-hermitian informational lattices," *Phys. Rev. Lett.*, vol. 108, p. 183 902, 18 May 2012 (cit. on p. 2).

[33] L. L. Frumin, A. A. Gelash, and S. K. Turitsyn, "New approaches to coding information using inverse scattering transform," *Phys. Rev. Lett.*, vol. 118, p. 223 901, 22 May 2017 (cit. on p. 2).

[34] J. K. Ranka, R. S. Windeler, and A. J. Stentz, "Visible continuum generation in air–silica microstructure optical fibers with anomalous dispersion at 800 nm," *Optics Letters*, vol. 25 (1), pp. 25–27, Jan. 2000 (cit. on pp. 2, 15).

[35] D. V. Skryabin and A. V. Gorbach, "*Colloquium* : Looking at a soliton through the prism of optical supercontinuum," *Reviews of Modern Physics*, vol. 82 (2), pp. 1287–1299, Apr. 2010 (cit. on pp. 2, 24, 25).

[36] V. Zakharov and L. Ostrovsky, "Modulation instability: The beginning," *Physica D: Nonlinear Phenomena*, vol. 238 (5), pp. 540–548, Mar. 2009 (cit. on p. 2).

[37] T. Taniuti and H. Washimi, "Self-Trapping and Instability of Hydromagnetic Waves Along the Magnetic Field in a Cold Plasma," *Physical Review Letters*, vol. 21 (4), pp. 209–212, Jul. 1968 (cit. on p. 2).

[38] T. B. Benjamin and J. E. Feir, "The disintegration of wave trains on deep water Part 1. Theory," *Journal of Fluid Mechanics*, vol. 27 (03), p. 417, Feb. 1967 (cit. on p. 2).

[39] K. E. Strecker, G. B. Partridge, A. G. Truscott, and R. G. Hulet, "Formation and propagation of matter-wave soliton trains," *Nature*, vol. 417 (6885), pp. 150–153, May 2002 (cit. on p. 2).

[40] G. Agrawal, *Nonlinear Fiber Optics*, Fifth Edition. Elsevier, 2013 (cit. on pp. 2, 8, 11, 20, 23, 29, 35, 44, 53, 84, 86).

[41] S. Pitois and G. Millot, "Experimental observation of a new modulational instability spectral window induced by fourth-order dispersion in a normally dispersive single-mode optical fiber," *Optics Communications*, vol. 226 (1), pp. 415–422, 2003 (cit. on pp. 2, 32).

[42] S. Wabnitz, "Modulational polarization instability of light in a nonlinear birefringent dispersive medium," *Physical Review A*, vol. 38 (4), pp. 2018–2021, Aug. 1988 (cit. on p. 2).

[43] M. Guasoni, "Generalized modulational instability in multimode fibers: Wideband multimode parametric amplification," *Physical Review A*, vol. 92 (3), p. 033 849, Sep. 2015 (cit. on pp. 2, 78).

[44] A. Mussot, M. Conforti, S. Trillo, F. Copie, and A. Kudlinski, "Modulation instability in dispersion oscillating fibers," *Advances in Optics and Photonics*, vol. 10 (1), pp. 1–42, Mar. 2018 (cit. on pp. 2, 3).

[45] M. Faraday, "XVII. On a peculiar class of acoustical figures; and on certain forms assumed by groups of particles upon vibrating elastic surfaces," *Philosophical Transactions of the Royal Society of London*, vol. 121, pp. 299–340, Jan. 1831 (cit. on p. 3).

[46] M. C. Cross and P. C. Hohenberg, "Pattern formation outside of equilibrium," *Rev. Mod. Phys.*, vol. 65 (3), pp. 851–1112, Jul. 1993 (cit. on p. 3).

[47] J. J. García-Ripoll, V. M. Pérez-García, and P. Torres, "Extended Parametric Resonances in Nonlinear Schrödinger Systems," *Phys. Rev. Lett.*, vol. 83 (9), pp. 1715–1718, 1999 (cit. on p. 3).

[48] K. Staliunas, S. Longhi, and G. J. de Valcárcel, "Faraday Patterns in Bose-Einstein Condensates," *Physical Review Letters*, vol. 89 (21), Nov. 2002 (cit. on p. 3).

[49] Staliunas, Kestutis and Longhi, Stefano and de Valcárcel, Germán J., "Faraday patterns in low-dimensional Bose-Einstein condensates," *Phys. Rev. A*, vol. 70 (1), p. 011 601, Jul. 2004 (cit. on p. 3).

[50] Engels, P. and Atherton, C. and Hoefer, M. A., "Observation of Faraday Waves in a Bose-Einstein Condensate," *Phys. Rev. Lett.*, vol. 98 (9), p. 095 301, Feb. 2007 (cit. on p. 3).

[51] T. M. Hoang, M. Anquez, B. A. Robbins, X. Y. Yang, B. J. Land, C. D. Hamley, and M. S. Chapman, "Parametric excitation and squeezing in a many-body spinor condensate," *Nature Communications*, vol. 7, p. 11 233, Apr. 2016 (cit. on p. 3).

[52] S. J. Moon, M. D. Shattuck, C. Bizon, D. I. Goldman, J. B. Swift, and H. L. Swinney, "Phase bubbles and spatiotemporal chaos in granular patterns," *Phys. Rev. E*, vol. 65 (1), p. 011 301, Dec. 2001 (cit. on p. 3).

[53] P. B. Umbanhowar, F. Melo, and H. L. Swinney, "Localized excitations in a vertically vibrated granular layer," *Nature*, vol. 382, pp. 793–796, 1996 (cit. on p. 3).

[54] O. Lioubashevski, Y. Hamiel, A. Agnon, Z. Reches, and J. Fineberg, "Oscillons and Propagating Solitary Waves in a Vertically Vibrated Colloidal Suspension," *Physical Review Letters*, vol. 83 (16), pp. 3190–3193, Oct. 1999 (cit. on p. 3).

[55] D. Rugar and P. Grütter, "Mechanical parametric amplification and thermomechanical noise squeezing," *Physical Review Letters*, vol. 67 (6), pp. 699–702, Aug. 1991 (cit. on p. 3).

[56] V. Petrov, Q. Ouyang, and H. L. Swinney, "Resonant pattern formation in a chemical system," *Nature*, vol. 388, p. 655, 1997 (cit. on p. 3).

[57] F. Matera, A. Mecozzi, M. Romagnoli, and M. Settembre, "Sideband instability induced by periodic power variation in long-distance fiber links," *Opt. Lett.*, vol. 18 (18), pp. 1499–1501, Sep. 1993 (cit. on p. 3).

[58] A. Armaroli and F. Biancalana, "Tunable modulational instability sidebands via parametric resonance in periodically tapered optical fibers," *Opt. Express*, vol. 20 (22), pp. 25 096–25 110, 2012 (cit. on pp. 3, 35).

[59] S. R. Nodari, M. Conforti, G. Dujardin, A. Kudlinski, A. Mussot, S. Trillo, and S. De Bièvre, "Modulational instability in dispersion-kicked optical fibers," *Phys. Rev. A*, vol. 92 (1), p. 013 810, 2015 (cit. on p. 3).

[60] M. Droques, A. Kudlinski, G. Bouwmans, G. Martinelli, and A. Mussot, "Dynamics of the modulation instability spectrum in optical fibers with oscillating dispersion," *Phys. Rev. A*, vol. 87 (1), p. 013 813, Jan. 2013 (cit. on p. 3).

[61] C. Finot, J. Fatome, A. Sysoliatin, A. Kosolapov, and S. Wabnitz, "Competing four-wave mixing processes in dispersion oscillating telecom fiber," *Opt. Lett.*, vol. 38 (24), pp. 5361–5364, Dec. 2013 (cit. on p. 3).

[62] M. Droques, A. Kudlinski, G. Bouwmans, G. Martinelli, and A. Mussot, "Experimental demonstration of modulation instability in an optical fiber with a periodic dispersion landscape," *Opt. Lett.*, vol. 37 (23), pp. 4832–4834, Dec. 2012 (cit. on p. 3).

[63] F. K. Abdullaev, S. A. Darmanyan, S. Bischoff, and M. P. Sørensen, "Modulational instability of electromagnetic waves in media with varying nonlinearity," *J. Opt. Soc. Am. B*, vol. 14 (1), pp. 27–33, Jan. 1997 (cit. on p. 3).

[64] K. Staliunas, C. Hang, and V. V. Konotop, "Parametric patterns in optical fiber ring nonlinear resonators," *Phys. Rev. A*, vol. 88 (2), p. 023 846, Aug. 2013 (cit. on p. 3).

[65] L. B. Soldano and E. C. M. Pennings, "Optical multi-mode interference devices based on self-imaging: Principles and applications," *Journal of Lightwave Technology*, vol. 13 (4), pp. 615–627, 1995 (cit. on pp. 3, 17).

[66] A. Mafi, "Pulse Propagation in a Short Nonlinear Graded-Index Multimode Optical Fiber," *Journal of Lightwave Technology*, vol. 30 (17), pp. 2803–2811, Sep. 2012 (cit. on pp. 3, 16, 76, 89).

[67] L. G. Wright, S. Wabnitz, D. N. Christodoulides, and F. W. Wise, "Ultrabroadband Dispersive Radiation by Spatiotemporal Oscillation of Multimode Waves," *Phys. Rev. Lett.*, vol. 115 (22), p. 223 902, Nov. 2015 (cit. on p. 3).

[68] M. Conforti, C. Mas Arabi, A. Mussot, and A. Kudlinski, "Fast and accurate modeling of nonlinear pulse propagation in graded-index multimode fibers," *Optics Letters*, vol. 42 (19), p. 4004, Oct. 2017 (cit. on pp. 3, 30, 33, 107, 108).

[69] K. Krupa, A. Tonello, A. Barthélémy, V. Couderc, B. M. Shalaby, A. Bendahmane, G. Millot, and S. Wabnitz, "Observation of Geometric Parametric Instability Induced by the Periodic Spatial Self-Imaging of Multimode Waves," *Physical Review Letters*, vol. 116 (18), p. 183 901, May 2016 (cit. on pp. 3, 77, 79, 85, 91).

[70] A. W. Snyder and J. D. Love, *Optical waveguide theory*, First Edition. Chapman and Hall, 1983 (cit. on pp. 8, 9).

[71] F. Mitschke, *Fiber optics: physics and technology*. Springer, 2009 (cit. on p. 9).

[72] A. Couairon, E. Brambilla, T. Corti, D. Majus, O. d. J. Ramírez-Góngora, and M. Kolesik, "Practitioner's guide to laser pulse propagation models and simulation," *The European Physical Journal Special Topics*, vol. 199 (1), pp. 5–76, Nov. 2011 (cit. on pp. 10, 54, 83).

[73] R. Boyd, *Nonlinear Optics*, Third Edition. Elsevier, 2008 (cit. on pp. 10, 12).

[74] J. W. Fleming, "Dispersion in GeO_2–SiO_2 glasses," *Applied Optics*, vol. 23 (24), pp. 4486–4493, Dec. 1984 (cit. on pp. 11, 110).

[75] P. N. Butcher and D. Cotter, *The Elements of Nonlinear Optics*, First Edition. Cambridge University Press, 1990 (cit. on p. 12).

[76] P. G. Kazansky, L. Dong, and P. S. J. Russell, "High second-order nonlinearities in poled silicate fibers," *Optics Letters*, vol. 19 (10), pp. 701–703, May 1994 (cit. on p. 12).

[77] U. Österberg and W. Margulis, "Dye laser pumped by Nd:YAG laser pulses frequency doubled in a glass optical fiber," *Optics Letters*, vol. 11 (8), pp. 516–518, Aug. 1986 (cit. on p. 12).

[78] J. M. Gabriagues, "Third-harmonic and three-wave sum-frequency light generation in an elliptical-core optical fiber," *Optics Letters*, vol. 8 (3), pp. 183–185, Mar. 1983 (cit. on p. 13).

[79] U. Osterberg, "Growth of third-harmonic signal in optical glass fibre," *Electronics Letters*, vol. 26 (2), pp. 103–104, Jan. 1990 (cit. on p. 13).

[80] K. Kim, R. H. Stolen, W. A. Reed, and K. W. Quoi, "Measurement of the nonlinear index of silica-core and dispersion-shifted fibers," *Opt. Lett.*, vol. 19 (4), pp. 257–259, Feb. 1994 (cit. on p. 13).

[81] C. Raman, "A new radiation," *Indian J. Phys.*, vol. 2, pp. 387–389, Mar. 1928 (cit. on p. 13).

[82] J. P. Gordon, "Theory of the soliton self-frequency shift," *Optics Letters*, vol. 11 (10), pp. 662–664, Oct. 1986 (cit. on p. 14).

[83] P. Yeh, A. Yariv, and E. Marom, "Theory of Bragg fiber," *JOSA*, vol. 68 (9), pp. 1196–1201, Sep. 1978 (cit. on p. 14).

[84] J. C. Knight, T. A. Birks, P. S. J. Russell, and D. M. Atkin, "All-silica single-mode optical fiber with photonic crystal cladding," *Optics Letters*, vol. 21 (19), pp. 1547–1549, Oct. 1996 (cit. on p. 14).

[85] J. D. Joannopoulos, S. G. Johnson, J. N. Winn, and R. D. Meade, *Photonic Crystals, molding the flow of light*. Princeton University Press (cit. on pp. 15, 36).

[86] A. Ortigosa-Blanch, J. C. Knight, W. J. Wadsworth, J. Arriaga, B. J. Mangan, T. A. Birks, and P. S. J. Russell, "Highly birefringent photonic crystal fibers," *Optics letters*, vol. 25 (18), pp. 1325–1327, Sep. 2000 (cit. on p. 15).

[87] D. Mogilevtsev, T. A. Birks, and P. S. J. Russell, "Group-velocity dispersion in photonic crystal fibers," *Optics Letters*, vol. 23 (21), pp. 1662–1664, Nov. 1998 (cit. on p. 15).

[88] A. Ferrando, E. Silvestre, J. J. Miret, and P. Andrés, "Nearly zero ultraflattened dispersion in photonic crystal fibers," *Opt. Lett.*, vol. 25 (11), pp. 790–792, Jun. 2000 (cit. on p. 15).

[89] M. Napierała, T. Nasilowski, E. Bereś-Pawlik, P. Mergo, F. Berghmans, and H. Thienpont, "Large-mode-area photonic crystal fiber with double lattice constant structure and low bending loss," *Optics Express*, vol. 19 (23), pp. 22 628–22 636, Nov. 2011 (cit. on p. 15).

[90] J. M. Dudley and J. R. Taylor, Eds., *Supercontinuum generation in optical fibers*. Cambridge University Press, 2010 (cit. on p. 15).

[91] A. Ferrando, E. Silvestre, J. J. Miret, P. Andrés, and M. V. Andrés, "Full-vector analysis of a realistic photonic crystal fiber," *Opt. Lett.*, vol. 24 (5), pp. 276–278, Mar. 1999 (cit. on p. 15).

[92] R. F. Cregan, B. J. Mangan, J. C. Knight, T. A. Birks, P. S. J. Russell, P. J. Roberts, and D. C. Allan, "Single-Mode Photonic Band Gap Guidance of Light in Air," *Science*, vol. 285 (5433), pp. 1537–1539, Sep. 1999 (cit. on p. 15).

[93] P. S. Russell, "Photonic-Crystal Fibers," *Journal of Lightwave Technology*, vol. 24 (12), pp. 4729–4749, Dec. 2006 (cit. on p. 15).

[94] J. M. Dudley, G. Genty, and S. Coen, "Supercontinuum generation in photonic crystal fiber," *Reviews of Modern Physics*, vol. 78 (4), pp. 1135–1184, Oct. 2006 (cit. on pp. 20, 75).

[95] V. E. Zakharov and A. Shabat, "Exact theory of two-dimensional self-focusing and one-dimensional self-modulation of waves in nonlinear media," *Soviet Physics JETP*, vol. 34 (1), p. 62, 1972 (cit. on p. 21).

[96] P. K. A. Wai, C. R. Menyuk, Y. C. Lee, and H. H. Chen, "Nonlinear pulse propagation in the neighborhood of the zero-dispersion wavelength of monomode optical fibers," *Optics Letters*, vol. 11 (7), pp. 464–466, Jul. 1986 (cit. on p. 23).

[97] N. Akhmediev and M. Karlsson, "Cherenkov radiation emitted by solitons in optical fibers," *Physical Review A*, vol. 51 (3), pp. 2602–2607, Mar. 1995 (cit. on p. 23).

[98] P. K. A. Wai, C. R. Menyuk, H. H. Chen, and Y. C. Lee, "Soliton at the zero-group-dispersion wavelength of a single-model fiber," *Optics Letters*, vol. 12 (8), pp. 628–630, Aug. 1987 (cit. on p. 23).

[99] V. I. Karpman, "Radiation by solitons due to higher-order dispersion," *Physical Review E*, vol. 47 (3), pp. 2073–2082, Mar. 1993 (cit. on p. 23).

[100] D. V. Skryabin, F. Luan, J. C. Knight, and P. S. J. Russell, "Soliton Self-Frequency Shift Cancellation in Photonic Crystal Fibers," *Science*, vol. 301 (5640), p. 1705, Sep. 2003 (cit. on p. 23).

[101] F. Biancalana, D. V. Skryabin, and A. V. Yulin, "Theory of the soliton self-frequency shift compensation by the resonant radiation in photonic crystal fibers," *Physical Review E*, vol. 70 (1), p. 16 615, Jul. 2004 (cit. on pp. 23, 57, 60, 63, 64).

[102] V. Karpman, "Stationary and radiating dark solitons of the third order nonlinear Schrödinger equation," *Physics Letters A*, vol. 181 (3), pp. 211–215, Oct. 1993 (cit. on pp. 23, 57).

[103] V. V. Afanasjev, C. R. Menyuk, and Y. S. Kivshar, "Effect of third-order dispersion on dark solitons," *Optics Letters*, vol. 21 (24), pp. 1975–1977, Dec. 1996 (cit. on pp. 23, 57, 60).

[104] C. Milián, D. V. Skryabin, and A. Ferrando, "Continuum generation by dark solitons," *Optics Letters*, vol. 34 (14), p. 2096, Jul. 2009 (cit. on pp. 23, 57, 61).

[105] T. Marest, C. Mas Arabí, M. Conforti, A. Mussot, C. Milián, D. V. Skryabin, and A. Kudlinski, "Emission of dispersive waves from a train of dark solitons in optical fibers," *Optics Letters*, vol. 41 (11), p. 2454, Jun. 2016 (cit. on pp. 23, 58, 61).

[106] T. Marest, C. M. Arabí, M. Conforti, A. Mussot, C. Milián, D. V. Skryabin, and A. Kudlinski, "Grayness-dependent emission of dispersive waves from dark solitons in optical fibers," *Optics Letters*, vol. 43 (7), p. 1511, Apr. 2018 (cit. on p. 23).

[107] R. Driben, A. V. Yulin, and A. Efimov, "Resonant radiation from oscillating higher order solitons," *Optics Express*, vol. 23 (15), p. 19 112, Jul. 2015 (cit. on p. 23).

[108] J. Cheng, M. E. V. Pedersen, K. Charan, K. Wang, C. Xu, L. Grüner-Nielsen, and D. Jakobsen, "Intermodal čerenkov radiation in a higher-order-mode fiber," *Optics Letters*, vol. 37 (21), p. 4410, Nov. 2012 (cit. on p. 23).

[109] A. Efimov, A. V. Yulin, D. V. Skryabin, J. C. Knight, N. Joly, F. G. Omenetto, A. J. Taylor, and P. Russell, "Interaction of an Optical Soliton with a Dispersive Wave," *Physical Review Letters*, vol. 95 (21), Nov. 2005 (cit. on p. 24).

[110] A. Efimov, A. J. Taylor, A. V. Yulin, D. V. Skryabin, and J. C. Knight, "Phase-sensitive scattering of a continuous wave on a soliton," *Optics Letters*, vol. 31 (11), p. 1624, Jun. 2006 (cit. on pp. 24, 43).

[111] A. Demircan, S. Amiranashvili, and G. Steinmeyer, "Controlling Light by Light with an Optical Event Horizon," *Physical Review Letters*, vol. 106 (16), Apr. 2011 (cit. on p. 24).

[112] T. G. Philbin, C. Kuklewicz, S. Robertson, S. Hill, F. König, and U. Leonhardt, "Fiber-Optical Analog of the Event Horizon," *Science*, vol. 319 (5868), p. 1367, Mar. 2008 (cit. on p. 24).

[113] K. E. Webb, M. Erkintalo, Y. Xu, N. G. R. Broderick, J. M. Dudley, G. Genty, and S. G. Murdoch, "Nonlinear optics of fibre event horizons," *Nature Communications*, vol. 5, p. 4969, Sep. 2014 (cit. on p. 24).

[114] R. Driben, A. V. Yulin, A. Efimov, and B. A. Malomed, "Trapping of light in solitonic cavities and its role in the supercontinuum generation," *Optics Express*, vol. 21 (16), p. 19 091, Aug. 2013 (cit. on p. 24).

[115] S. F. Wang, A. Mussot, M. Conforti, X. L. Zeng, and A. Kudlinski, "Bouncing of a dispersive wave in a solitonic cage," *Optics Letters*, vol. 40 (14), p. 3320, Jul. 2015 (cit. on p. 24).

[116] T. Voytova, I. Oreshnikov, A. V. Yulin, and R. Driben, "Emulation of Fabry–Perot and Bragg resonators with temporal optical solitons," *Optics Letters*, vol. 41 (11), p. 2442, Jun. 2016 (cit. on p. 24).

[117] I. Oreshnikov, R. Driben, and A. V. Yulin, "Weak and strong interactions between dark solitons and dispersive waves," *Optics Letters*, vol. 40 (21), p. 4871, Nov. 2015 (cit. on pp. 24, 57).

[118] ——, "Interaction of high-order solitons with external dispersive waves," *Opt. Lett.*, vol. 40 (23), pp. 5554–5557, Dec. 2015 (cit. on p. 24).

[119] K. Tai, A. Hasegawa, and A. Tomita, "Observation of modulational instability in optical fibers," *Physical Review Letters*, vol. 56 (2), pp. 135–138, Jan. 1986 (cit. on p. 32).

[120] J. D. Harvey, R. Leonhardt, S. Coen, G. K. L. Wong, J. Knight, W. J. Wadsworth, and P. St.J. Russell, "Scalar modulation instability in the normal dispersion regime by use of a photonic crystal fiber," *Optics Letters*, vol. 28 (22), p. 2225, Nov. 2003 (cit. on p. 32).

[121] S. B. Cavalcanti, J. C. Cressoni, H. R. da Cruz, and A. S. Gouveia-Neto, "Modulation instability in the region of minimum group-velocity dispersion of single-mode optical fibers via an extended nonlinear schrödinger equation," *Phys. Rev. A*, vol. 43, pp. 6162–6165, 11 Jun. 1991 (cit. on p. 32).

[122] F. Bessin, F. Copie, M. Conforti, A. Kudlinski, and A. Mussot, "Modulation instability in the weak normal dispersion region of passive fiber ring cavities," *Optics Letters*, vol. 42 (19), p. 3730, Oct. 2017 (cit. on p. 32).

[123] G. W. Hill, "On the part of the motion of the lunar perigee which is a function of the mean motions of the sun and moon," *Acta Mathematica*, vol. 8 (0), pp. 1–36, 1886 (cit. on p. 34).

[124] C. M. Bender and S. A. Orszag, *Advanced Mathematical Methods for Scientists and Engineers*. Springer, 1999 (cit. on pp. 34, 36, 96, 99).

[125] M. Droques, A. Kudlinski, G. Bouwmans, G. Martinelli, A. Mussot, A. Armaroli, and F. Biancalana, "Fourth-order dispersion mediated modulation instability in dispersion oscillating fibers," *Optics Letters*, vol. 38 (17), p. 3464, Sep. 2013 (cit. on p. 36).

[126] A. H. Nayfeh and D. T. Mook, *Nonlinear Oscillations*. Wiley, 1995 (cit. on p. 36).

[127] J. J. Sakurai and J. Napolitano, *Modern quantum mechanics*, Second Edition. Addison-Wesley, Pearson, 2011 (cit. on p. 36).

[128] A. V. Yulin, L. R. Gorjão, R. Driben, and D. V. Skryabin, "Tuning resonant interaction of orthogonally polarized solitons and dispersive waves with the soliton power," *Optics Express*, vol. 22 (9), p. 10 995, May 2014 (cit. on p. 43).

[129] K. J. Blow, N. J. Doran, and D. Wood, "Polarization instabilities for solitons in birefringent fibers," *Optics Letters*, vol. 12 (3), p. 202, Mar. 1987 (cit. on pp. 45, 52).

[130] D. V. Skryabin and A. V. Yulin, "Theory of generation of new frequencies by mixing of solitons and dispersive waves in optical fibers," *Physical Review E*, vol. 72 (1), Jul. 2005 (cit. on pp. 45, 46, 48, 49, 66).

[131] C. Mas Arabí, F. Bessin, A. Kudlinski, A. Mussot, D. Skryabin, and M. Conforti, "Efficiency of four-wave mixing between orthogonally polarized linear waves and solitons in a birefringent fiber," *Physical Review A*, vol. 94 (6), p. 063 847, Dec. 2016 (cit. on p. 48).

[132] A. Choudhary and F. König, "Efficient frequency shifting of dispersive waves at solitons," *Optics Express*, vol. 20 (5), p. 5538, Feb. 2012 (cit. on pp. 52, 69, 70).

[133] H. G. Winful, "Polarization instabilities in birefringent nonlinear media: Application to fiber-optic devices," *Optics Letters*, vol. 11 (1), p. 33, Jan. 1986 (cit. on p. 52).

[134] F. Luan, A. Yulin, J. C. Knight, and D. V. Skryabin, "Polarization instability of solitons in photonic crystal fibers," *Optics Express*, vol. 14 (14), p. 6550, 2006 (cit. on p. 52).

[135] N. Akhmediev and J. M. Soto-Crespo, "Dynamics of solitonlike pulse propagation in birefringent optical fibers," *Physical Review E*, vol. 49 (6), pp. 5742–5754, Jun. 1994 (cit. on p. 52).

[136] Y. Barad and Y. Silberberg, "Polarization Evolution and Polarization Instability of Solitons in a Birefringent Optical Fiber," *Physical Review Letters*, vol. 78 (17), pp. 3290–3293, Apr. 1997 (cit. on p. 52).

[137] D. C. Hutchings and J. M. Arnold, "Polarization stability of solitons in birefringent optical fibers," *Journal of the Optical Society of America B*, vol. 16 (4), p. 513, Apr. 1999 (cit. on p. 52).

[138] D. Krökel, N. J. Halas, G. Giuliani, and D. Grischkowsky, "Dark-Pulse Propagation in Optical Fibers," *Physical Review Letters*, vol. 60 (1), pp. 29–32, Jan. 1988 (cit. on p. 58).

[139] P. Emplit, J. Hamaide, F. Reynaud, C. Froehly, and A. Barthelemy, "Picosecond steps and dark pulses through nonlinear single mode fibers," *Optics Communications*, vol. 62 (6), pp. 374–379, Jun. 1987 (cit. on p. 58).

[140] A. M. Weiner, J. P. Heritage, R. J. Hawkins, R. N. Thurston, E. M. Kirschner, D. E. Leaird, and W. J. Tomlinson, "Experimental Observation of the Fundamental Dark Soliton in Optical Fibers," *Physical Review Letters*, vol. 61 (21), pp. 2445–2448, Nov. 1988 (cit. on p. 58).

[141] J. E. Rothenberg and H. K. Heinrich, "Observation of the formation of dark-soliton trains in optical fibers," *Optics Letters*, vol. 17 (4), p. 3, 1992 (cit. on p. 58).

[142] M. Nakazawa and K. Suzuki, "10 Gbit/s pseudorandom dark soliton data transmission over 1200 km," *Electronics Letters*, vol. 31 (13), pp. 1076–1077, Jun. 1995 (cit. on p. 58).

[143] Y. Kivshar, "Dark optical solitons: Physics and applications," *Physics Reports*, vol. 298 (2-3), pp. 81–197, May 1998 (cit. on p. 58).

[144] M. Conforti and S. Trillo, "Radiative effects driven by shock waves in cavity-less four-wave mixing combs," *Optics Letters*, vol. 39 (19), p. 5760, 2014 (cit. on p. 61).

[145] S. F. Wang, A. Mussot, M. Conforti, A. Bendahmane, X. L. Zeng, and A. Kudlinski, "Optical event horizons from the collision of a soliton and its own dispersive wave," *Physical Review A*, vol. 92 (2), p. 023 837, Aug. 2015 (cit. on pp. 68, 69).

[146] L. Landau and E. M. Lifshitz, *Quantum Mechanics (Non-relativistic Theory)*, Pergamon, London. 1977 (cit. on p. 69).

[147] M. Plöschner, T. Tyc, and T. Čižmár, "Seeing through chaos in multimode fibres," *Nature Photonics*, vol. 9 (8), pp. 529–535, Aug. 2015 (cit. on p. 75).

[148] W. H. Renninger and F. W. Wise, "Optical solitons in graded-index multimode fibres," *Nature Communications*, vol. 4, p. 1719, Apr. 2013 (cit. on pp. 75, 76).

[149] S. Berdagué and P. Facq, "Mode division multiplexing in optical fibers," *Applied Optics*, vol. 21 (11), p. 1950, Jun. 1982 (cit. on p. 75).

[150] J. Carpenter, B. J. Eggleton, and J. Schröder, "Observation of Eisenbud–Wigner–Smith states as principal modes in multimode fibre," *Nature Photonics*, vol. 9 (11), pp. 751–757, Nov. 2015 (cit. on p. 75).

[151] R. H. Stolen, J. E. Bjorkholm, and A. Ashkin, "Phase-matched three-wave mixing in silica fiber optical waveguides," *Applied Physics Letters*, vol. 24 (7), pp. 308–310, Apr. 1974 (cit. on p. 75).

[152] F. Poletti and P. Horak, "Dynamics of femtosecond supercontinuum generation in multimode fibers," *Optics Express*, vol. 17 (8), p. 6134, Apr. 2009 (cit. on p. 75).

[153] A. Picozzi, G. Millot, and S. Wabnitz, "Nonlinear virtues of multimode fibre: Nonlinear optics," *Nature Photonics*, vol. 9 (5), pp. 289–291, May 2015 (cit. on p. 76).

[154] K. Krupa, A. Tonello, B. M. Shalaby, M. Fabert, A. Barthélémy, G. Millot, S. Wabnitz, and V. Couderc, "Spatial beam self-cleaning in multimode fibres," *Nature Photonics*, vol. 11 (4), p. 237, Apr. 2017 (cit. on p. 76).

[155] L. G. Wright, Z. Liu, D. A. Nolan, M.-J. Li, D. N. Christodoulides, and F. W. Wise, "Self-organized instability in graded-index multimode fibres," *Nature Photonics*, vol. 10 (12), pp. 771–776, Nov. 2016 (cit. on pp. 76, 77).

[156] Z. Liu, L. G. Wright, D. N. Christodoulides, and F. W. Wise, "Kerr self-cleaning of femtosecond-pulsed beams in graded-index multimode fiber," *Optics Letters*, vol. 41 (16), p. 3675, Aug. 2016 (cit. on p. 76).

[157] C. Connaughton, C. Josserand, A. Picozzi, Y. Pomeau, and S. Rica, "Condensation of Classical Nonlinear Waves," *Physical Review Letters*, vol. 95 (26), p. 263 901, Dec. 2005 (cit. on p. 76).

[158] P. Aschieri, J. Garnier, C. Michel, V. Doya, and A. Picozzi, "Condensation and thermalization of classsical optical waves in a waveguide," *Physical Review A*, vol. 83 (3), p. 033 838, Mar. 2011 (cit. on p. 76).

[159] J. Lægsgaard, "Spatial beam cleanup by pure Kerr processes in multimode fibers," *Optics Letters*, vol. 43 (11), p. 2700, Jun. 2018 (cit. on p. 76).

[160] R. Guenard, K. Krupa, R. Dupiol, M. Fabert, A. Bendahmane, V. Kermene, A. Desfarges-Berthelemot, J. L. Auguste, A. Tonello, A. Barthélémy, G. Millot, S. Wabnitz, and V. Couderc, "Nonlinear beam self-cleaning in a coupled cavity composite laser based on multimode fiber," *Optics Express*, vol. 25 (19), p. 22 219, Sep. 2017 (cit. on p. 76).

[161] B. A. Malomed, D. Mihalache, F. Wise, and L. Torner, "Spatiotemporal optical solitons," *Journal of Optics B: Quantum and Semiclassical Optics*, vol. 7 (5), R53–R72, May 2005 (cit. on p. 76).

[162] Y. S. Kivshar and G. Agrawal, *Optical Solitons, from fibers to photonic crystals*. Elsevier, 2003 (cit. on p. 76).

[163] B. Crosignani and P. Di Porto, "Soliton propagation in multimode optical fibers," *Optics Letters*, vol. 6 (7), p. 329, Jul. 1981 (cit. on p. 76).

[164] B. Crosignani, A. Cutolo, and P. Di Porto, "Coupled-mode theory of nonlinear propagation in multimode and single-mode fibers: Envelope solitons and self-confinement," *Journal of the Optical Society of America*, vol. 72 (9), p. 1136, Sep. 1982 (cit. on p. 76).

[165] S. Buch and G. P. Agrawal, "Soliton stability and trapping in multimode fibers," *Optics Letters*, vol. 40 (2), p. 225, Jan. 2015 (cit. on p. 76).

[166] L. Wright, W. H. Renninger, D. N. Christodoulides, and F. W. Wise, "Spatiotemporal Dynamics of Multimode Optical Solitons," OSA, 2015, FW4D.1 (cit. on p. 77).

[167] L. G. Wright, D. N. Christodoulides, and F. W. Wise, "Controllable spatiotemporal nonlinear effects in multimode fibres," *Nature Photonics*, vol. 9 (5), pp. 306–310, May 2015 (cit. on p. 77).

[168] L. G. Wright, W. H. Renninger, D. N. Christodoulides, and F. W. Wise, "Spatiotemporal dynamics of multimode optical solitons," *Optics Express*, vol. 23 (3), p. 3492, Feb. 2015 (cit. on p. 77).

[169] S. Longhi, "Modulational instability and space time dynamics in nonlinear parabolic-index optical fibers," *Optics letters*, vol. 28 (23), pp. 2363–2365, 2003 (cit. on pp. 77, 79, 89).

[170] Kagan, Yu. and Maksimov, L. A., "Damping of trapped Bose-Einstein condensate oscillations at zero temperature," *Phys. Rev. A*, vol. 64 (5), p. 053 610, Oct. 2001 (cit. on p. 77).

[171] K. Krupa, C. Louot, V. Couderc, M. Fabert, R. Guenard, B. M. Shalaby, A. Tonello, D. Pagnoux, P. Leproux, A. Bendahmane, R. Dupiol, G. Millot, and S. Wabnitz, "Spatiotemporal characterization of supercontinuum extending from the visible to the mid-infrared in a multimode graded-index optical fiber," *Optics Letters*, vol. 41 (24), p. 5785, Dec. 2016 (cit. on p. 77).

[172] G. Lopez-Galmiche, Z. Sanjabi Eznaveh, M. A. Eftekhar, J. Antonio Lopez, L. G. Wright, F. Wise, D. Christodoulides, and R. Amezcua Correa, "Visible supercontinuum generation in a graded index multimode fiber pumped at 1064 nm," *Optics Letters*, vol. 41 (11), p. 2553, Jun. 2016 (cit. on p. 77).

[173] D. Ceoldo, K. Krupa, A. Tonello, V. Couderc, D. Modotto, U. Minoni, G. Millot, and S. Wabnitz, "Second harmonic generation in multimode graded-index fibers: Spatial beam cleaning and multiple harmonic sideband generation," *Optics Letters*, vol. 42 (5), p. 971, Mar. 2017 (cit. on p. 77).

[174] R. Dupiol, A. Bendahmane, K. Krupa, A. Tonello, M. Fabert, B. Kibler, T. Sylvestre, A. Barthelemy, V. Couderc, S. Wabnitz, and G. Millot, "Far-detuned cascaded intermodal four-wave mixing in a multimode fiber," *Optics Letters*, vol. 42 (7), p. 1293, Apr. 2017 (cit. on p. 77).

[175] F. Poletti and P. Horak, "Description of ultrashort pulse propagation in multimode optical fibers," *Journal of the Optical Society of America B*, vol. 25 (10), p. 1645, Oct. 2008 (cit. on pp. 77, 85).

[176] P. Horak and F. Poletti, "Multimode Nonlinear Fibre Optics: Theory and Applications," p. 23, 2012 (cit. on p. 77).

[177] L. G. Wright, Z. M. Ziegler, P. M. Lushnikov, Z. Zhu, M. A. Eftekhar, D. N. Christodoulides, and F. W. Wise, "Multimode Nonlinear Fiber Optics: Massively Parallel Numerical Solver, Tutorial, and Outlook," *IEEE Journal of Selected Topics in Quantum Electronics*, vol. 24 (3), pp. 1–16, May 2018 (cit. on p. 78).

[178] P. M. Lushnikov, "Fully parallel algorithm for simulating dispersion-managed wavelength-division-multiplexed optical fiber systems," *Optics Letters*, vol. 27 (11), p. 939, Jun. 2002 (cit. on p. 78).

[179] J. Lægsgaard, "Efficient simulation of multimodal nonlinear propagation in step-index fibers," *Journal of the Optical Society of America B*, vol. 34 (10), p. 2266, Oct. 2017 (cit. on p. 78).

[180] E. Nazemosadat, H. Pourbeyram, and A. Mafi, "Phase matching for spontaneous frequency conversion via four-wave mixing in graded-index multimode optical fibers," *Journal of the Optical Society of America B*, vol. 33 (2), p. 144, Feb. 2016 (cit. on p. 78).

[181] L. Pitaevskii and S. Stringari, *Bose-Einstein Condensation and Superfluidity*, ser. International Series of Monographs on Physics. Oxford: Oxford University Press, 2016 (cit. on p. 78).

[182] M. Kolesik and J. V. Moloney, "Nonlinear optical pulse propagation simulation: From Maxwell's to unidirectional equations," *Physical Review E*, vol. 70 (3), Sep. 2004 (cit. on p. 82).

[183] A. Couairon and A. Mysyrowicz, "Femtosecond filamentation in transparent media," *Physics Reports*, vol. 441 (2-4), pp. 47–189, Mar. 2007 (cit. on p. 82).

[184] J. Andreasen and M. Kolesik, "Nonlinear propagation of light in structured media: Generalized unidirectional pulse propagation equations," *Physical Review E*, vol. 86 (3), Sep. 2012 (cit. on p. 82).

[185] E. Rubino, J. McLenaghan, S. C. Kehr, F. Belgiorno, D. Townsend, S. Rohr, C. E. Kuklewicz, U. Leonhardt, F. König, and D. Faccio, "Negative-Frequency Resonant Radiation," *Physical Review Letters*, vol. 108 (25), Jun. 2012 (cit. on p. 82).

[186] M. Conforti, A. Marini, T. X. Tran, D. Faccio, and F. Biancalana, "Interaction between optical fields and their conjugates in nonlinear media," *Optics Express*, vol. 21 (25), p. 31 239, Dec. 2013 (cit. on p. 82).

[187] A. Ferrando, M. Zacarés, P. Fernández de Córdoba, D. Binosi, and Á. Montero, "Forward-backward equations for nonlinear propagation in axially invariant optical systems," *Physical Review E*, vol. 71 (1), Jan. 2005 (cit. on p. 82).

[188] M. A. Eftekhar, L. G. Wright, M. S. Mills, M. Kolesik, R. A. Correa, F. W. Wise, and D. N. Christodoulides, "Versatile supercontinuum generation in parabolic multimode optical fibers," *Optics Express*, vol. 25 (8), p. 9078, Apr. 2017 (cit. on p. 83).

[189] A. V. Husakou and J. Herrmann, "Supercontinuum Generation of Higher-Order Solitons by Fission in Photonic Crystal Fibers," *Physical Review Letters*, vol. 87 (20), Oct. 2001 (cit. on p. 83).

[190] L. Yu, M. Huang, M. Chen, W. Chen, W. Huang, and Z. Zhu, "Quasi-discrete Hankel transform," p. 3, (cit. on p. 86).

[191] M. Guizar-Sicairos and J. C. Gutiérrez-Vega, "Computation of quasi-discrete Hankel transforms of integer order for propagating optical wave fields," *J. Opt. Soc. Am. A*, vol. 21 (1), pp. 53–58, Jan. 2004 (cit. on p. 86).

[192] J. Hult, "A Fourth-Order Runge–Kutta in the Interaction Picture Method for Simulating Supercontinuum Generation in Optical Fibers," *Journal of Lightwave Technology*, vol. 25 (12), pp. 3770–3775, Dec. 2007 (cit. on p. 87).

[193] M. Karlsson, D. Anderson, and M. Desaix, "Dynamics of self-focusing and self-phase modulation in a parabolic index optical fiber," *Optics letters*, vol. 17 (1), pp. 22–24, 1992 (cit. on p. 88).

[194] S. Longhi and D. Janner, "Self-focusing and nonlinear periodic beams in parabolic index optical fibres," *Journal of Optics B: Quantum and Semiclassical Optics*, vol. 6 (5), p. 303, 2004 (cit. on p. 88).

[195] M. Karlsson, D. Anderson, M. Desaix, and M. Lisak, "Dynamic effects of Kerr nonlinearity and spatial diffraction on self-phase modulation of optical pulses," *Opt. Lett.*, vol. 16 (18), pp. 1373–1375, 1991 (cit. on p. 88).

[196] C. Mas Arabí, A. Kudlinski, A. Mussot, and M. Conforti, "Geometric parametric instability in periodically modulated graded-index multimode fibers," *Physical Review A*, vol. 97 (2), p. 023 803, Feb. 2018 (cit. on p. 93).

[197] V. M. Pérez-García, P. Torres, J. J. García-Ripoll, and H. Michinel, "Moment analysis of paraxial propagation in a nonlinear graded index fibre," *Journal of Optics B: Quantum and Semiclassical Optics*, vol. 2 (3), p. 353, 2000 (cit. on p. 94).

[198] E. Pinney, "The nonlinear differential equation $y'' + p(x)y + Cy^{-3} = 0$," *Proceedings of the American Mathematical Society*, vol. 1 (5), p. 681, 1950 (cit. on p. 95).

[199] J. F. Cariñena, "A new approach to Ermakov systems and applications in quantum physics," *The European Physical Journal Special Topics*, vol. 160 (1), pp. 51–60, 2008 (cit. on p. 95).

[200] F. Copie, A. Kudlinski, M. Conforti, G. Martinelli, and A. Mussot, "Modulation instability in amplitude modulated dispersion oscillating fibers," *Optics Express*, vol. 23 (4), pp. 3869–3875, Feb. 2015 (cit. on p. 101).

[201] M. Conforti, S. Trillo, A. Mussot, and A. Kudlinski, "Parametric excitation of multiple resonant radiations from localized wavepackets," *Scientific Reports*, vol. 5 (1), Aug. 2015 (cit. on p. 111).

[202] M. Conforti, S. Trillo, A. Kudlinski, and A. Mussot, "Multiple QPM Resonant Radiations Induced by MI in Dispersion Oscillating Fibers," *IEEE Photonics Technology Letters*, vol. 28 (7), pp. 740–743, Apr. 2016 (cit. on p. 111).

[203] M. Conforti and S. Trillo, "Dispersive wave emission from wave breaking," *Optics Letters*, vol. 38 (19), p. 3815, Oct. 2013 (cit. on p. 111).

[204] U. Tegin and B. Ortac, "Spatiotemporal Instability of Femtosecond Pulses in Graded-Index Multimode Fibers," *IEEE Photonics Technology Letters*, vol. 29 (24), pp. 2195–2198, Dec. 2017 (cit. on p. 113).

[205] M. Conforti, F. Baronio, and S. Trillo, "Resonant radiation shed by dispersive shock waves," *Physical Review A*, vol. 89 (1), Jan. 2014 (cit. on p. 113).

AUTHOR'S BIBLIOGRAPHY

AUTHOR'S BIBLIOGRAPHY

Publications in peer-reviewed international journals

1. T. Marest, C. Mas Arabí, M. Conforti, A. Mussot, C. Milián, D. Skryabin, A.Kudlinski, "Emission of dispersive waves from a train of dark solitons in optical fibers", *Optics Letters*, 41, 2454 (2016).

2. C. Mas Arabí, F. Bessin, A. Kudlinski, A. Mussot, D. Skryabin, M. Conforti, "Efficiency of four-wave mixing between orthogonally polarized linear waves and solitons in a birefringent fiber". *Physical Review A*, 94, 063847 (2016).

3. M. Conforti, C. Mas Arabí, A. Mussot, A. Kudlinski. "Fast and accurate modeling of nonlinear pulse propagation in graded-index multimode fibers" *Optics Letters*, 42, 4004 (2017).

4. T. Marest, C. Mas Arabí, M. Conforti, A. Mussot, C. Milián, D. Skryabin, A.Kudlinski. "Grayness-dependent emission of dispersive waves from dark solitons in optical fibers", *Optics Letters*, 43, 1511 (2018).

5. C. Mas Arabí, A. Mussot, A. Kudlinski,M. Conforti. "Geometric parametric instability in periodically modulated graded-index multimode fibers". *Physical Review A*, 97, 023803 (2018).

6. T. Marest, C. Mas Arabí, M. Conforti, A. Mussot, C. Milián, D. Skryabin, A.Kudlinski, "Collision between a dark soliton and a linear wave in an optical fiber", *Optics Express* (2018)

Orals in peer-reviewed international conferences

(*) Name of the presenting author:

1. C. Mas Arabí, F. Bessin, A. Kudlinski, A. Mussot, D. Skryabin, M. Conforti*. "Conversion efficiency of vector scattering between soltions and dispersive waves", Nonlinear Photonics, Sydney, Australia (2016).

2. C. Mas Arabí*, F. Bessin, A. Kudlinski, A. Mussot, D. Skryabin, M. Conforti, "Vector collision between Solitons and Dispersive Waves" , Nice Optics, Nice, France (2016).

3. C. Mas Arabí*, A. Kudlinski, A. Mussot, M. Conforti, "Parametric instability in a periodic multimode fiber", CLEO Europe, Munich, Germany (2017).

4. C. Mas Arabí, A. Kudlinski, A. Mussot, M. Conforti*."Geometric parametric instability in modulated parabolic graded-index fibers". Nonlinear Photonics, Zurich, Switzerland (2018).

5. T. Marest, C. Mas Arabí, M. Conforti, A. Mussot*, C. Milian, D. Skryabin, A. Kudlinski."Dark solitons, dispersive waves and their collision in an optical fiber". Nonlinear Photonics, Zurich, Switzerland (2018).

6. M. Conforti*, C. Mas Arabí, A. Mussot, A. Bendahmane, A. Kudlinski. "Efficient modelling of nonlinear propagation in multimode graded-index fibers" Nonlinear Photonics, Zurich, Switzerland (2018).

Propagation non-linéaire dans les fibres optiques: solitons, ondes dispersives et instabilités multimodes

Resumé: Ces travaux de thèse portent sur l'étude de la propagation non-linéaire de la lumière dans les fibres optiques. Nous nous sommes concentrés sur deux types de problèmes: les solitons dans les fibres monomodes et la propagation de la lumière multimode dans les fibres à gradient d'indice. Les solitons sont des impulsions lumineuses courtes et intenses qui restent localisées lors de la propagation. Ils apparaissent sous la forme d'un maximum d'intensité (appelé soliton brillant) dans le régime de dispersion anormale, ou d'un trou d'intensité sur un fond continu en dispersion normale (soliton sombre). Lorsque leur fréquence de porteuse est proche de la longueur d'onde de dispersion nulle ou que la biréfringence de la fibre est prise en compte, les solitons peuvent interagir avec des ondes de faible amplitude et générer de nouvelles fréquences. Nous avons étudié théoriquement l'efficacité de ces processus dans le cas de solitons sombres qui se propagent près de la longueur d'onde de dispersion nulle et de solitons brillants dans une fibre fortement biréfringente. Les résultats de ces analyses ont été validés par des expériences.

Dans la deuxième partie de cette thèse, nous augmentons le nombre de degrés de liberté en utilisant des fibres multimode. La propagation de la lumière dans les fibres multimodes s'acompage d'une dynamique spatio-temporelle encore loin d'être complètement comprise. Un effet qui se produit dans les fibres GRIN est le l'auto-imagerie, un processus dans lequel le faisceau spatial injecté à l'entrée se réplique périodiquement le long de la fibre, créant un réseau d'indice grâce à l'effet Kerr de la silice. En raison de ce comportement périodique, quand une onde continue se propage dans une fibre multimode, certaines fréquences deviennent instables et sont amplifiées (processus appelé instabilité paramétrique géométrique). Nous avons caractérisé le motif des fréquences instables lorsqu'une variation périodique du diamètre de la fibre est réalisée. Nous présentons également un modèle unidimensionnel capable d'imiter la dynamique spatio-temporelle de la lumière dans une fibre multimode.

Mots clés: Optique non-linéaire; Fibres optiques; Solitons; Ondes dispersives; Fibres multimode; Instabilité modulationelle; Instabilité paramétrique.

Nonlinear propagation in optical fibers: from soliton radiations to multimode instabilities

Abstract: The main goal of this thesis is the investigation of nonlinear light propagation in optical fibers. We have focused on two kinds of problems: solitons in single-mode fibers and multimode light propagation in graded index (GRIN) fibers. Solitons are short and intense light pulses which remain localized during propagation. They appear as maxima of intensity (called bright soliton) in the anomalous dispersion regime or intensity dips on a continuous wave (CW) background in normal dispersion (dark solitons). When their carrier frequency is close to the zero dispersion wavelength (ZDW) or when fiber's birefringence is taken into account, solitons can interact with weak waves and generate new frequencies. We have studied theoretically the efficiency of these processes in the case of dark solitons propagating close to ZDW and bright solitons in a highly birefringent fiber. The outcomes of these analysis have been validated experimentally.

In the second part of this thesis, we increase the degrees of freedom by using multimode fibers. Light propagation in multimode fibers entails a spatiotemporal dynamics which is still far to be fully understood. An effect arising in GRIN fibers is self-imaging, a process in which the spatial beam injected at the input replicates itself periodically along the fiber, creating a grating by virtue of the silica's Kerr effect. Due to this periodic behavior, when a CW propagates in a multimode fiber, some frequencies become unstable and they are amplified (a process called geometric parametric instability). We have characterized the pattern of unstable frequencies when a periodic variation of the fiber diameter is made. We also present a reduced one dimensional model which is able to mimic the spatiotemporal dynamics of light in a multimode GRIN fiber.

Keywords: Temporal optical solitons; Nonlinear optics; Optical fiber; Modulation instability; Multimode fiber; Dispersive waves.